Fakultät für Chemie
Technische Universität München

Ab initio modeling of heterogeneous catalysis: Multiscale analysis of interacting reaction pathways

Juan Manuel Lorenzi

Vollständiger Abdruck der von der Fakultät für Chemie der Technischen Universität München zur Erlangung des akademischen Grades eines

Doktors der Naturwissenschaften (Dr. rer. nat.)

genehmigten Dissertation.

Vorsitzender:
Priv.-Doz. Dr. Harald Oberhofer

Prüfende der Dissertation:
1. Prof. Dr. Karsten Reuter
2. Prof. Dr.-Ing. Kai-Olaf Hinrichsen

Die Dissertation wurde am 02.11.2017 bei der Technischen Universität München eingereicht und durch die Fakultät für Chemie am 13.12.2017 angenommen.

To Mihaela.

Preface

This is a publication-based dissertation. The work presented here has been accepted for publication in international, peer-reviewed journals. The first chapters of this thesis provide the methodological background as well as a summary of relevant literature. Next, short summaries of the two published articles are included. Finally, general conclusions on this dissertation's contributions are presented. The full texts of the articles, as well as the associated supporting material, are included in the appendix.

Abstract

Approaches to heterogeneous catalysis which aim at a detailed microscopic understanding necessarily employ simplified models. Simplifications often include (a) using a single crystal model catalyst and (b) treating a reduced reaction network. In this thesis, we use computational modeling to explore some consequences of the latter approximation. In addition, we introduce new methodology for multiscale modeling of reactions with extended reaction networks.

In the first part of the thesis, we have built and analyzed a first-principles kinetic Monte Carlo (1p-kMC) model of simultaneous oxidation of NO and CO at Pd(100) under oxygen-rich conditions. Previous microscopically detailed studies analyzed either pathway separately (CO oxidation or NO oxidation). In contrast, supported catalyst experiments show different types of inhibiting and/or enhancing effects when both reactions occur simultaneously. Our detailed 1p-kMC model predicts inhibiting effects at oxygen-lean conditions and synergistic effects at oxygen-rich conditions. In the latter case, very low NO concentrations can drastically reduce oxygen coverages, suggesting that NO can strongly inhibit oxide formation. Such behavior arises from intricate kinetic effects and highlights the difficulties of extrapolating results from simplified models to more realistic situations as well as the importance of further improving the complexity of theoretical models.

The second part of this work has focused on extending methodology for the coupling of 1p-kMC and computational fluid dynamics (CFD) simulations. These multiscale modeling schemes are crucial for the validation of microkinetic models with *in-situ* catalysis experiments, something particularly important when small reactant quantities can have marked effects in the catalyst's behavior. We have extended an existing multiscale approach, in which the coupling is done through the interpolation of a precalculated dataset of steady-state reactivity. For this, we developed a novel interpolation method based on the modified Shepard method. The interpolants consist of a weighted sum of linear approximations centered on the points on the dataset. The weights are based on automatically generated local metrics. In this way, it is possible to exploit the special characteristics of 1p-kMC-based reactivity maps and construct interpolants of significantly better quality using smaller datasets. This is particularly advantageous for kinetic models with many gas-phase species, as they normally would require larger input datasets, i.e. many computationally demanding 1p-kMC simulations. Furthermore, the mathematical simplicity of the method makes it suitable for use by non-experts, which can facilitate the development of multiscale models.

Zusammenfassung

Der Einsatz von Studien zur Erlangung eines detaillierten, atomar aufgelöstes Verständnis von heterogener Katalyse basiert notwendigerweise auf vereinfachenden Modellen. Diese beinhalten meist einerseits die Benutzung von Einkristall-Modellkatalysatoren und andererseits die Behandlung eines reduzierten Reaktionsnetzwerkes. In der vorliegenden Dissertation werden Computermodellierungstechniken benutzt, um die Auswirkungen dieser zweiten Näherung zu erforschen. Zusätzlich wird eine neue Methodik zur Multiskalenmodellierung von Reaktionen mit umfangreichen Reaktionsnetzwerken vorgeschlagen.

Der erste Teil der Arbeit fokussiert sich entsprechend auf den Aufbau und die Analyse eines *first-principles kinetic Monte Carlo* (1p-kMC) Modells zur Beschreibung der gleichzeitigen Oxidation von NO und CO an Pd(100) Oberflächen unter sauerstoffreichen Bedingungen. Bisherige atomar aufgelöste Studien betrachteten hierbei meist die CO oder NO Oxidation als isolierte Reaktionswege. Solche Annahmen widersprechen allerdings experimentellen Studien auf geträgerten Katalysatoren, die verschiedene Arten von hemmenden und/oder verstärkenden Effekten zeigten, sobald beide Reaktionen gleichzeitig auftreten. Das hier vorgeschlagene erweiterte 1p-kMC Modell sagt hemmende Effekte unter sauerstoffarmen Bedingungen und synergistische Effekte unter sauerstoffreichen Bedingungen vorher. Im letzteren Fall können niedrige NO Konzentrationen die Sauerstoffbedeckung drastisch reduzieren. Dies deutet darauf hin, dass NO die Oberflächenoxidbildung stark einschränkt. Solch ein Verhalten resultiert aus verworrenen kinetischen Effekten und ist damit ein Paradebeispiel für die die Schwierigkeiten, die aus einer Extrapolation von vereinfachten Modellen hin zu komplizierteren, realistischeren Situationen entstehen können. Zugleich unterstreicht diese Erkenntnis damit die Notwendigkeit komplexerer theoretischer Modelle.

Im Mittelpunkt des zweiten Teiles der Arbeit steht die Kopplung von 1p-kMC und Computer-Fluiddynamik (CFD) Simulationen. Diese Multiskalenmodellierungsschemata sind von essentieller Bedeutung für die Validierung mikrokinetischer Modelle mit Hilfe von *in-situ* Experimenten, insbesondere wenn bereits kleinste Mengen von Reaktanten aufgeprägte Effekte auf das Katalysator-Verhalten haben. In diesem Zusammenhang wird ein existierender Multiskalenansatz derart erweitert, dass die entsprechende Skalenkopplung nun durch die Interpolation zuvor berechneter steady-state Reaktivitätsdaten erfolgt. Hierfür wird, basierend auf der modifizierten Shepard Methode, eine neuartige Interpolationsroutine entwickelt. Die Interpolanten bestehen dabei aus einer gewichteten Summe von linearen Näherungen, die auf den Punkten des Datensatzes zentriert sind. Die entsprechenden Gewichte basieren wiederum auf automatisch generierten lokalen Metriken. Auf diese Weise ist es möglich, die spezielle Charakteristik von 1p-kMC basierten Reaktivitätsfunkttionen auszunutzen und damit signifikant bessere Interpolanten

mit kleineren Datensätzen zu konstruieren. Dies ist besonders für kinetische Modelle mit mehreren Gasphasenspezies vorteilhaft, die normalerweise große Input-Datensätze und damit viele rechenintensive 1p-kMC Simulationen erfordern. Letztlich ist die hier vorgeschlagene Methode durch ihre mathematische Einfachheit auch für Laien zugänglich, was im Umkehrschluss der weiteren Entwicklung von Multiskalenmodellen zuträglich ist.

Contents

1 Introduction

It is difficult to overstate the impact of heterogeneous catalysis in the quality of life: it is crucial to clean exhaust gases from motor vehicles; to facilitate the production of fertilizers; and to provide a plethora of key chemical compounds for industrial processes. Clearly, there are great incentives to reach a detailed understanding of catalytic processes, with the ultimate aim of maximizing their cost-, energy- and materials-efficiency. However, such task is daunting: catalytic processes are extremely complex. Such complexity stems mainly from the fact that catalysis is an intrinsically multiscale problem. From the electronic structure of the materials, through the mesoscopic composition of porous catalyst, to the flow dynamics in the reaction chamber, phenomena occurring at vastly different time and length scales have an impact on the final performance of the catalytic process. Due to this complexity, most of the advances in catalyst design in the last few decades have been extensively based on a trial-and-error based approach.

A complementary way to tackle this problem is to take a *bottom-up* approach. This starts with a detailed microscopic understanding of the catalytic phenomena. Here, the powerful tools of surface science, including spectroscopic and scanning microscopy techniques, provide crucial microscale information such as binding sites of intermediates, overlayer structures and binding energies[1]. Nevertheless, traditional techniques have the disadvantage of being restricted to ultra high vacuum (UHV) conditions. This implies that reactions need to be run at pressures much smaller than those in realistic systems, or that the characterization experiments need to be performed *ex situ*, i.e. after the reaction has finished.

Luckily, advances in experimental techniques are changing this picture. So-called *in situ* methods consist of adaptations of traditional surface science experimental setups which allows for the study of catalysts during operation at pressures close to ambient[2]. These techniques are a highly promising way towards a fundamental understanding of catalytic processes, and have already provided valuable new insights[3, 4, 5, 6, 7]. However, there are still several challenges to be resolved. At higher pressures, mass and heat transfer effects become relevant. In such situation, the nominal values of pressure and temperature at the inlet of the reactor might differ considerably from the values at the immediate vicinity of the catalyst. Therefore, conclusions on its intrinsic reactivity can be difficult to reach[8, 9]. This is aggravated due to the fact that in-situ experiments typically require complex experimental setups. These comprise, e.g. nozzles from pumping systems close to the sample in spectroscopic techniques[10], or the tips of scanning microscopes[11]. The presence of such elements alters flow profiles and complicates their analysis, in particular preventing the use of simplified flow patterns.

Theoretical approaches have for a long time been invaluable to support and validate experimental discoveries. Fig. 1.1 indicates some of the theoretical methods considered

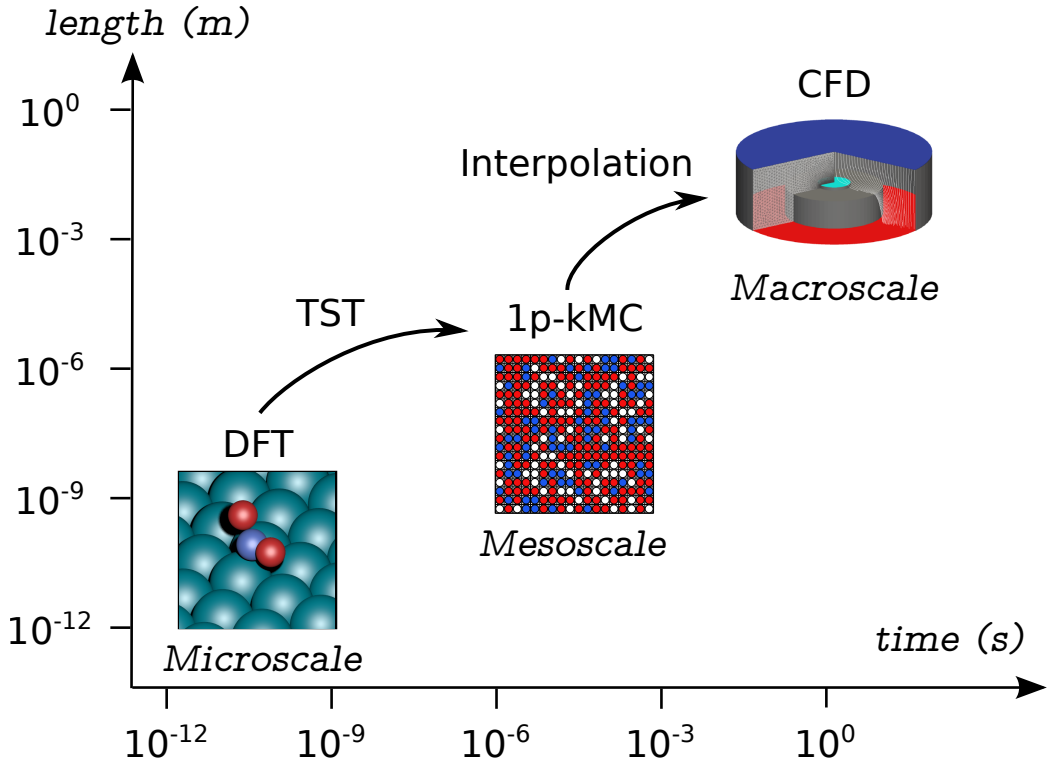

Figure 1.1: The different methods used to describe the scales relevant to heterogeneous catalysis. The microscale is described with density functional theory (DFT), the mesoscale with first principles kinetic Monte Carlo (1p-kMC) and the macroscale with computational fluid dynamics (CFD). In addition, the formalisms that help connecting the different scales are also indicated: transition state theory (TST) for micro- to mesoscale and interpolation for meso- to macroscale.

in this thesis, roughly indicating the length and time scales that they can describe. At the smallest scale are *ab initio* electronic structure methods. These have been shown to provide quantitative predictions on materials properties. Such predictions are material-specific and independent from experimental inputs, i.e. there are no adjustable parameters. This makes such theoretical calculations a powerful complement to experiments. Density functional theory (DFT) in particular has been a key element in heterogeneous catalysis research. Due to its relatively low computational cost and high accuracy, DFT has become the method of choice for the treatment of large chemically complex systems including extended solid surfaces [12]. In contrast, traditional ab initio quantum chemistry approaches remain mostly limited to treating gas-phase reactions. DFT is currently the workhorse in computational materials research in general, and in surface science (and heterogeneous catalysis) in particular.

Initially, first-principle methods have focused on providing equilibrium information to support surface science experiments. For example, helping to elucidate which are

the most stable intermediates of a given reaction pathway. More recently, advanced approaches such as so-called *ab-initio* thermodynamics, are able predict the equilibrium structure of surfaces at elevated temperature and exposed to different gas compositions[6]. In the realm of kinetics, DFT can be also used to evaluate reaction barriers of elementary processes and obtain detailed reaction energy diagrams[13].

This information can be used to speculate on the characteristics of the reaction's kinetics, e.g. by guessing which the "rate-determining step" is. However, quite often the kinetic behavior is more complex than what can be deduced from energetics only: which processes are executed can depend in non trivial ways on the overlayers that form, or there could be more than one single rate-controlling step for some conditions[14]. In these cases explicit simulations of kinetics are needed. The most widely used methods for this purpose are rate-equation based. These rely on a mean field (MF) approximation which neglects the effects of the overlayer structures and of fluctuations or correlations[15]. They are expected to fail in cases in which diffusion is slow or limited, or when lateral interactions effects are important[15, 16]. Therefore, in this thesis we employ first-principles kinetic Monte Carlo (1p-kMC) simulations, which provide a much more detailed description of the catalytic process. Contrary to MF-based models, 1p-kMC uses an explicit representation of the surface lattice and takes into account all fluctuations and correlations arising from kinetic effects[17]. This method has been incredibly successful in pushing forward our understanding of catalysis[18, 19, 6].

One problem of this approach is the fact that the construction of a predictive-quality 1p-kMC model is a challenging and time consuming task. Extensive details on the catalyst's structure, all relevant intermediates and all relevant reaction barriers are needed. Currently, there is no standard approach for automatically obtaining all this information and generating the required catalog of elementary processes. Moreover, there is currently no 1p-kMC model which can describe the full complexity of an industrial heterogeneous catalyst. In view of this, a valid strategy is to treat simpler problems, that can nevertheless provide novel insights. In this sense, two major approximations are normally used: On the one hand, single crystal model catalysts are used. On the other hands, only simplified reaction pathways are considered.

In the first part of this work, we have examined the latter approximation. We have taken the simultaneous oxidation of CO and NO by O_2 at Pd(100) as a showcase for the very relevant problem of automotive exhaust treatment with platinum-group metals. The oxidation of these two species has been treated in the past with microscopically detailed 1p-kMC models, but only separately[20, 21, 22, 23]. Moreover, the Pd(100) surface has received enormous attention, in particular through attempts to elucidate which is the morphology of the "active phase" for CO oxidation. Different studies have been published which support the idea that an oxide forms during activity, others that reject this idea, and others which suggest that the surface oscillates between oxidized and reduced states[24, 25, 26, 27, 20, 28, 5]. Our main result shows that CO and NO oxidation pathways interact in a complex way. In particular, kinetic effects arising from the addition of very small amounts of NO can drastically reduce the surface's oxygen coverage under oxygen-rich conditions. This has implications on the stability of the surface oxides when NO is present. It also highlights that active phases observed in

experiments involving only CO and O_2 are not guaranteed to appear under more realistic gas mixtures, even when the additional species are a minority.

Although an extensive set of DFT calculations have informed the construction of our model and provided the kinetic barriers, approximations had to be made in the process. It is thus very important to experimentally validate the results. As kinetics have shown to play a crucial role in the effects observed, detailed *in situ* experiments characterizing the surface under high pressure conditions are needed to observe the predicted effects. In addition, a multiscale coupling method able to incorporate a description of the gas dynamics on top of the intrinsic kinetics modeled by 1p-kMC is necessary for direct comparison. However, at the time of this writing, there is no standard coupling methodology. This has motivated the second part of this work, which focused on extending the multiscale methodology developed by Matera and collaborators[29, 8, 9, 30].

This approach is based on the interpolation of a precalculated steady-state activity dataset. This makes it computationally much more efficient at runtime and conceptually simpler than alternative direct coupling methods[30]. A disadvantage is that it is limited to reactions involving only a small number N_{spec} of reactive gas-phase species. This is because the activity maps are functions of $D = N_{\text{spec}} + 1$ variables: N_{spec} partial pressures and the temperature. Higher dimensional functions are more challenging to interpolate, because the number of data points required normally grows exponentially with the dimension. For this reason, this coupling method has up to now been limited to reactions with only two relevant gas-phase species (such as CO oxidation). In this thesis, we have developed a new interpolation method tailored to solve this problem. The new method is able to exploit the characteristics of 1p-kMC-based activity maps and produce good quality interpolants using small input datasets. An additional advantage of the method is that it is based only on geometrical considerations and that all adjustable parameters have clear conceptual interpretations. We expect these properties will make it easy to use by researchers who are not necessarily experts in interpolation and thus facilitate the generation of multiscale models of heterogeneous catalysis.

This thesis is organized as follows. Chapter 2 presents the theoretical basis for the quantum mechanical treatment of heterogeneous catalysis and the fundamentals of DFT. Chapter 3 introduces the basics of microkinetic modeling, with a focus on 1p-kMC. Chapter 4 gives a summary of the literature on the kinetics of CO and NO oxidation at the Pd(100) surface. Chapter 5 is an overview of existing methodology for the coupling of 1p-kMC and CFD simulations. In chapter 6, short summaries of the publications included in this thesis are given, as well as statements of the individual contributions of each author. General conclusions and an outlook with potential future research directions are presented in chapter 7. Finally, full copies of the publications are included in appendix A.

2 The microscopic scale and density functional theory

2.1 The potential energy surface

At the smallest scale, heterogeneous catalysis is dominated by the breaking and making of chemical bonds. These are the result of the interaction between the atoms in the catalyst and the reaction intermediates, mediated by their electronic structure. A quantum mechanical description of this interaction is needed. Almost invariably catalysis research relies on the (typically very good) approximation that electronic dynamics is much faster than the dynamics of the nuclei. It is possible thus to treat them separately, by solving the dynamics of the electrons for any given configuration of the nuclei as if they were fixed. This is the well known Born-Oppenheimer approximation, and leads to the definition of the potential energy surface (PES)

$$E = E(\mathbf{R}_1, ..., \mathbf{R}_{N_{\text{at}}}) = E^{\text{el}}(\mathbf{R}_1, ..., \mathbf{R}_{N_{\text{at}}}) + V^{\text{n-n}}(\mathbf{R}_1, ..., \mathbf{R}_{N_{\text{at}}}), \tag{2.1}$$

which gives the total of the system as a function of the nuclear coordinates $\mathbf{R}_j$. N_{at} is the total number of atoms, E^{el} represents the electronic contribution (including the interaction of electrons with the nuclei) and $V^{\text{n-n}}$ represents the potential energy due to the electrostatic interaction between the nuclei. As we will see in the next chapter, the PES is a central element for the construction of 1p-kMC models used to simulate chemical kinetics and efficient methods to evaluate it at arbitrary nuclear positions are needed.

The PES can be obtained by solving the time-independent electronic Schrödinger equation

$$\hat{H}\Psi(\mathbf{r}_1, ..., \mathbf{r}_{N_{\text{elec}}}) = E^{\text{el}}\Psi(\mathbf{r}_1, ..., \mathbf{r}_{N_{\text{elec}}}) \tag{2.2}$$

where $\Psi(\mathbf{r}_1, ..., \mathbf{r}_{N_{\text{elec}}})$ is the ground state wave-function of the system, the $\mathbf{r}_i$ are the positions of the N_{elec} electrons and $\hat{H}$ is the electronic Hamiltonian operator

$$\begin{aligned} \hat{H} &= (\hat{T} + \hat{V}^{\text{e-e}} + \hat{V}^{\text{ext}}) \\ &= \left(-\frac{1}{2} \sum_{i=1}^{N_{\text{elec}}} \nabla^2_{\mathbf{r}_i} + \sum_{i<j} \frac{1}{||\mathbf{r}_i - \mathbf{r}_j||_2} + \sum_{i=1}^{N_{\text{elec}}} v^{\text{ext}}(\mathbf{r}_i) \right) \end{aligned} \tag{2.3}$$

given by the sum of the kinetic energy operator $\hat{T}$, the electron-electron interaction potential $\hat{V}^{\text{e-e}}$ and the external potential $\hat{V}^{\text{ext}}$. In our case, the external potential corre-

sponds to the interaction of the electrons with the nuclei

$$v^{\text{ext}}(\mathbf{r}_i) = v_0^{\text{ext}}(\mathbf{r}_i) = -\sum_{j=1}^{N_{\text{at}}} \frac{Z_j}{||\mathbf{R}_j - \mathbf{r}_i||_2}, \tag{2.4}$$

where the Z_j are the atomic numbers. In the formulas above, the Hamiltonian $\hat{H}$ depends parametrically on the nuclear positions $\{\mathbf{R}_1, ..., \mathbf{R}_{N_{\text{at}}}\}$ through $\hat{V}^{\text{ext}}$. As consequence, the wavefunction $\Psi(\mathbf{r}_1, ..., \mathbf{r}_{N_{\text{elec}}})$ and the energy E^{el} are also functions of such parameters. We omit including this explicitly in most formulas to keep notation more compact.

Direct solution of equation (2.2) is prohibitively expensive with modern computers for all but the simplest examples. Luckily, a vast collection of different approximate solution methods have been developed. These provide different levels of accuracy and computation costs. By far the most widely used in catalysis research is density functional theory (DFT), as it provides a good compromise between these two factors.

2.2 Density functional theory

The Schrödinger equation given by eq. (2.2) is a $3N_{\text{elec}}$-dimensional partial differential equation, which can only be solved analytically for $N_{\text{elec}} \leq 2$. For systems relevant for heterogeneous catalysis, in which not only reacting molecules but also the solid substrate need to be considered, the value of N_{elec} can easily reach the thousands. The large dimensionality of the wave function makes the use of traditional wavefunction-based computational methods impractical in this case. Density based methods, such as DFT, provide a solution to this problem.

The conceptual basis for DFT can be fond in the two Hohenberg-Kohn (HK) theorems [31]. In order to state them, we must consider a class of eigenvalue problems similar to eq. (2.2), in which the $\hat{T}$ and $\hat{V}_{\text{e-e}}$ terms in the Hamiltonian (2.3) are fixed, but such that the external potential $v^{\text{ext}}(\mathbf{r})$ is arbitrary (i.e. not necessarily equal to $v_0^{\text{ext}}(\mathbf{r})$ from eq. (2.4)). The first HK theorem (HK1) relates the choice of the external potential and the ground state electronic density, given by

$$\rho(\mathbf{r}) = N_{\text{elec}} \int \text{dr}_2\text{d...dr}_{N_{\text{elec}}} \Psi^*(\text{r}, \text{r}_2, ..., \text{r}_{N_{\text{elec}}}) \Psi(\text{r}, \text{r}_2, ..., \text{r}_{N_{\text{elec}}}). \tag{2.5}$$

It is intuitively clear that fixing $v^{\text{ext}}(\mathbf{r})$ also fixes the ground state density $\rho(\mathbf{r})$, as it fully determines the Hamiltonian. HK1 states that the converse is also true: given a density function $\rho(\mathbf{r})$, there exists an unique external potential $v_{\text{ext}}(\mathbf{r})$ for which $\rho(\mathbf{r})$ is the ground state density. Therefore the Hamiltonian, and thus all ground state properties of the system can be considered *functionals* of the density. I.e. for any arbitrary $\rho(\mathbf{r})$ we can write $\Psi = \Psi[\rho]$ for the ground state wavefunction. This result shows that a description of the system based on the density ρ, instead of the wave function Ψ, is in principle possible. Such description can overcome the challenge of the high dimensionality of eq. (2.2), as ρ is a function of only the 3 variables.

Given a certain Hamiltonian $\hat{\tilde{H}}$, defined by fixing the value of $v^{\text{ext}} = \tilde{v}^{\text{ext}}$, we can define an energy functional according to

$$E_{\hat{\tilde{H}}}[\rho] = \left\langle \Psi[\rho] \middle| \hat{\tilde{H}} \middle| \Psi[\rho] \right\rangle. \tag{2.6}$$

It is important to notice that this functional can be evaluated for any arbitrary density, i.e. ρ does not need to coincide with the ground state density $\tilde{\rho}$ associated to Hamiltonian $\hat{\tilde{H}}$. The second HK theorem (HK2) states that

$$E_{\hat{\tilde{H}}}[\tilde{\rho}] < E_{\hat{\tilde{H}}}[\rho] \quad \forall \rho \neq \tilde{\rho}. \tag{2.7}$$

This implies that the ground state density corresponds to a minimum of the energy functional.

The most popular method to make use of the HK theorems for practical energy evaluations is due to Kohn and Sham[32]. The basic idea behind Kohn-Sham-DFT (KS-DFT) is to use an auxiliary, fictitious system which is easier to solve: a system of non-interacting electrons, i.e. such that $\hat{V}^{\text{e-e}} = 0$. The HK1 theorem implies that there exists one external potential $v_s^{\text{ext}}(\mathbf{r})$ for which this auxiliary system has a ground state density exactly equal to the ground state density of the interactive systems we intend to solve. In what follows, we will refer to quantities pertaining to this non-interactive system with a subindex s. Similarly, we will indicate quantities pertaining to the interactive system of interest with a subindex 0.

As it is non-interacting, the wave function of the auxiliary system will be given by a single Slater determinant of single particle orbitals $\varphi_i^{\text{KS}}(\mathbf{r})$, which are know as Kohn-Sham orbitals. This leads to a simple expression for the density of the non-interacting system

$$\rho_s(\mathbf{r}) = \sum_{i=1}^{N_{\text{elec}}} |\varphi_i^{\text{KS}}(\mathbf{r})|^2 \tag{2.8}$$

which we require by definition to be equal to the ground state density of the interacting system, i.e. $\rho_s = \rho_0$.

It is possible to write the energy functional from eq. (2.6) for the interacting system as

$$\begin{aligned} E_{\hat{H}_0}[\rho] =& T_s[\rho] + V^{\text{ext}}[\rho] + J[\rho] + E_{\text{xc}}[\rho] \\ =& -\frac{1}{2}\sum_{i=1}^{N_{\text{elec}}} \int \mathrm{d}\mathbf{r} \varphi_i^{\text{KS}*}(r) \nabla^2 \varphi_i^{\text{KS}}(r) - \int \mathrm{d}\mathbf{r} \sum_{j=1}^{N_{\text{at}}} \frac{Z_j}{|\mathbf{R}_j - \mathbf{r}|} \rho(\mathbf{r}) \\ &+ \frac{1}{2} \int \mathrm{d}\mathbf{r}\mathrm{d}\mathbf{r}' \frac{\rho(\mathbf{r})\rho(\mathbf{r}')}{|\mathbf{r} - \mathbf{r}'|} + E_{\text{xc}}[\rho], \end{aligned} \tag{2.9}$$

where $\tilde{H}_0$ is the Hamiltonian of the interacting system, $T_s[\rho]$ is the kinetic energy for the *non-interacting* system, $V^{\text{ext}}[\rho]$ the energy contribution from the external potential (of the original problem) and $J[\rho]$ is the Hartree term representing the classical (electrostatic) part of the electron-electron interaction. The exchange-correlation term $E_{\text{xc}}[\rho]$ contains all information for which no explicit functional form can be derived.

The Kohn-Sham orbitals φ_i^{KS} are solutions of the eigenvalue problem for the non-interactive auxiliary system. To derive them, it is necessary to find an expression for the effective external potential $v_s^{\mathrm{ext}}(\mathbf{r})$. This can be done using the variational principle arising from HK2 (cf. eq. (2.7)), namely

$$\left.\frac{\delta E_{\hat{H}_0}[\rho]}{\delta\rho}\right|_{\rho=\rho_0} = 0. \tag{2.10}$$

This leads to

$$v_s^{\mathrm{ext}} = v_0^{\mathrm{ext}}(\mathbf{r}) + \int \mathrm{d}\mathbf{r}' \frac{\rho(\mathbf{r}')}{|\mathbf{r}' - \mathbf{r}|} + v_{\mathrm{xc}}(\mathbf{r}), \tag{2.11}$$

where v_0^{ext} is the external potential for the interactive system, i.e. eq. (2.4), and

$$v_{\mathrm{xc}}(\mathbf{r}) = \left.\frac{\delta E_{\mathrm{xc}}[\rho]}{\delta\rho}\right|_{\rho=\rho_0} \tag{2.12}$$

is the exchange-correlation potential. Therefore, the Kohn-Sham orbitals can be obtained by solving

$$\left(-\frac{1}{2}\nabla^2 + v^{\mathrm{ext}}(\mathbf{r}) + \int \mathrm{d}\mathbf{r}' \frac{e^2\rho(\mathbf{r}')}{|\mathbf{r}' - \mathbf{r}|} + v_{\mathrm{xc}}(\mathbf{r})\right)\varphi_i^{\mathrm{KS}} = \epsilon_i \varphi_i^{\mathrm{KS}}, \tag{2.13}$$

which are the Kohn-Sham equations. As the effective potential depends on the density, which in turn depends on the occupied eigenfunctions φ_i^{KS}, the Kohn-Sham equations need to be solved recursively: from an initial guess of the density, the eigenproblem is solved for an updated density. This is repeated until self-consistency is achieved, i.e. until the change in the density between iterations is below a given tolerance.

In order to obtain eq. (2.9), all terms for which no explicit analytic expression is know where hidden in the $E_{\mathrm{xc}}[\rho]$ term. The success of DFT relies in part on the fact that the other terms in eq. (2.9) represent the largest contributions to the energy. If an exact expression for $E_{\mathrm{xc}}[\rho]$ was know, DFT would be able to provide the exact energy for the interacting system. In practice, it is necessary to find approximations. The simplest one used in practice is the local density approximation (LDA), for which the functional takes the form

$$E_{\mathrm{xc}}^{\mathrm{LDA}}[\rho] = \int \mathrm{d}\mathbf{r}\rho(\mathbf{r})\epsilon_{\mathrm{xc}}^{\mathrm{LDA}}(\rho(\mathbf{r})), \tag{2.14}$$

where the value of $\epsilon_{\mathrm{xc}}^{\mathrm{LDA}}(\rho(\mathbf{r}))$ is taken as the value corresponding to the homogeneous electron gas. This simple idea works surprisingly well to predict geometric properties (e.g. bond distances) of molecules and solids. However, binding energies arising from LDA calculations are typically less accurate. Therefore, more advanced approximations are needed to deal with problems in chemistry. In this work we employ the so-called generalized gradient approximation (GGA), in which the exchange correlation functional is of the form

$$E_{\mathrm{xc}}^{\mathrm{GGA}}[\rho] = \int \mathrm{d}\mathbf{r} f^{\mathrm{GGA}}(\rho(\mathbf{r}), \nabla\rho(\mathbf{r})), \tag{2.15}$$

i.e. information on the density gradient of reference systems is also included. Contrary to the LDA, there are several different versions of GGA functionals, depending on how f^{GGA} is defined. In this work we employ the popular functional by Perdew, Burke and Ernzerhof[33], known as PBE functional.

The calculations performed during the work on this thesis were done with CASTEP[34]. This software package implements DFT for periodic systems, uses plane waves to expand the KS orbitals and treats core electrons implicitly with pseudopotentials. These characteristics are favorable to deal with systems containing a periodic metallic surface, in which electrons are delocalized, such as those of interest in this thesis.

3 The mesoscopic scale and first-principles kinetic Monte Carlo

3.1 The separation of timescales and the master equation

Once a reliable way of evaluating the PES is available, simulating catalysis reduces in principle to solving the equations of motion arising from it. In particular, treating the motion of the nuclei classically is a good approximation, particularly in cases without hydrogen or other light atoms. This suggests the use of classical molecular dynamics (MD) simulations to sample the behavior of a catalyst: starting from several different initial conditions sampled from a thermal ensemble, the evolution of the systems could be propagated with the forces obtained from the PES. After enough simulations have been run for enough time, the desired properties, such as turnover frequencies (TOF) and overlayer configurations could be obtained.

In practice, this is not computationally feasible. On the one hand, the length scale of catalytic phenomena is an obstacle. As relevant length scales encompass tens of lattice constants at a minimum, first-principles based MD would be highly expensive. On the other hand, a more pressing problem is related to the separation of time scales. PESs for catalytic problems are characterized by the presence of several local minima (e.g as is illustrated in fig. 3.1.a). The *basins* defined by such minima are separated from each other by energy barriers that are typically much larger than the thermal energy of the system $k_{\mathrm{B}}T$. As a direct consequence of this, the resulting dynamics consists of large periods in which the system remains trapped inside the basins, interrupted by short transition periods in which it jumps between two basins. The long time spent in basins corresponds simply to the thermal vibrations of the reaction intermediates adsorbed on fixed lattice sites. The motion in these metastable states is of little relevance to the overall evolution of the catalytic cycle. In contrast, the movements *between* metastable states correspond to the *elementary reaction events* which actually move the reaction forward. These are the diffusional hops between adjacent adsorption sites, the adsorption (desorption) of intermediates from (to) the gas phase and the breaking and making of chemical bonds during surface reactions. Due to the high barriers, a typical period of metastable oscillation inside a basin is several orders of magnitude smaller than the total time spent inside basins. The elementary reaction events are therefore *rare events*. In order to simulate such a system with molecular dynamics, time steps need to be smaller than the oscillation timescale. Conversely, total simulation times need to be several times larger than the time between elementary reaction events. In some cases, millions of MD steps would be needed to observe a single reaction event. Considering that a huge number of such events are required for proper sampling, the computational cost

of running such simulation would still be prohibitively large even if the PES could be evaluated instantly.

Luckily, this large timescale separation can be turned into an advantage. Considering the relatively long time spent inside each basin, it is a reasonable approximation to assume that the system will have reached metastable equilibrium before performing a jump to the next basin. Once such metastable equilibrium is reached, the future dynamic evolution will only depend on the current basin the system sits on and not on the preceding trajectory. Thanks to this, a clear method to *coarse-grain* the description of the system's state arises. Instead of using the full phase space (i.e. the coordinates and velocities of the nuclei) to describe the state of the system, it is possible to use discrete states σ_i, one for each basin. We can thus define a mapping $\mathcal{C}$ from the phase space Ω to these coarse grained states

$$\begin{aligned} \mathcal{C} :\Omega \subset \mathbb{R}^{6N_{\text{at}}} &\rightarrow \{\sigma_1, ..., \sigma_{N_{\text{states}}}\} \\ P = (\mathbf{R}_1, , \mathbf{R}_{N_{\text{at}}}, \dot{\mathbf{R}}_1, ..., \dot{\mathbf{R}}_{N_{\text{at}}}) &\rightarrow \mathcal{C}(P), \end{aligned} \tag{3.1}$$

where N_{at} is the total number of atoms in the system and N_{states} is the number of basins in the PES. This is illustrated in fig. 3.1.b. This mapping is by definition not bijective, as many different points of the phase state will be mapped to the same discrete state. In the case of heterogeneous catalysis, the periodicity of the solid surface helps define the discrete states: the intermediates adsorb onto lattice sites that respect this periodicity. The minima of the PES correspond to the different possible arrangements of the (meta)stable intermediates in the lattice, i.e. which intermediate (if any) sits on each lattice site. This is illustrated in fig. 3.1.c.

Under the coarse-grained description, only a probabilistic treatment is possible. However, we can only hope to give a probabilistic treatment of catalysis anyway, as we can never pretend to know precisely the velocity and position of each atom on the catalyst and the intermediates in any realistic situation. A stochastic process with the characteristic described above, in which the system evolves between discrete states without memory of its previous trajectory, is a Markovian jump process[35]. Such processes are described by a master equation (ME)

$$\frac{\mathrm{d}p_i}{\mathrm{d}t}(t) = \sum_{\substack{j=0 \\ j\neq i}}^{N_{\text{states}}} (k_{ji}p_j(t) - k_{ij}p_i(t)) \qquad i = 1, ..., N_{\text{states}}, \tag{3.2}$$

where the $p_i(t)$ represents the probability of finding the system in state σ_i at time t and the coefficients k_{ij} are the *rate constants*, which represent the probability per unit of time of transitioning from state σ_i to σ_j. If we were able to solve the ME, the resulting probabilities $\{p_1(t), ..., p_{N_{\text{states}}}(t)\}$ would provide all the information necessary to characterize chemical kinetics, including TOF and coverage patterns. The ME is generally a matrix differential equation of extremely high dimensionality though, as the number of states N_{states} is huge even for the simplest examples in heterogeneous catalysis. For example, a square lattice of (10×10) sites in which a single type of adsorbates can

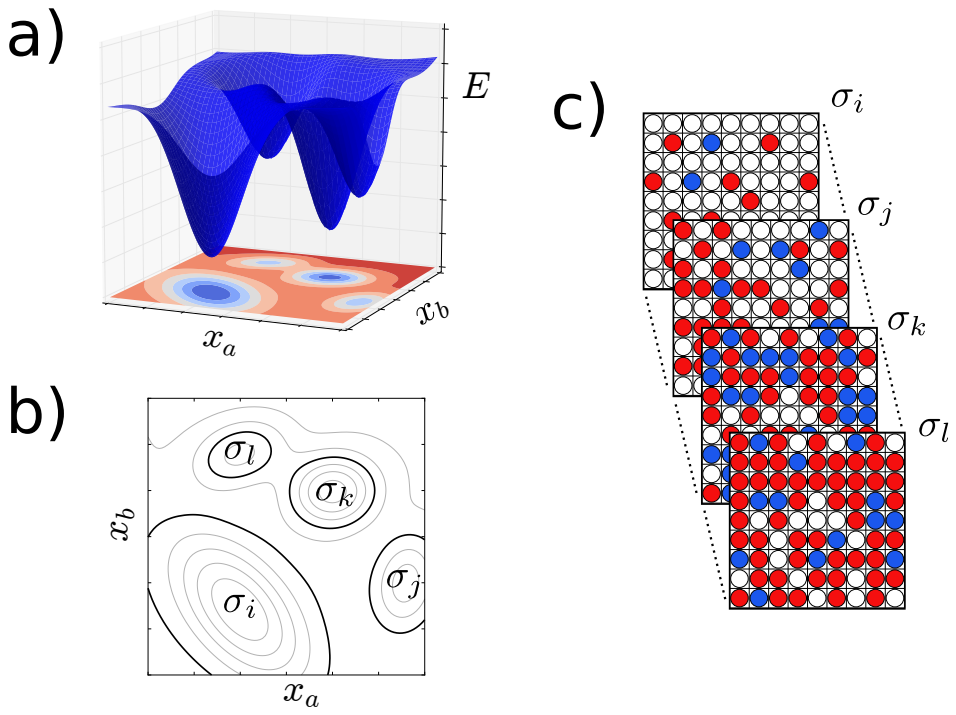

Figure 3.1: a) A 2D cut of a PES. A system with thermal energy $k_\mathrm{B}T$ much smaller than the depth of the basins will evolve with *rare event* dynamics. b) Contour lines for the PES (gray lines) with the coarse-grained discrete states associated to each basin indicated with black lines. c) In heterogeneous catalysis applications, a coarse-grained discrete state exists for each possible way of filling the surface lattice with the different (meta)stable intermediates.

sit leads to $N_\mathrm{states} = 2^{100} \approx 1 \times 10^{30}$. Correspondingly, the number of rate constants k_{ij} is N_states^2.

Luckily, in the case of heterogeneous catalysis, the number of *different* rate constants is much smaller than that. Firstly, rate constants connecting basins located far away from each other in the configuration space can be treated as zero, as the probability of the system transitioning directly between two such basins will be extremely small compared to rate constants connecting close laying basins. For example, this would correspond to a diffusional hop of an adsorbate between adjacent lattice sites versus a direct hop across distant sites. Clearly, there will be a maximum distance after which direct hops become highly improbable. Secondly, the symmetry of the lattice can be exploited to further reduce the number of different positive rate constants, i.e. processes representing the same *elementary reaction step* (in the same chemical environment) will have equal rate constants, regardless of their specific location in the lattice.

In addition, rate constants for physical systems need to satisfy relations known as *detailed balance*. To derive them, we consider our system in the steady state: the probabilities $p_j(t)$ are independent of time, i.e. $p_k(t) = p_k^\mathrm{eq}$, $dp_k(t)/dt = 0$. The ME, eq. (3.2),

reduces to

$$\sum_{\substack{j=0 \\ j\neq i}}^{N_{\text{states}}} \left(k_{ji} p_j^{\text{eq}} - k_{ij} p_i^{\text{eq}} \right) = 0. \tag{3.3}$$

As this relation must be valid for each state, i.e. for $0 < i \leq N_{\text{states}}$, this can only be satisfied if each of the terms in the sum are zero, i.e. if

$$k_{ji} p_j^{\text{eq}} = k_{ij} p_i^{\text{eq}} \quad \forall \quad 0 < i, j \leq N_{\text{states}}. \tag{3.4}$$

If the system is in equilibrium at constant temperature T and constant chemical potentials (i.e. the Grand Canonical ensemble), we have

$$p_i^{\text{eq}} \propto e^{-G_i / k_{\text{B}} T}, \tag{3.5}$$

where G_i is the Gibbs free energy of the system in state i. Eqs. (3.4) and (3.3) lead to

$$\frac{k_{ij}}{k_{ji}} = \exp\left(-\frac{G_j - G_i}{k_{\text{B}} T} \right) \quad \forall \quad 0 < i, j \leq N_{\text{states}}. \tag{3.6}$$

Relations (3.6) define the conditions for detailed balance (also sometimes referred as microscopic reversibility) and are valid even when the system is not in equilibrium.

3.2 Solving the master equation: kinetic Monte Carlo (kMC)

Even taking into account the reduction in the number of individual rate constants described above, a direct numerical solution of the ME is still impossible due to the high dimensionality. Alternatively, it is possible to sample the Markov process directly by simulating a random walk across the states σ_i, guided by the transition probabilities k_{ij}. Such procedure is known as kinetic Monte Carlo (kMC).

The result of an individual kMC simulation is a sequence of states and time intervals between the transitions from state to state. By averaging several of such *stochastic trajectories*, the $p_i(t)$ can be sampled. In practice, however, the quantities of interest for heterogeneous catalysis, such as TOFs and coverage patterns, can be sampled directly from the kMC trajectories.

Fig. 3.2 represents an intuitively simple version of an algorithm to obtain a kMC trajectory. Under the Markovian approximation, the probability per unit time of escaping from a given state σ_i to another given state σ_j is given by the rate constant k_{ij}. This leads to a probability distribution for the time of first escape *towards such basin*

$$p_{ij}^{\text{escape}}(t) = k_{ij} e^{-k_{ij} t}. \tag{3.7}$$

We can simulate the stochastic jump process by drawing escape times for each reachable process $\sigma_j \neq \sigma_i$ according to distribution (3.7). This can be done by drawing uniformly distributed random numbers $\rho_j \in (0, 1]$ and taking $\tau_j = -\ln(\rho_j)/k_{ij}$ as the times of

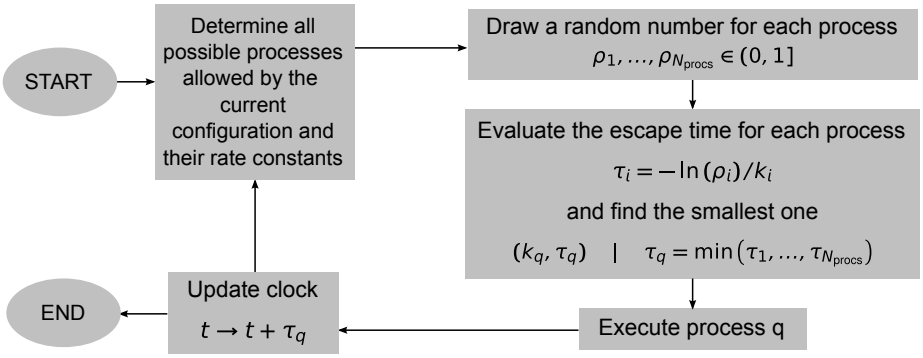

Figure 3.2: The first reaction kinetic Monte Carlo algorithm.

escape. The process with the shortest τ_j determines the time interval and the state to which the system moves.

In this thesis, we employ an alternative kMC algorithm: the so-called *direct* algorithm. It has the advantage of only requiring the generation of two random numbers per step. This is based on the facts that: (a) The probability distribution of the time of first escape from state σ_i to *any* other state is given by

$$p_i^{\text{escape}}(t) = k_i^{\text{tot}} e^{-k_i^{\text{tot}} t}, \tag{3.8}$$

where

$$k_i^{\text{tot}} = \sum_{\substack{j=1 \\ j \neq i}}^{N_{\text{states}}} k_{ij} \tag{3.9}$$

is the sum of all rates constants for escaping state σ_i; and (b) the probability of the system escaping towards a given state σ_j is k_{ij}/k_i^{tot}. This can be exploited to employ the algorithm depicted in figure 3.3. In this case, given two uniformly distributed random numbers $\rho_1, \rho_2 \in (0, 1]$, the next state to be visited is chosen according to

$$\sigma_q \quad | \quad k_i^{\text{sum}}(q) < \rho_1 k_i^{\text{tot}} \leq k_i^{\text{sum}}(q+1), \tag{3.10}$$

where

$$k_i^{\text{sum}}(q) = \sum_{\substack{j=1 \\ j \neq i}}^{q} k_{ij} \tag{3.11}$$

is a partial sum of rate constants (clearly $k_i^{\text{sum}}(N_{\text{procs}}) = k_i^{\text{tot}}$). Once the process has been chosen, the time for the step is then drawn from distribution (3.8) according to

$$\tau = -\frac{\ln \rho_2}{k_i^{\text{tot}}}. \tag{3.12}$$

The direct kMC algorithm is more efficient than the first reaction algorithm in cases where the number of *different* rate constants is small and constant in time. Using

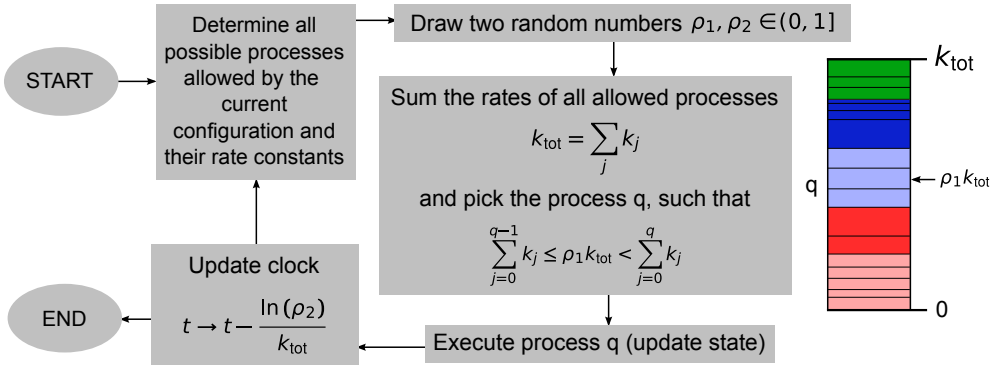

Figure 3.3: The direct kinetic Monte Carlo algorithm

appropriate data structures, the selection of the next time step can be made in *constant time* with respect to the size of the simulation lattice. All kMC simulations in this work were performed using the kmos framework, which takes advantage of such scaling. kmos is a free and open source software package authored by Max J. Hoffmann[36]. It consists of a user-friendly Python interface that facilitates the generation of an abstract model definition, which is then used to automatically generate efficient Fortran code. A Python interface to run and analyze results is also provided. While performing the research that led to this thesis, I have also contributed extensively to the development of the kmos framework. Besides the official documentation[37], the reader is encouraged to take a look at the introductory lecture notes which I co-authored[38].

3.3 Getting the rate constants: transition state theory

In our discussion of the kMC method, the rate constants have entered as input parameters. In early kMC studies, the rate constants have been guessed from chemical intuition or simply used as adjustable parameters[39, 40]. However, the rate constants are simply a property of the underlying system's dynamics and thus a function of the PES. Therefore, it is possible to use a PES based on first principles to obtain kMC models which are both material specific and free of empirical parameters. Such methodology is known as first principles kMC (1p-kMC)[41, 18, 19, 6].

The straightforward way to evaluate the rate constants k_{ij} would be to directly sample the system's dynamics. Running several molecular dynamics simulations would allow for the sampling of time of escape distributions from which the k_{ij} could be evaluated. Due to the separation of time scales discussed in section 3.1, this is prohibitively expensive. Direct calculation of the rate constants would negate the improvement in efficiency provided by the kMC method.

In practice, approximate methods can be used for a much more efficient evaluation of rate constants. The most widely used approximation is transition state theory (TST)[42]. In TST, the rate constants k_{ij} are approximated by the equilibrium (normalized) *forward* flux across a (hyper-)surface separating the PES basins associated to states σ_i and

σ_j. This approximation overestimates the values of the k_{ij}: it is assumed that each forward crossing of the dividing surface corresponds to a reactive event, i.e. re-crossings are neglected. However, TST rate constants can be expressed as ensemble-averages and can be evaluated through equilibrium-sampling methods such as Metropolis Monte Carlo[42, 43].

In this work, we employ a further approximation known as harmonic TST (hTST). In hTST, the dividing surface is defined as a hyper-plane that goes through the highest energy point along the minimum energy path (MEP) connecting the minima $\mathbf{x}_i$ and $\mathbf{x}_j$ associated to the basins σ_i and σ_j. Such point is known as the *transition state* (TS) and will be denoted by $\mathbf{x}_{ij}^{\mathrm{TS}}$. It corresponds to a saddle point of the PES in which the Hessian (the matrix of second partial derivatives) has a single negative eigenvalue. The dividing plane is taken perpendicular to the direction of this eigenvalue. The hTST rate constants are calculated based on the hypotheses that (a) the probability of finding the system in a close vicinity of the bottom of the initial basin (i.e. close to local minimum $\mathbf{x}_i$) is much larger than the probability of finding it anywhere else within the basin; (b) that crossings occur through points close to $\mathbf{x}_{ij}^{\mathrm{TS}}$ with a much higher probability than through any other point in the dividing surface; and (c) that the PES can be approximated by quadratic functions around $\mathbf{x}_i$ and $\mathbf{x}_{ij}^{\mathrm{TS}}$. Under these conditions, a formula for the rate constant can be derived that depends only on the shape of the PES at the bottom of the basin and at the TS, namely

$$k_{ij}^{\mathrm{hTST}} = \frac{k_{\mathrm{B}}T}{h}\frac{Z_{ij}^{\mathrm{TS}}}{Z_i}\exp\left(-\frac{\Delta E}{k_{\mathrm{B}}T}\right), \tag{3.13}$$

where Z_{ij}^{TS} and Z_i are the vibrational partition functions at $\mathbf{x}_i$ and $\mathbf{x}_{ij}^{\mathrm{TS}}$, respectively; and $\Delta E = E_{ij}^{\mathrm{TS}} - E_i$ is the energy difference between these two positions: the reaction barrier. In this way, the calculation of the rate constants requires only the evaluation of properties of the system at the minimum and the TS.

In this work, we have evaluated the rate constants using the approach put forward by Reuter and Scheffler, which was introduced in reference [41]. For bound-to-bound processes, the ratio of the partition functions is approximated as $Z_{ij}^{\mathrm{TS}}/Z_i \approx 1$, as the vibrational properties at the minimum and the TS are expected to be similar. Therefore, rate equations for diffusion and reaction processes are calculated using

$$k_{ij} = \frac{k_{\mathrm{B}}T}{h}\exp\left(-\frac{\Delta E}{k_{\mathrm{B}}T}\right). \tag{3.14}$$

For processes of adsorption, the gas phase is treated as a reservoir composed of a mixture of N_{spec} ideal gas species of molecular masses m_i at constant partial pressures p_i and constant temperature T. The rate of adsorption of species i into a given site s in the surface unit cell can be modeled as

$$k_{i,s}^{\mathrm{ads}} = S_{i,s}(T)I_i(p_i, T), \tag{3.15}$$

where

$$I_i(p_i, T) = \frac{p_i A}{\sqrt{2\pi m_i k_{\mathrm{B}}T}} \tag{3.16}$$

is the impingement rate of molecules of species i into the unit cell's surface area A and $0 < S_{i,s}(T) < 1$ plays the role of a local sticking coefficient. Employing the hole model for adsorption, we assume that only molecules impinging at lateral position within a given area A_s around the site s will be steered towards it. In a classical picture, molecules need to have energy higher than the barrier they encounter when impinging on the surface. If all molecules had to overcome the same barrier ΔE, we would have $S_{i,s}(T) = (A_s/A)\exp(-\Delta E/k_{\mathrm{B}}T)$. Therefore, we can approximate

$$S_{i,s}(T) = f_{i,s}(T)\frac{A_s}{A}\exp\left(-\frac{\Delta E_{i,s}^{\mathrm{ads}}}{k_{\mathrm{B}}T}\right), \tag{3.17}$$

where $\Delta E_{i,s}^{\mathrm{ads}}$ is highest barrier in the MEP, i.e. the adsorption barrier, and the factor $0 < f_{i,s}(T) \leq 1$ accounts for the error due to adsorption attempts through paths with higher barriers than the MEP. In the moderate temperatures used in this work, the kinetic energy of the impinging particles is not too high and we can expect them to be efficiently steered into the MEP. Therefore we take $f_{i,s} \approx 1$ for all adsorption processes. In the specific case of the simultaneous CO and NO oxidation model constructed for this thesis, all adsorption processes are non-activated: i.e. all adsorption barriers are zero. Therefore, the formula for adsorption rates used in that case is

$$k_{i,s}^{\mathrm{ads}} = \frac{p_i A_s}{\sqrt{2\pi m_i k_{\mathrm{B}}T}}. \tag{3.18}$$

The values of the areas A_s were calculated by evenly dividing the total unit cell area A among all adsorption sites available to the corresponding adsorbate.

Considering the desorption processes as reverse adsorption processes, we can use detailed balance to get

$$\frac{k_{i,s}^{\mathrm{ads}}}{k_{i,s}^{\mathrm{des}}} = \exp\left(\frac{\Delta G_{i,s}(T,p_i)}{k_{\mathrm{B}}T}\right), \tag{3.19}$$

where $\Delta G_{i,s} = G_{i,s}^{\mathrm{gas}} - G_{i,s}^{\mathrm{ads}}$ is the difference in Gibbs free energy between the state with the molecule in the gas phase and the state with the molecule adsorbed. The Gibbs free energy of the gas phase state will be given by the chemical potential of the gas $G_{i,s}^{\mathrm{gas}} = \mu_i(T,p_i) = E_{i,\mathrm{gas}}^{\mathrm{tot}} + \Delta\mu_i(T,p_i)$, where $E_{i,\mathrm{gas}}^{\mathrm{tot}}$ is the total energy of the molecule in the gas phase. Values for $\Delta\mu_i(T,p_i)$ can be easily obtained by interpolating available tabulated values[44]. For small molecules in a chemisorbed state, the entropic contributions to the free energy are small, and can be neglected. We thus approximate the free energy in the bound state with the corresponding total energy: $G_{i,s}^{\mathrm{ads}} \approx E_{i,s}^{\mathrm{tot}}$. Under these approximations, eq. (3.20) reads

$$\frac{k_{i,s}^{\mathrm{ads}}}{k_{i,s}^{\mathrm{des}}} = \exp\left(\frac{\Delta\mu_i(T,p_i) - E_{i,s}^{\mathrm{bind}}}{k_{\mathrm{B}}T}\right), \tag{3.20}$$

where we introduced the binding energy of the molecule i on site s: $E_{i,s}^{\mathrm{bind}} = E_{i,s}^{\mathrm{tot}} - E_{i,\mathrm{gas}}^{\mathrm{tot}}$. Therefore, the formula for the desorption rates results

$$k_{i,s}^{\mathrm{des}} = k_{i,s}^{\mathrm{ads}} \exp\left(\frac{E_{i,s}^{\mathrm{bind}} - \Delta\mu_i(T, p_i)}{k_{\mathrm{B}}T}\right). \tag{3.21}$$

3.4 Uncertainties in 1p-kMC models

The methods used to derive the rates are evidently only approximate. Although it would be possible to lift many of the approximations outlined in section 3.3, this would not alleviate the main source of error on the rates: the DFT-PES itself. Barriers calculated using GGA functionals can have errors of ~ 0.2 eV. Considering that the barriers enter the rate expressions exponentially, this can lead to errors of up to a couple orders of magnitude in the rates. It is currently not possible to go beyond a GGA level of theory for systems as those addressed in this thesis, as obtaining all the necessary barriers would be extremely computationally expensive with any significantly more accurate method. For this reason, current 1p-kMC are not typically able to reach exact quantitative agreement with experiment and only qualitative agreement can be expected. Local[14] and global[45] sensitivity analysis methods exist which allow to quantify the effect of these errors on the predicted rates. However, this is outside the scope of this thesis.

Another source of error in kMC models (in catalysis and other areas) is related to the model definition itself. When constructing a 1p-kMC model, transitions judged to be unlikely are simply excluded from the process list. These typically include e.g. adsorption into less favorable lattice sites, long-distance diffusional hops, or any process that presents very high barriers. In addition, it is typically impossible to find all minima in a DFT-PES and all connecting transition states in an automatic fashion due to the extreme amount of computational power this would require. In principle, also the effects of different chemical environments surrounding the reacting intermediate should be taken into account. These lateral interaction effects can increase the amount of minima and barrier calculations drastically, making only approximate methods feasible[27, 21, 46].

Experimental input can help with these issues. Although the fitting of rate constants to experimental results can easily lead to wrong microscopic insight[16], direct experimental observations can clearly provide crucial insight. Observations such as the presence of specific intermediates or the selectivity towards a certain product can be directly compared to kMC simulations[4, 5].

4 NO and CO oxidation at Pd(100)

Platinum group metals (PGM) are of great interest in catalysis mainly because they are a key component of automotive catalytic converters. The majority of the global production of Platinum, Palladium and Rhodium is used for such end[47]. Pd is considerably cheaper than Pt and there has been significant growth in its use in automotive catalysis[48]. The three most important exhaust products are carbon monoxide, the nitrogen oxides NO and NO_2 (collectively symbolized as NO_x), and hydrocarbons (HC). Modern three-way catalytic converters (TWC) can efficiently treat these exhaust components by oxidizing CO and HC and reducing NO_x.

Engines that operate using a higher air-to-fuel ratio (such as diesel engines and so called *lean-burn* gasoline engines) present a challenge for traditional TWCs. Under the oxygen excess conditions of these exhausts, it becomes difficult to fully reduce NO_x. As these types of engines can provide increased fuel efficiency (and thus reduced total emissions), it is desirable to develop catalytic technology that can properly treat their exhausts. Nitrogen Storage Reduction (NSR) relies on cyclic engine operation, switching between longer fuel-lean cycles during which NO is oxidized into NO_2 and stored in a carrier material, and fuel-rich bursts in which all NO_2 is reduced[49, 50]. For this application, the capabilities of PGMs for NO oxidation in oxygen-rich environments are of interest.

In the context of technical catalysis research, several studies have been performed on supported catalysts and their effect on mixtures closely resembling lean-burn or diesel exhausts[51, 52, 53, 54, 55, 56, 57]. Of particular interest for this work are studies which focus on the effect CO presence has in NO oxidation, and vice versa. Early studies initially suggested that the interaction of both oxidation pathways have inhibiting effects on each other[58, 55, 59]. However, there have also been indications of synergistic effects[59, 54]. For example, Boubnov and collaborators[54] studied simultaneous oxidation of CO and NO over Pt/Al_2O_3 catalysts. They found that the presence of NO is favorable for CO oxidation in the initial stages of the reaction, a result attributed to the presence of active surface oxide species produced during NO oxidation. They also observed steady-state NO oxidation rate to be significantly higher when CO is present in the mix, which was attributed to the regeneration of oxidized catalysts by CO.

The different observations found in literature clearly demonstrate that the synergistic/inhibiting effects of these oxidation processes arise from complex kinetics. In the context of the experiments discussed above, where supported catalysts and complex gas mixtures were employed, several factors will have an effect on the final observations. These include: the specific composition of the input gas mixture, the details of the composition and microstructure of the catalyst used, the geometry of the reaction chamber, as well as other effects outside the control of the researchers, such as nanoparticle sin-

tering. This situation motivates the complementary pursuit of a bottom-up approach. In this spirit, focusing on single-crystal model catalysts and simpler gas mixtures, it is possible to reach a more complete understanding of kinetic effects.

In this work, we have focused on the Pd(100) crystal facet, for which several detailed microscopic studies have been performed, from UHV to near ambient pressures. Goodman and collaborators[60, 61, 62], using a variety of experimental techniques, characterized a set of ordered CO and NO coverage-dependent over-layers on various Pd single crystal surfaces. The interaction of CO and NO with Pd surfaces has been investigated in various DFT studies [63, 64, 65, 66, 67, 68, 69]. In particular, the nature of the Pd(100) surface under oxygen rich conditions and at higher pressures has also attracted attention. However, information is mostly available in the context of CO oxidation (without NO). Additionally to the plain metal surface, various surface oxide terminations, including a subnanometric $(\sqrt{5} \times \sqrt{5})$ surface oxide, have been proposed[26, 70, 71, 72]. Rogal, Reuter and Scheffler compared the relative stability of different terminations of the Pd(100) surface in a mixture of CO and O_2 using first principles thermodynamics[26]. They found that both the pristine metallic termination and the $(\sqrt{5} \times \sqrt{5})$ surface oxide termination could be stable under relevant reaction conditions. Oscillatory behavior between these phases that was observed in kinetic experimental studies [28] and could be explained through the analysis of 1p-kMC models of CO oxidation, which indicated the existence of a bistability region [20, 21]. In-situ spectroscopic studies confirmed both phases to be catalytically active and suggested that the formation of bulk oxide is kinetically hindered even at relatively high temperatures [3, 4]. The effects of gas-phase transport limitations have only recently entered the discussion, and it was found that these play a prominent role also for single crystal catalysts [70, 73].

Regarding NO oxidation conditions, Jelic and Meyer[74] employed first principles thermodynamics to obtain the surface phase diagram of Pd(100) and Pd(111) in contact with NO and O_2 mixtures. Jelic and collaborators[22] then developed a 1p-kMC model for the $(\sqrt{5} \times \sqrt{5})$ termination which showed high efficiency for NO oxidation under an oxidizing feed, supporting the suitability of Pd oxides for NSR catalysis. Smeltz et al. [75] studied NO oxidation at Pt(111) in a batch reactor and performed *ex situ* X-Ray photoelectron spectroscopy and Auger electron Spectroscopy. Various theoretical mean-field[76, 77] and 1p-kMC[78, 23] models have been developed for this reaction. Among other results, these studies have found that lateral interactions play an important role in the oxidation kinetics.

A common denominator of such detailed single-crystal studies is that they typically focus on the oxidation of a single component, i.e. either CO or NO, as a way to reduce the complexity of the problem. Considering the varied inhibition and/or synergy effects observed in supported catalysts experiments, exploring the interaction of NO and CO oxidation pathways in a detailed fashion becomes of interest. This was the focus of the first publication included in this thesis, summarized in section 6.1.

5 Coupling to the macroscopic scale

Fluid dynamics models that incorporate heterogeneous catalysis are established in the field of technical catalysis and are a crucial part of the process of reactor design[79]. To solve flow problems computationally, different schemes such as finite difference (FDM), finite volume (FVM) or finite element methods (FEM) can be used according to the nature of the geometries and flow patterns. All these methods provide a way of *discretizing* the problem, by subdividing the spatial domain into small *cells* and the time into a set of discrete intervals. In this way, the partial differential equations (PDEs) that govern the fluid dynamics (i.e. the Navier-Stokes equations) are transformed into algebraic equations that can be solved computationally. The effects of the catalyst enter the problem as boundary conditions for the PDEs

$$\phi_i = \phi_i(\mathbf{r}, t) \qquad i = 1, ..., N_{\text{spec}}, \tag{5.1}$$

where the ϕ_i represent the mass flow per unit area and unit time of species i entering (or exiting) the fluid cell due to the catalytic reaction, $\mathbf{r}$ represents a position on the a catalyst's surface, and t is the time. The ϕ_i are simply proportional to the TOFs determined by the microkinetic model, where the proportionality constant is simply the molecular mass of the corresponding gas species.

When the chemical kinetic models used are based on rate equations it is possible to treat the ϕ_i under the same discretization scheme as the fluid equations. This cannot be done when 1p-kMC is used, because this method does not provide a set of closed differential equations (as the ME, eq. (3.2), is not explicitly solved). Therefore, special coupling schemes are needed in this case. A straightforward way of doing this is to solve each problem separately within small time intervals, alternating between fluid steps and catalysis steps and communicating the results in between. Such direct coupling approach has been used by Vlachos[80] and Kissel-Osterrieder et al.[81] for one-dimensional transport (zero-dimensional surface) models and empirical kMC models. Majumder and Broadbelt[82] extended these methods to a problem with a one-dimensional surface, employing a simple model mechanism.

There are several limitations to the application of direct coupling, especially for problems with arbitrary geometries and/or dealing with complex chemistry. One of them is simply the high computational cost, as kMC can be several orders of magnitude more expensive than rate equation-based approaches. Needing to perform an independent kMC simulation for each fluid cell in contact with the catalyst and for each time step can easily become a computational bottleneck. Furthermore, being a stochastic approach, kMC generates results which contain statistical noise, which can make the coupled simulation unstable[83]. This is aggravated in cases in which the derivatives of the boundary conditions are required, since noise can can drastically increase the error of numerical

derivatives. Reducing statistical noise can only be achieved by performing more kMC simulations, which increases computational costs even more.

Several strategies have been developed to alleviate these difficulties. Robust control methods[84] have been employed to reduce instabilities caused by stochastic noise. To reduce the amount of kMC calculations necessary, approaches such as in-situ adaptive tabulation[85] or the gap-tooth method[82] can be used. The former keeps results from performed kMC simulation in a database and only executes additional simulations if an interpolation of stored values is judged not to be accurate enough. In the latter coupling approach, the catalyst's surface is divided into small sub-domains (*teeth*), in which kMC simulations are explicitly performed, and larger separating regions (*gaps*), in which reactivity is obtained via the interpolation of the results from the teeth. Although these methods are promising, direct coupling of kMC and CFD is currently still limited to simplified geometries and/or phenomenological reactivity models.

All these limitations of direct coupling can be avoided provided one additional approximation is valid: the instantaneous steady state approximation. In most cases of interest, the time the catalyst takes to reach its steady-state is much smaller than the timescale of change of the macroscopic fluid problem. In those cases, it can be assumed that whenever the gas phase conditions over the catalyst change, the reaction rates will immediately adapt to the steady-state rates under the new conditions. This approximation dramatically simplifies the problem at hand, as now boundary conditions on the catalyst can be described as a function of the partial pressures of the different gas species p_j, $j = 1, ..., N_{\text{spec}}$, and the temperature T directly on top of the catalyst:

$$\phi_i = \phi_i(\mathbf{r}, t) = r_i(p_1(\mathbf{r}, t), ..., p_{N_{\text{spec}}}(\mathbf{r}, t), T(\mathbf{r}, t)) \qquad i = 1, ..., N_{\text{spec}}. \tag{5.2}$$

In this situation, a valid strategy is to precompute a database of steady-state TOF values for a range of partial pressure and temperature values that covers the values expected during the simulation. Such database can then be used to generate a continuous representation of the r_i functions through interpolation. If the interpolation is fast to evaluate, the 1p-kMC/CFD coupled simulation can be made as efficient as simulations based on rate-equation microkinetic models. Such an interpolation-based scheme has been put forward by Matera and Reuter[8, 9] and has even been used to simulate complex flow dynamics found in in-situ reactivity experiments[30, 5].

Under this scheme, the main challenge is finding an interpolation method that can be evaluated quickly and that can be constructed with an initial database of 1p-kMC simulations that is not too large. The latter part is challenging due to the nature of the steady state 1p-kMC reactivity maps. Such functions are best represented under the transformation of coordinates

$$\begin{aligned} (p_1, ..., p_{N_{\text{spec}}}, T) \rightarrow \quad & \mathbf{x} = (\log(p_1), ..., \log(p_{N_{\text{spec}}}), \frac{1}{T}) \\ r_i \rightarrow \quad & f_i = \log(r_i), \end{aligned} \tag{5.3}$$

i.e. logarithmic scale in the pressures and mass flow and inverse scale in temperature. In the transformed coordinates the f_i present a smooth, almost linear behavior on large

regions of their domain. Such regions correspond to steady-state kinetic phases, characterized by a defined coverage regime on the catalyst. In contrast, they present highly non-linear behavior in the boundaries between such regions. Typically, such transition regions are relatively localized and present sharp changes in the function values and/or its gradient. In principle, a high density of points is needed there to get an interpolant of decent quality. This problem is aggravated when the number of species becomes large. The domain of functions f_i is of dimension $D = N_{\text{spec}} + 1$. The number of points needed to densely sample a volume of space grows exponentially with the dimension: the number of points on a grid of a given resolution n in each dimension is equal to n^D. This is known as the *curse of dimensionality* and makes it challenging to densely sample the highly non-linear regions of the reactivity maps, as a very large number of 1p-kMC simulations would in principle be needed.

In this thesis, we have developed an extension of the modified Shepard interpolation method that uses a set of automatically generated local metrics to alleviate the problem of the curse of dimensionality. This is presented in the second included paper, which is summarized in section 6.2.

6 Publications summaries with details of contributions

6.1 Paper 1: Synergistic inhibition of oxide formation in oxidation catalysis: A first-principles kinetic Monte Carlo study of NO + CO oxidation at Pd(100)

Authors: J. M. Lorenzi, S. Matera and K. Reuter. Published in ACS Catalysis, Volume 6, Number 8, Pages 5191-5197, July 2016. DOI: 10.1021/acscatal.6b01344.

Summary

This paper presents a 1p-kMC model of simultaneous oxidation of CO and NO by O_2 on a single-crystal Pd(100) catalyst. The model is based on an extensive set of DFT calculations. The effect of the strong lateral interactions are incorporated using blocking rules. The analysis in the paper focused on studying the effects of the presence of NO on CO oxidation kinetics. For conditions in which the Pd surface is most active towards CO oxidation, i.e. at CO/O_2 ratios close to stoichiometry, predicted activity is reduced when NO is present. A markedly different result was found for the case of oxygen-rich feeds. Under such conditions, the surface is predicted to be fully oxygen poisoned in the absence of NO, indicating the formation of a surface oxide. Interestingly, the addition of only small amounts of NO ($\sim 10^{-5}$ bar) drastically reduced the steady-state O coverage and increased CO oxidation activity. This suggests that small amounts of NO could stabilize the pristine metal phase of Pd(100) by limiting the amount of oxygen adatoms and thus inhibiting oxidation. Through the analysis of modified versions of the kinetic model details on the nature of this synergistic effect where revealed to be quite intricate. Turning off NO oxidation from the model suppressed the enhancing effect on CO oxidation, demonstrating that this effect goes beyond simple coadsorption effects. In addition, simulations under other modified versions of the model demonstrated that both the generation of empty sites through NO_2 desorption as well as an NO_2-mediated O-diffusion mechanism are responsible for the onset of the oxidation inhibition at such low NO partial pressures.

Author contributions

This project was carried out in collaboration with Dr. S. Matera, currently at the Mathematics Department of the Freie Universität Berlin. Dr. Matera originally proposed the project while he was still working as a postdoctoral fellow in the Lehrstuhl

für Theoretische Chemie. He provided scientific advise throughout the project. Prof. Dr. Karsten Reuter closely supervised the project and provided critical scientific input regarding both the construction of the model and the analysis of the results. He also contributed significantly to the co-writing and editing of the manuscript.

I performed all DFT calculations the 1p-kMC model is based on, including all binding energy evaluations, transition state searches and the extensive analysis of the lateral interactions used to justify the blocking-rules scheme used. I also defined the 1p-kMC model conceptually and implemented it using the kmos simulation framework. In addition, I performed all 1p-kMC simulations presented in the paper, prepared all figures and co-wrote the manuscript.

6.2 Paper 2: Local-metrics error-based Shepard interpolation as surrogate for highly non-linear materials models in high dimensions

Authors: J. M. Lorenzi, T. Stecher, K. Reuter and S. Matera. Submitted to the Journal of Chemical Physics.

Summary

This paper presents a novel scattered data interpolation method. The method aims at interpolating high dimensional functions which present concentrated regions of highly non-linear behavior but are smooth in the rest of the domain. Normally a very large amount of data points would be needed to properly interpolate such functions, as the non-linear regions would need to be sampled densely and the amount of points needed to densely sample a region of space grows exponentially with dimension (i.e. the effect known as *the curse of dimensionality*). The method presented in this work is based on the modified Shepard (MS) interpolation. Interpolants are constructed as weighted sums of linear local approximations centered at the points in the database (nodes). The novel element in our approach is the fact that the weights are based on local metrics. These local metrics are generated automatically according to the input data in the vicinity of each node. Using a collection of challenging analytic functions, we showed that the method can provide remarkably good interpolations even when using very small data sets. We tested dimensions from 2 to 7 and compared our method to different versions of MS as well as to the state of the art Gaussian Processes Regression (GPR) method. In all cases our method resulted superior. In addition, we also interpolated a 7-dimensional TOF function arising from a 1p-kMC model, as this application originally motivated this project. In this case we also found the method to provide qualitatively very good results for very small data sets ($\approx$ 1024 points) and quantitatively good results for moderately large date sets ($\approx$ 8192 points). An additional advantage of the model is that its mathematical formulation is conceptually simple and based solely on geometrical considerations. In addition, all adjustable parameters either have a geometrical interpretation or represent an error scale. We are optimistic that these characteristics will make the

method easy to apply by researchers that are not necessarily experts in interpolation methods.

Author contributions

Dr. Sebastian Matera proposed the conceptual basis for the interpolation method, closely supervised the project and provided scientific guidance. In addition, he provided the implementation of the 1p-kMC model used for testing and contributed to the writing and editing of the manuscript. Prof. Dr. Karsten Reuter also supervised the work and contributed to the writing of the manuscript. Dr. Thomas Stecher performed all GPR calculations used for testing and wrote the corresponding parts of the manuscript. He additionally helped with the proofreading of the manuscript.

I developed the algorithm for the interpolation method. To achieve this, I performed extensive testing of different strategies for the generation of the local metrics. This was facilitated by my implementation of the interpolation routines as a modular Python package, in which computationally demanding routines where included as C-extensions. In addition, I designed the set of analytic test functions and generated all the input data necessary for the tests, including the 1p-kMC calculations. Moreover, I constructed all MS-based interpolants, evaluated the error of each of them, performed all data analysis, wrote the majority of the manuscript and generated all figures.

7 Summary and outlook

This thesis focused on the multiscale modeling of heterogeneous catalysis beyond typical simplified reaction pathways. The first part has explored interaction effects between CO and NO oxidation reaction pathways. This was motivated by the potential importance of such effects in the context of Nitrogen Storage Reduction catalysis, as observed in earlier experiments done under technically realistic conditions. A detailed first principles kinetic Monte Carlo model of the reactions occurring simultaneously at a Pd(100) single crystal catalyst was built. The model showed that both reactions interact in non-trivial ways, particularly indicating that the presence of small amounts of NO could have a strong oxidation-inhibiting effect. This suggests that observations from fundamental studies focusing on the nature of the active phase of platinum group metals under CO oxidation conditions cannot easily be extrapolated to more realistic conditions where the gas phase contains more species. The effects observed are the consequence of rather complex kinetic effects, which could only be elucidated thanks to the detailed modeling.

The importance of such complex kinetic effects even for simple model catalysts highlights the importance of advancing methodology which can simplify and accelerate the comparison of theory and experiment. This thesis has contributed to this by extending an existing multiscale 1p-kMC/CFD framework. Multiscale modeling is crucial to properly interpret in-situ experiments, in which mass and heat transfer effects are important. The contribution in this work consisted of an improved interpolation method based on the popular modified Shepard method. The interpolation is used as an intermediate step in the 1p-kMC/CFD coupling scheme, to improve efficiency. The new interpolation method achieves better results than the state of the art while using considerably fewer 1p-kMC simulations as input data.

At present, a collaboration with experts in *in-situ* X-ray photoelectron spectroscopy (XPS) is ongoing. Motivated by the results of our 1p-kMC model, they are performing simultaneous NO and CO oxidation experiments on Pd(100). Interestingly, initial results support the existence of the oxidation inhibition effect due to NO. However, mass transfer effects seem to also play an important role in the experimental observations. Therefore, an important future step is to incorporate the CO+NO oxidation model into the multiscale modeling scheme and simulate the experiment. This should give novel insight on the effects of mass transfer, and help validate or disprove the hypothesis of the model.

Methodologically, there are also several promising future developments. In this thesis, the novel interpolation method has been shown to require fewer data points that other methods for sets of input points uniformly distributed. We believe that even greater efficiency can be obtained through a targeted selection of the data points' locations. For this, available error estimates could be used: After an initial coarse interpolant is gen-

erated from a coarse, uniformly distributed data set, new data points would be placed where error estimates are large. In this way it should be possible to only run 1p-kMC simulations which provide maximal improvement in interpolant accuracy, minimizing data redundancy. Such adaptivity scheme could be directly implemented into the kmos kMC modeling framework, enabling the generation of continuous representations of reactivity maps directly from the abstract definition of the 1p-kMC model. The availability of such an automated tool should significantly facilitate the generation of multiscale 1p-kMC/CFD models.

In addition, due to its general formulation, the interpolation scheme is potentially useful beyond kMC/CFD coupling. One possible application is towards global sensitivity analysis (GSA) of 1p-kMC models. GSA evaluates how much errors of each rate constant impact the observable prediction of the simulation. Such analysis might require the evaluation of hundreds of thousands of 1p-kMC simulations[45]. Initial tests have shown that most of these calculations could be replaced with interpolant evaluations, saving vast amounts of computational data. In addition, with minimal extensions, the model should be applicable to different interpolation problems such as, e.g. PES interpolation for MD simulations.

Acknowledgments

Many people have helped during this research project, some contributing directly to the scientific research, and others indirectly. Of the former, I would like first to thank my supervisor Prof. Karsten Reuter for giving me the opportunity to work in his group and for the guidance he provided throughout this research. I also thank Sebastian Matera, who initiated this research project and acted as a second advisor, always available and supportive. I am indebted to Max Hoffmann for his invaluable help during the early stages of my research, when he introduced me to the basics of kMC and to Python programming. I also thank him for developing the great software package kmos, which has been a crucial tool for this research. Stefan Ringe has been an excellent friend, office mate and flat mate. As our research topics were rather different, our scientific discussions were always insightful with new perspectives. Moreover, I cherish his friendliness and support during my first months in Germany, while I was still getting accustomed to life in a new country. I am also thankful to the rest of the Theoretical Chemistry group for providing such a nice and friendly work environment. I acknowledge Stefan Ringe and Simon Rittmeyer for help with proofreading this thesis and the translation of the abstract. In addition, I would also like to thank Alejandra Martinez, Fabio Busnengo and the members of the Group of Physical-Chemistry at Interfaces and Nanostructures of the Instituto de Física Rosario for welcoming me to their their research group before I started my PhD and during my more recent research visit. Without their help introducing me to first-principles modeling, I would not have started this project. The work in this thesis has been conducted with the help of many free (*libre*) software packages (kmos, ASE, numpy, scipy, matplotlib, GNU/Linux, emacs, NLopt, and others); I thank the many unsung heroes who create, maintain and contribute to free scientific software. I also acknowledge financial support from the German Research Council (DFG) and computational time provided by the Leibniz Supercomputing Centre (LRZ).

I have many friends, old and new, to thank for support not directly connected to my research, but which I value greatly. I thank the old friends who stayed in Rosario, for always welcoming me with warm hearts and hot asados. The old friends around the world for staying in touch and putting a smile on my face when we chat. The new friends for the lunch breaks, board-game nights and other outings. I am forever indebted to my parents, for nurturing my interest in math, science and technology and for providing me with the education which allowed me to pursue this PhD. To them and my sister I am always thankful for their unconditional support and encouragement, especially necessary when one is far away. I also thank my grandparents, and remember Enzo dearly, for their affection. Last but not least, I have to thank my girlfriend and better-half Mihaela with all my heart. Both the good and the difficult days of this enterprise were much better thanks to her. Her patience, trust and love have been invaluable.

Bibliography

[1] D. W. Goodman, *Chem. Rev.* **95**, 523 (1995).

[2] A. Stierle and A. M. Molenbroek, *MRS Bull.* **32**, 1001 (2007).

[3] E. Lundgren, J. Gustafson, A. Mikkelsen, J. N. Andersen, A. Stierle, H. Dosch, M. Todorova, J. Rogal, K. Reuter, and M. Scheffler, *Phys. Rev. Lett.* **92**, 046101 (2004).

[4] S. Blomberg, M. Hoffmann, J. Gustafson, N. Martin, V. Fernandes, A. Borg, Z. Liu, R. Chang, S. Matera, K. Reuter, and E. Lundgren, *Phys. Rev. Lett.* **110**, 117601 (2013).

[5] S. Matera, S. Blomberg, M. J. Hoffmann, J. Zetterberg, J. Gustafson, E. Lundgren, and K. Reuter, *ACS Catal.* **5**, 4514 (2015).

[6] K. Reuter, *Catal. Lett.* **146**, 541 (2016).

[7] J. Dou, Z. Sun, A. A. Opalade, N. Wang, W. Fu, and F. F. Tao, *Chem. Soc. Rev.* **46**, 2001 (2017).

[8] S. Matera and K. Reuter, *Catal. Lett.* **133**, 156 (2009).

[9] S. Matera and K. Reuter, *Phys. Rev. B* **82**, 085446 (2010).

[10] H. Bluhm, M. Hävecker, A. Knop-Gericke, M. Kiskinova, R. Schlögl, and M. Salmeron, *MRS Bull.* **32**, 1022 (2007).

[11] J. Frenken and B. Hendriksen, *MRS Bull.* **32**, 1015 (2007).

[12] B. Hammer and J. K. Nørskov, *Adv. Catal.* **45**, 71 (2000).

[13] J. K. Norskov, F. Abild-Pedersen, F. Studt, and T. Bligaard, *Proc. Natl. Acad. Sci. U. S. A.* **108**, 937 (2011).

[14] H. Meskine, S. Matera, M. Scheffler, K. Reuter, and H. Metiu, *Surf. Sci.* **603**, 1724 (2009).

[15] B. Temel, H. Meskine, K. Reuter, M. Scheffler, and H. Metiu, *J. Chem. Phys.* **126**, 204711 (2007).

[16] S. Matera, H. Meskine, and K. Reuter, *J. Chem. Phys.* **134**, 064713 (2011).

[17] K. Reuter, First-Principles Kinetic Monte Carlo Simulations for Heterogeneous Cataly-sis: Concepts, Status and Frontiers., in *Modelling and Simulation of Heterogeneous Catalytic Reactions: From the Molecular Process to the Technical System*, edited by O. Deutschmann, pp. 71–111, Wiley-VCH Verlag GmbH & Co. KGaA, Weinhein, 2011.

[18] M. Stamatakis and D. G. Vlachos, *ACS Catal.* **2**, 2648 (2012).

[19] M. Stamatakis, *J. Phys.: Condens. Matter* **27**, 013001 (2015).

[20] J. Rogal, K. Reuter, and M. Scheffler, *Phys. Rev. B* **77**, 155410 (2008).

[21] M. J. Hoffmann and K. Reuter, *Top. Catal.* **57**, 159 (2013).

[22] J. Jelic, K. Reuter, and R. Meyer, *ChemCatChem* **2**, 658 (2010).

[23] J. Nielsen, M. d'Avezac, J. Hetherington, and M. Stamatakis, *J. Chem. Phys.* **139**, 224706 (2013).

[24] F. Gao, Y. Wang, and D. W. Goodman, *J. Phys. Chem. C* **114**, 6874 (2010).

[25] R. van Rijn, O. Balmes, R. Felici, J. Gustafson, D. Wermeille, R. Westerström, E. Lundgren, and J. W. M. Frenken, *J. Phys. Chem. C* **114**, 6875 (2010).

[26] J. Rogal, K. Reuter, and M. Scheffler, *Phys. Rev. Lett.* **98**, 046101 (2007).

[27] J. Rogal, K. Reuter, and M. Scheffler, *Phys. Rev. B* **75**, 205433 (2007).

[28] B. L. M. Hendriksen, S. C. Bobaru, and J. W. M. Frenken, *Catal. Today* **105**, 234 (2005).

[29] Sebastian Matera, *A First-Principles Based Multiscale Approach from the Electronic to the Continuum Regime: CO Oxidation at RuO 2 (110)*, PhD thesis, Technische Unversität Berlin, Berlin, 2010.

[30] S. Matera, M. Maestri, A. Cuoci, and K. Reuter, *ACS Catal.* **4**, 4081 (2014).

[31] P. Hohenberg and W. Kohn, *Phys. Rev.* **136**, B864 (1964).

[32] W. Kohn and L. J. Sham, *Phys. Rev.* **140**, A1133 (1965).

[33] J. P. Perdew, K. Burke, and M. Ernzerhof, *Phys. Rev. Lett.* **77**, 3865 (1996).

[34] S. J. Clark, M. D. Segall, C. J. Pickard, P. J. Hasnip, M. I. J. Probert, K. Refson, and M. C. Payne, *Z. Kristallogr.* **220**, 567 (2005).

[35] C. W. Gardiner, *Handbook of Stochastic Methods for Physics, Chemistry and the Natural Sciences*, Springer Series in Synergetics, Springer, Berlin Heidelberg, Germany, 3rd edition, 2004.

[36] M. J. Hoffmann, S. Matera, and K. Reuter, *Comput. Phys. Commun.* **185**, 2138 (2014).

[37] M. J. Hoffmann, kmos, http://kmos.readthedocs.io.

[38] J. M. Lorenzi and M. Andersen, Introduction to kmos, https://github.com/jmlorenzi/intro2kmos.

[39] R. M. Ziff, E. Gulari, and Y. Barshad, *Phys. Rev. Lett.* **56**, 2553 (1986).

[40] J. J. Luque, F. Jiménez-Morales, and M. C. Lemos, *J. Chem. Phys.* **96**, 8535 (1992).

[41] K. Reuter and M. Scheffler, *Phys. Rev. B* **73**, 045433 (2006).

[42] P. Hänggi, P. Talkner, and M. Borkovec, *Rev. Mod. Phys.* **62**, 251 (1990).

[43] A. F. Voter, INTRODUCTION TO THE KINETIC MONTE CARLO METHOD, in *Radiation Effects in Solids*, edited by K. E. Sickafus, E. A. Kotomin, and B. P. Uberuaga, number 235 in NATO Science Series, pp. 1–23, Springer Netherlands, 2007, DOI: 10.1007/978-1-4020-5295-8_1.

[44] M. W. Chase, J. L. Curnutt, H. Prophet, R. A. McDonald, and A. N. Syverud, *J. Phys. Chem. Ref. Data* **4**, 1 (1975).

[45] S. Döpking and S. Matera, *Chem. Phys. Lett.* **674**, 28 (2017).

[46] S. Piccinin and M. Stamatakis, *ACS Catal.* **4**, 2143 (2014).

[47] U.S. Geological Survey, 2014 Minerals Yearbook: Platinum-Group Metals, `https://minerals.usgs.gov/minerals/pubs/commodity/platinum/myb1-2014-plati.pdf`. Accessed: 2017-08-25, 2014.

[48] U.S. Geological Survey, Mineral commodity summaries 2017: U.S. Geological Survey, `https://doi.org/10.3133/70180197`, 2017, pages 126-127.

[49] S. Matsumoto, *CATTECH* **4**, 102 (2000).

[50] G. Liu and P.-X. Gao, *Catal. Sci. Technol.* **1**, 552 (2011).

[51] S. Salasc, M. Skoglundh, and E. Fridell, *Appl. Catal. B: Environ.* **36**, 145 (2002).

[52] Y. Su, K. S. Kabin, M. P. Harold, and M. D. Amiridis, *Appl. Catal. B: Environ.* **71**, 207 (2007).

[53] A. Pandya, J. Mmbaga, R. E. Hayes, W. Hauptmann, and M. Votsmeier, *Top. Catal.* **52**, 1929 (2009).

[54] A. Boubnov, S. Dahl, E. Johnson, A. P. Molina, S. B. Simonsen, F. M. Cano, S. Helveg, L. J. Lemus-Yegres, and J.-D. Grunwaldt, *Appl. Catal. B: Environ.* **126**, 315 (2012).

[55] M. Crocoll, S. Kureti, and W. Weisweiler, *J. Catal.* **229**, 480 (2005).

[56] D. E. Doronkin, A. B. Kuriganova, I. N. Leontyev, S. Baier, H. Lichtenberg, N. V. Smirnova, and J.-D. Grunwaldt, *Catal. Lett.* **146**, 452 (2015).

[57] J. Koop and O. Deutschmann, *Appl. Catal. B: Environ.* **91**, 47 (2009).

[58] S. E. Voltz, C. R. Morgan, D. Liederman, and S. M. Jacob, *Ind. Eng. Chem. Prod. Res. Dev.* **12**, 294 (1973).

[59] S. R. Katare, J. E. Patterson, and P. M. Laing, *Ind. Eng. Chem. Res.* **46**, 2445 (2007).

[60] X. Xu, P. Chen, and D. W. Goodman, *J. Phys. Chem.* **98**, 9242 (1994).

[61] D. Rainer, S. Vesecky, M. Koranne, W. Oh, and D. Goodman, *J. Catal.* **167**, 234 (1997).

[62] E. Ozensoy and D. W. Goodman, *Phys. Chem. Chem. Phys.* **6**, 3765 (2004).

[63] A. Eichler and J. Hafner, *J. Catal.* **204**, 118 (2001).

[64] A. Eichler, *Surf. Sci.* **498**, 314 (2002).

[65] Z.-P. Liu and P. Hu, *Top. Catal.* **28**, 71 (2004).

[66] B. Hammer, *Faraday Discuss.* **110**, 323 (1998).

[67] B. Hammer, *J. Catal.* **199**, 171 (2001).

[68] D. Loffreda, F. Delbecq, D. Simon, and P. Sautet, *J. Chem. Phys.* **115**, 8101 (2001).

[69] D. Loffreda, D. Simon, and P. Sautet, *J. Catal.* **213**, 211 (2003).

[70] F. Gao, S. McClure, Y. Cai, K. Gath, Y. Wang, M. Chen, Q. Guo, and D. Goodman, *Surf. Sci.* **603**, 65 (2009).

[71] M. Chen, X. V. Wang, L. Zhang, Z. Tang, and H. Wan, *Langmuir* **26**, 18113 (2010).

[72] R. van Rijn, O. Balmes, A. Resta, D. Wermeille, R. Westerström, J. Gustafson, R. Felici, E. Lundgren, and J. Frenken, *Phys. Chem. Chem. Phys.* **13**, 13167 (2011).

[73] J. Zetterberg, S. Blomberg, J. Gustafson, Z. Sun, Z. Li, E. Lundgren, and M. Alden, *Rev. Sci. Instrum.* **83**, 053104 (2012).

[74] J. Jelic and R. J. Meyer, *Phys. Rev. B* **79**, 125410 (2009).

[75] A. Smeltz, R. Getman, W. Schneider, and F. Ribeiro, *Catal. Today* **136**, 84 (2008).

[76] R. B. Getman and W. F. Schneider, *ChemCatChem* **2**, 1450 (2010).

[77] C. Wu, D. Schmidt, C. Wolverton, and W. Schneider, *J. Catal.* **286**, 88 (2012).

[78] S. Ovesson, B. Lundqvist, W. Schneider, and A. Bogicevic, *Phys. Rev. B* **71** (2005).

[79] V. M. Janardhanan and O. Deutschmann, Computational Fluid Dynamics of Catalytic Reactors, in *Modeling and Simulation of Heterogeneous Catalytic Reactions: From the Molecular Process to the Technical System*, edited by O. Deutschmann, pp. 251–282, Wiley-VCH, 2011.

[80] D. G. Vlachos, *AIChE J.* **43**, 3031 (1997).

[81] R. Kissel-Osterrieder, F. Behrendt, and J. Warnatz, *Proc. Combust. Inst.* **27**, 2267 (1998).

[82] D. Majumder and L. J. Broadbelt, *AIChE J.* **52**, 4214 (2006).

[83] S. Raimondeau and D. G. Vlachos, *Chem. Eng. J.* **90**, 3 (2002).

[84] E. Rusli, T. O. Drews, D. L. Ma, R. C. Alkire, and R. D. Braatz, *J. Process Control* **16**, 409 (2006).

[85] A. Varshney and A. Armaou, *Chem. Eng. Sci.* **60**, 6780 (2005).

A Publications

A.1 Paper 1

Synergistic Inhibition of Oxide Formation in Oxidation Catalysis: A First-Principles Kinetic Monte Carlo Study of NO + CO Oxidation at Pd(100).
Juan M. Lorenzi, Sebastian Matera and Karsten Reuter
ACS Catalysis, Vol. 6, pp 5191 - 5197.

ACS Catalysis

Letter

pubs.acs.org/acscatalysis

Synergistic Inhibition of Oxide Formation in Oxidation Catalysis: A First-Principles Kinetic Monte Carlo Study of NO + CO Oxidation at Pd(100)

Juan M. Lorenzi,[†] Sebastian Matera,[‡] and Karsten Reuter*[,†]

[†]Chair for Theoretical Chemistry and Catalysis Research Center, Technische Universität München, Lichtenbergstr. 4, 85747 Garching, Germany

[‡]Fachbereich f. Mathematik u. Informatik, Freie Universität Berlin, Otto-von-Simson-Str. 19, D-14195 Berlin, Germany

Supporting Information

ABSTRACT: Oxide formation under oxygen-rich reaction conditions has independently been reported for both CO oxidation and NO oxidation with Pd single-crystal model catalysts. We present a first-principles kinetic Monte Carlo study addressing the simultaneous occurrence of both reactions at Pd(100) exposed to CO- and NO-containing feeds. Even in most oxygen-rich feeds, very small amounts of NO are found to reduce the surface oxygen coverage well below the level required to induce oxide formation. Even though NO and CO compete for the same surface sites and surface oxygen, the ongoing NO oxidation reactions furthermore lead to a partially strong enhancement of the CO oxidation activity. This highlights synergistic effects of multicomponent gas feeds on both surface composition and catalytic activity that cannot be captured, nor extrapolated from prevalent studies focusing on individual reactions.

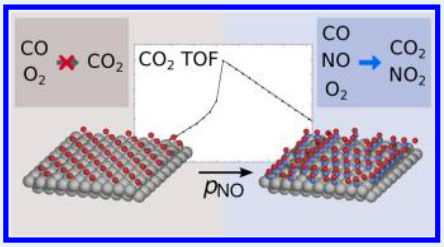

KEYWORDS: *first-principles kinetic Monte Carlo, heterogeneous catalysis, CO oxidation, NO oxidation, oxide formation, NOx reduction, automotive catalysis*

1. INTRODUCTION

The last two decades have seen an extensive (partially heated) discussion, with regard to the active state of late-transition-metal catalysts commonly employed in oxidation catalysis.[1−4] In the oxygen-rich environment, the formation of oxides, thin oxide films, or other heavily oxygen-loaded surface structures would generally be expected for Pt-group metals on thermodynamic grounds. Under operating conditions, this is opposed by the continuing reduction due to the ongoing surface reactions, as well as kinetic limitations to dissociative oxygen adsorption or further oxidation. For the purpose of identifying which effects dominate for the working catalyst, strong efforts have been devoted to identify the surface structure and composition of low-index model catalysts under reaction conditions that come as close as possible to those of technological oxidation catalysis.[5,6] Corresponding near-ambient *in situ* measurements or first-principles microkinetic modeling studies have partially confirmed the formation of oxygen-rich surface structures, partially rejected such formation, or even reported an oscillatory formation and decomposition.[7−13]

While the case is thus not generally settled, an important feature common to previous atomic-scale investigations of single-crystal model catalysts is the consideration of a simplified gas composition, i.e., only the presence of one reducing agent in the feed has been systematically addressed. In the predominantly studied CO oxidation, for instance, this is CO; in NO oxidation, this is NO. This makes the problem more tractable, but neglects possibly important inhibitive or synergistic effects that have frequently been discussed for the multicomponent feeds of real applications.[14−22] Inspired by the automotive exhaust gas composition of lean-burn or diesel engines, we assess this possibility for a gas phase containing both CO and NO and by setting up a first-principles kinetic Monte Carlo model that correspondingly accounts for simultaneous NO and CO oxidation reactions. As the substrate, we specifically select the Pd(100) surface, for which oxide formation has been reported experimentally for both CO oxidation[12] and NO oxidation.[23] The stability, in particular of a monolayer thin PdO(101) surface oxide layer,[24,25] has also been confirmed by constrained *ab initio* thermodynamics and first-principles kinetic Monte Carlo (1p-kMC) studies considering either a CO + O_2[9,11] or a NO + O_2 atmosphere.[26,27] In contrast, a recent 1p-kMC study for CO oxidation at Pd(100) has emphasized the suppression of dissociative O_2 adsorption by higher surface coverages, which kinetically limits the O coverage to values below the threshold inducing oxide formation.[28]

We find that this effect is dramatically increased by the simultaneous presence of NO in the feed. Already smallest amounts of NO, of the order or smaller than, e.g., that typically present under NO_x storage reduction (NSR) conditions,[21,29,30]

Received: May 13, 2016
Revised: July 4, 2016

DOI: 10.1021/acscatal.6b01344
ACS Catal. 2016, 6, 5191−5197

are sufficient to reduce the surface oxygen coverage below the values required for oxide formation for a wide range of near-ambient O_2 and CO pressures. Interestingly, this goes hand in hand with a significant increase in the CO oxidation activity for oxygen-rich conditions. Our systematic analysis tracks both effects down to the reduction of kinetic adsorption limitations by additional reaction and diffusion channels offered in the enhanced NO + CO oxidation reaction network. Corresponding synergistic effects in multicomponent gas phases can be neither captured nor extrapolated from studies selectively addressing the catalytic function in feeds containing only subsets of the reactive species.

2. THEORY

We use 1p-kMC simulations[31,32] to numerically evaluate the microkinetics of the NO + CO oxidation reaction network. Different from mean-field rate-equation based microkinetic simulations, 1p-kMC thereby fully treats the correlations, fluctuations, and explicit spatial distributions of the reaction intermediates at the catalyst surface.[33] Targeting steady-state reaction conditions with defined temperature and reactant partial pressures, the 1p-kMC simulations yield the detailed occurrence of any elementary process or local surface configuration within the entire reaction network. Appropriately averaged over a sufficiently large ensemble of surface sites, this leads to the average coverages of all reaction intermediates and to the catalytic activity (measured as turnover frequency (TOF) in product molecules per area and time). As with any microkinetic model, the necessary input to the simulations includes a list of all elementary processes in the reaction network, together with their respective rate constants. The latter are determined using density functional theory (DFT) and transition-state theory (TST).[32,34] To be able to account for the geometric arrangement of the individual surface sites active in the reaction network, 1p-kMC additionally requires this information in the form of a lattice model.

For the CO oxidation part of the reaction network, we rely on the 1p-kMC model established previously by Hoffmann et al.[28,35] Therefore, the following subsections provide first a concise summary of this model and then an account of the computational setup used to obtain the first-principles rate constants and perform the 1p-kMC simulations. This very framework is subsequently employed to extend the CO oxidation model toward (simultaneous) NO oxidation, the details of which are described in subsection 2.3.

2.1. Literature 1p-kMC Model of CO Oxidation at Pd(100). The 1p-kMC model of CO oxidation at Pd(100) by Hoffmann et al.[28,35] considers the high-symmetry hollow and bridge sites as adsorption sites for O and CO, respectively. The list of elementary processes correspondingly contains all nonconcerted adsorption, desorption, diffusion, and Langmuir−Hinshelwood reaction processes involving these sites. Oxygen adsorbs dissociatively and CO unimolecularly. Both processes are nonactivated. The corresponding desorption processes are time reversals of these adsorption processes, with rate constants fulfilling detailed balance. Since CO_2 binds only very weakly to Pd(100), CO oxidation is modeled as associative desorption, i.e., with the formed CO_2 desorbing instantaneously and irreversibly at the temperatures of interest in this study.

Systematic DFT calculations identified strong short-range repulsive interactions between the adsorbed reaction intermediates.[36−38] In the 1p-kMC model, these are accounted for through site-blocking rules that exclude processes leading to O−O pairs at nearest-neighbor (NN) hollow−hollow distances, to CO−CO pairs closer than or at next-NN bridge−bridge distance, and O−CO pairs at NN hollow-bridge distance.[28] Diffusion processes are thus hops between NN sites obeying these site-blocking rules, whereas, for dissociative O_2 adsorption, these rules imply the necessity of a pattern of eight empty hollow sites, such that the two O atoms can adsorb in next-NN sites and have no NNs in any of the surrounding hollow sites (the so-called 8-site rule[28,38]).

2.2. Computational Setup. For the calculation of the first-principles rate constants, we employ the approach described by Reuter and Scheffler.[34] This approach relies on kinetic gas theory to determine the rate constants for adsorption processes, whereas, for bound-to-bound transitions such as surface diffusion or Langmuir−Hinshelwood reactions, harmonic TST is applied. Desorption events are modeled as reverse adsorption processes with rate constants satisfying detailed balance. Gas-phase chemical potentials are interpolated to tabulated values,[28,39,40] which assures correct equilibrium conversion of the gas-phase species. The necessary first-principles input is then essentially reduced to binding energies and reaction barriers. We compute these energetic parameters with DFT and using the plane-wave code CASTEP, together with standard library ultrasoft pseudo-potentials.[41] Electronic exchange and correlation is treated at the level of the generalized gradient approximation functional by Perdew, Burke, and Ernzerhof (PBE)[42] that was also employed in the 1p-kMC model of CO oxidation at Pd(100).[28,35]

The calculations are performed within supercell geometries, using four layer slabs (with the topmost two layers fully relaxed), 3 × 3 surface unit cells, and a 10 Å vacuum. The energetics of the gas-phase molecules is calculated using a 12 Å × 12 Å × 12 Å box and Γ-point sampling. At the employed cutoff of 400 eV and a *k*-point density of 0.4 $Å^{-1}$ for the supercell calculations, the targeted binding energies and reaction barriers are converged to within 50 meV. Transition-state searches are performed using the climbing-image Nudged Elastic Band (NEB)[43] method. We made sure that all forces at the saddle points were lower than 0.05 eV/Å and also checked the nature of the transition state by calculating the vibrational frequencies using the finite displacement method (keeping the substrate frozen). Both NEB calculations and vibrational analyses are performed within the Atomistic Simulation Environment (ASE).[44]

This computational framework yields energetic parameters that are fully compatible with the literature values of the CO oxidation 1p-kMC model, with small deviations within 70 meV, because of the use of a smaller surface unit cell in the preceding work. A notable exception is presented by the CO oxidation reaction barrier, which was previously estimated by reaction coordinate scans as ∼0.9 eV[28] and is now computed with the NEB method as 0.68 eV (*vide infra*). We confirmed that none of the conclusions presented in ref 28 are affected by this change in the barrier value.

The 1p-kMC model was implemented and run using the kmos computer package.[45] The simulations are performed in simulation cells containing 20 × 20 Pd(100) unit cells (comprising 1200 bridge and hollow sites) and periodic boundary conditions. Test simulations in larger cells containing up to 60 × 60 unit cells showed no evidence of finite size effects. Analogous to the procedure employed by Hoffmann et al.,[28,35] the numerical efficiency of the simulations was increased by raising the barriers of otherwise dominant diffusion

DOI: 10.1021/acscatal.6b01344
ACS Catal. 2016, 6, 5191−5197

processes by 0.5 eV. Validation runs with smaller diffusion barriers showed no significant changes, demonstrating that, even with the raised barriers, diffusion is still fast enough to achieve an equilibration of the adlayer ordering between the other (rare) elementary processes.[32] With these settings, running the simulations over 10^{10} kMC steps was found to be enough to reach steady state and subsequently achieve sufficient sampling for converged average coverages and TOFs.

2.3. Extended 1p-kMC Model of CO + NO Oxidation at Pd(100). The properties of Pd(100) toward NO adsorption and NO reduction to N_2 have been extensively studied both theoretically[46−49] and experimentally.[50−54] Consistent with these works, our DFT calculations at varying coverages indicate a preferential NO adsorption at the high-symmetry bridge sites offered by the Pd(100) surface. These previous studies furthermore suggest that Pd(100) terraces are not very active toward NO dissociation. In particular, both Loffreda et al.[49] and Hammer[48] computed rather high barriers in excess of 1.6 eV for this process. Focusing on oxidizing conditions, we correspondingly neglect NO dissociation events, as well as further reaction channels requiring NO dissociation in the 1p-kMC model and focus on the unimolecular adsorption (and desorption) of NO at bridge sites. This choice is supported *a posteriori* by test simulations that augment our 1p-kMC model with NO dissociation and N_2 formation processes with barriers from ref 48 and that indeed resulted in almost no NO dissociation events occurring in the entire relevant range of gas-phase conditions.

In contrast, NO oxidation yields NO_2 as another reaction intermediate to consider. Different from CO_2, we find NO_2 to bind with moderate strength to Pd(100), requiring its explicit incorporation into the 1p-kMC model. A systematic calculation of NO_2 binding to all Pd(100) high-symmetry sites in upright and tilted configurations (see the Supporting Information (SI)) identifies the tilted on-top configuration shown in Figure 1 as most stable one, with a binding energy of −1.55 eV.

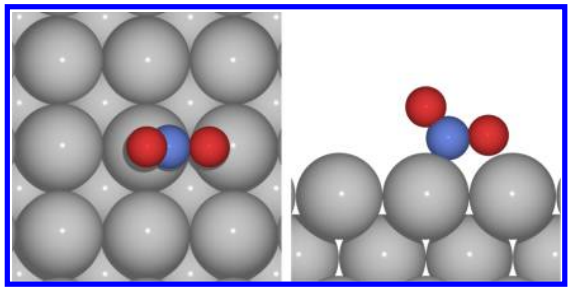

Figure 1. Top view (left) and side view (right) of the optimized adsorption geometry of NO_2 at Pd(100). O, N, and Pd atoms are depicted as red, blue, and gray spheres, respectively.

Similar to CO and O, we suspect sizable lateral interactions also with and between the additional reaction intermediates (NO and NO_2). We computed a DFT database of 97 (co)adsorption configurations in 2 × 2 and 3 × 2 surface unit cells to extract these lateral interactions through pairwise cluster expansions.[36,38] Aiming at higher coverage configurations, we thereby neglect the tilt of the NO_2 adsorption geometry and assume a C_{4v} symmetry in the interactions. As detailed in the SI and irrespective of the particular interaction figures considered in the cluster expansions, this yields strongly repulsive interactions at short range, as previously found for CO oxidation. Consistent with the procedure employed in the original CO oxidation 1p-kMC model,[28,35] we account for these strong interactions through site-blocking rules, suppressing any processes that would lead to top−top, bridge−bridge, top−hollow, top−bridge, and bridge−hollow species at NN distance. In the case of bridge−bridge interactions (NO−NO, NO−CO), this site blocking also extends to a second NN distance across a top site. Similar to the previous findings for CO and O,[28,35] the cluster expansions, in fact, also predict finite-size repulsive interactions at even larger distances. We correspondingly expect the employed shortest-range site-blocking rules to yield a lower bound to the effect of the true interactions. Preliminary 1p-kMC simulations with further ranging site-blocking blocking rules indeed show all the effects discussed below.

Under consideration of the site-blocking rules, all adsorption, desorption, diffusion and reaction processes of the extended CO + NO oxidation model are then essentially defined by the energetic quantities compiled in Table 1. The adsorption processes additionally require a sticking coefficient. Systematic potential energy scans vertically lifting NO and NO_2 from their adsorption site provide no evidence for an additional activation barrier to adsorption. We correspondingly model NO and NO_2 adsorption as nonactivated and use sticking coefficients of 0.5 and 1, respectively, which arises in the hole model underlying the Reuter/Scheffler approach[34] from a straightforward equipartitioning of all impinging molecules over the available active sites per surface unit cell. We note that NO oxidation is a reversible process, which is endothermic in the forward direction (cf. Table 1). Notwithstanding, NO_2 dissociation requires an adjacent empty bridge−hollow second NN site pair, which will favor NO oxidation at higher coverages.[27] For the reaction conditions considered in this study, we treat the desorption of the formed NO_2 as being irreversible, i.e., there is no readsorption of NO_2 from the gas phase. At the low NO_2 TOFs, the underlying assumption thereby is that the small amount of formed NO_2 is quickly swept away with the stream in the reactor geometries typically employed in *in situ* studies on single-crystal model catalysts.[55−57] For channel-type reactors as used for supported real catalysts back-reactions might instead become quite important.[30]

Table 1. Summary of All DFT Binding Energies, As Well As Diffusion and Reaction Barriers Used in the Extended 1p-kMC NO + CO Oxidation Model

parameter	value
Binding Energies	
$E_O^{b,hollow}$	−1.17 eV
$E_{CO}^{b,br}$	−2.00 eV
$E_{NO}^{b,br}$	−2.27 eV
$E_{NO_2}^{b,top}$	−1.55 eV
Diffusion Barriers	
ΔE_O^{diff}	0.24 eV
ΔE_{CO}^{diff}	0.12 eV
ΔE_{NO}^{diff}	0.14 eV
$\Delta E_{NO_2}^{diff}$	0.15 eV
Surface Reactions	
CO + O → CO_2	
ΔE^{forw}	0.68 eV
NO + O ↔ NO_2	
ΔE^{forw}	1.06 eV
ΔE^{back}	0.32 eV

DOI: 10.1021/acscatal.6b01344
ACS Catal. 2016, 6, 5191−5197

3. RESULTS

3.1. Synergism in the CO + NO Oxidation Activity. We start analyzing the effect of additional NO species present in the feed gas by comparing the CO oxidation activity in the absence of gaseous NO with that resulting in the presence of a small amount of NO, corresponding to $p_{NO} = 10^{-4}$ bar. Figure 2 shows the corresponding results as a function of oxygen and

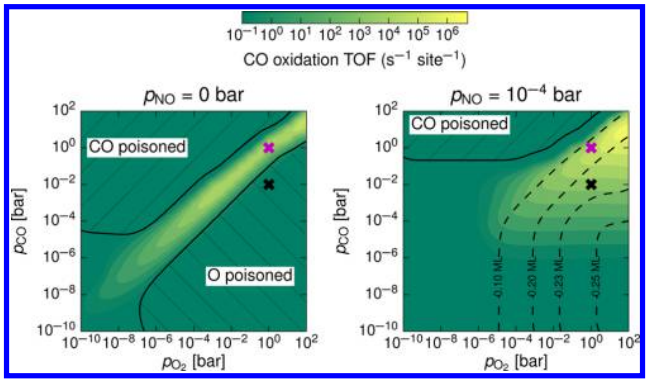

Figure 2. Steady-state CO oxidation turnover frequency (TOF), as a function of oxygen and CO partial pressures at T = 600 K, in the absence of additional NO in the feed (left panel) and for a finite amount of NO, corresponding to $p_{NO} = 10^{-4}$ bar (right panel). Hatched lines represent the regions in which the catalyst is poisoned by either CO or oxygen. As the O-poisoned region is absent in the finite p_{NO} case, contour lines for the O coverage are included. The crosses in the diagrams indicate the (p_{O_2}, p_{CO}) conditions used in Figure 3.

CO partial pressures and for a temperature of 600 K. In the absence of NO, we obtain the expected confinement of high catalytic activity to a narrow range of gas-phase conditions around a stoichiometric CO/O_2 partial pressure ratio. Under corresponding pressure ratios (and sufficient absolute pressures), both reaction intermediates, CO and O, are stabilized at the surface in appreciable amounts, which then enables efficient execution of the Langmuir−Hinshelwood-type oxidation reaction. Outside this pressure corridor, the surface gets poisoned by one of the intermediates as also indicated in Figure 2. Under the site-blocking rules employed in the present 1p-kMC model such (O or CO) poisoning corresponds to reaching a maximum coverage of 0.5 monolayer (ML), which then prevents any coadsorption of the respective other species. In the case of O-poisoning, reaching such a critical coverage would, in reality, induce the formation of a surface oxide, which, for Pd(100), is known to start at an O coverage of ≥0.5 ML.[24] For any lower O coverage, we should instead be well inside the applicability regime of the present microkinetic model focusing exclusively on surface reactions at metal Pd(100).[9,11,27,28,35]

Intriguingly, the addition of only a small amount of NO to the feed gas heavily reduces this steady-state O coverage under oxygen-rich conditions. Already for the chosen $p_{NO} = 10^{-4}$ atm, which is at or below the pressures representative for NSR conditions,[21,29,30] no O-poisoning is reached anymore in the entire pressure range displayed in Figure 2. Instead, the oxygen coverage reaches at maximum of ∼0.25 ML, predicting that oxide formation would be clearly inhibited, even under the most oxygen-rich reaction conditions shown. In corresponding environments, the additional NO also leads to a significant increase in the CO oxidation activity, i.e., the active region with appreciable TOFs is much wider in the right panel of Figure 2, while the maximum TOF values reached are barely changed. This positive effect on the CO oxidation properties is quite remarkable considering that CO and NO compete for the same surface sites and for the same adsorbed oxygen species.

3.2. Coverage and Lateral Interactions. In order to analyze these intriguing findings in more detail, we now concentrate on two specific (p_{O_2}, p_{CO}) conditions, which are marked with crosses in Figure 2. Both correspond to a fixed condition of p_{O_2} = 1 bar at T = 600 K and contrast a situation that, in the absence of NO, is in the high-activity stoichiometric-pressure regime (p_{CO} = 1 bar, magenta cross) and a situation that, in the absence of NO, is in the O-poisoned regime (p_{CO} = 0.01 bar, black cross). For the sake of simplicity, we will henceforth refer to these two reaction conditions shortly as "high activity" and "poisoned". The top panels of Figure 3 show how the CO and NO oxidation activities change

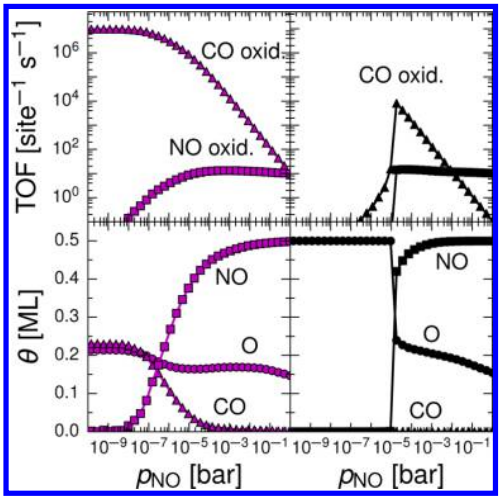

Figure 3. CO and NO oxidation TOFs (top panels) and surface coverages θ (bottom panels), as a function of NO partial pressure and T = 600 K. Compared are two specific reaction conditions marked with crosses in Figure 2: p_{O_2} = 1 bar, p_{CO} = 1 bar (magenta, left panels) and p_{O_2} = 1 bar, p_{CO} = 0.01 bar (black, right panels), representing high-activity and O-poisoned conditions in the absence of NO, respectively.

for these two cases when the NO pressure is continuously increased. For the "high activity" case, the TOFs evolve smoothly and in a form that is intuitive, in view of the competition of the NO and CO oxidation reactions for the same surface sites and adsorbed oxygen. With increasing p_{NO}, the initially high CO oxidation TOF gradually decreases, at the expense of a continuously rising NO oxidation TOF. In contrast, much more abrupt variations arise in the "poisoned" case. Here, appreciable CO oxidation activity only sets in above a critical p_{NO} (∼10^{-5} atm), then decays again after this initial steep increase. Interestingly, the NO oxidation activity sets in simultaneously with the CO oxidation activity, but then plateaus for higher p_{NO} at exactly the same value as in the "high activity" case.

The key to understanding the less intuitive activity variation of the "poisoned" case comes from an analysis of the surface coverages also compiled in Figure 3 for both cases. For the "high activity" case, we find, at the lowest NO pressures, an O coverage of ∼0.2 ML and a CO coverage at a similar value. This is roughly what thermodynamics wants: If we switch off all oxidation reactions in the 1p-kMC simulations and thereby

DOI: 10.1021/acscatal.6b01344
ACS Catal. 2016, 6, 5191−5197

simulate the adsorption−desorption equilibrium situation, we obtain O and CO coverages of ∼0.3 ML and ∼0.35 ML, respectively, for these pressure conditions. Under the highly repulsive lateral interactions, this is close to the maximum coverage that can be achieved at the surface. The ongoing surface reactions thus remove surface species faster than can be replenished from the gas phase, resulting in average coverages that are below this ideal thermodynamic limit. At increasing p_{NO}, NO starts to compete with CO for the bridge sites. Since NO is subject to the same repulsive lateral interactions with O, this does not affect the O surface population substantially. Its coverage remains almost constant, as is apparent from Figure 3. NO replaces CO at the surface to ultimately reach the maximum possible coverage of 0.5 ML at the highest NO pressures shown. This gradual replacement then effectuates the intuitive smooth TOF variations previously discussed.

The situation is quite different in the "poisoned" case. At the lowest p_{NO}, the ideal thermodynamic coverages resulting from the mere adsorption−desorption equilibrium would be similar to those for the "high activity" case (∼0.3 ML O and ∼0.35 ML CO). In contrast, we see, in Figure 3, the maximum coverage of 0.5 ML O possible in the present 1p-kMC model that concomitantly completely suppresses CO at the surface. This difference from the "high activity" case comes from the changed p_{O_2}/p_{CO} partial pressure ratio. With a ratio of 100:1, CO is now an absolute minority species, which makes replenishment of surface CO through adsorption a much slower process. In consequence, the ongoing surface reactions diminish the surface CO population so much that enough space is created to accommodate more surface oxygen. Under the highly repulsive O−O interactions, this corresponds to a $c(2 \times 2)$ motif. The highly repulsive O−CO interactions then prevent any adsorption of CO into such an oxygen-enriched area. A critical NO pressure is necessary to break this deadlock. Above $p_{NO} \approx 10^{-5}$ atm, NO can be stabilized at the surface, which goes hand in hand with the abrupt reduction of the surface oxygen coverage back to the 0.2 ML case. This frees surface sites for CO adsorption and leads to a strong increase in CO oxidation activity. After this transition, the situation is then equivalent to the "high activity" case with a gradual replacement of CO by NO. Since the NO coverage eventually reaches the same maximum value, the NO oxidation TOF also plateaus at the same value.

3.3. Beyond Coadsorption Effects. From the analysis to this point, it would seem as if the observed positive effect of NO on the "poisoned" case is a simple coadsorption effect, in which the additional presence of NO at the surface helps to suppress the buildup of a poisoning O coverage. Yet, further analysis demonstrates that the cooperativity is more intricate. Selectively switching off the NO oxidation reactions in the 1p-kMC model simulates precisely the effect of a mere coadsorption of (nonreactive) NO. Indeed, such simulations yield a coverage pattern that resembles that discussed for the fully reactive simulations to a large extent, except for a shift in the p_{NO} axis. The "high activity" case exhibits the smooth gradual replacement of CO by NO at bridge sites at ∼0.2 ML O coverage that is essentially independent of p_{NO}. The "poisoned" case shows the abrupt reduction of the O coverage once a threshold NO pressure of $\sim 10^{-4}$ bar is exceeded. Surprisingly, however, these equivalent coverages yield significantly changed CO oxidation TOFs, as summarized in Figure 4. While in the "high activity" case the TOF is

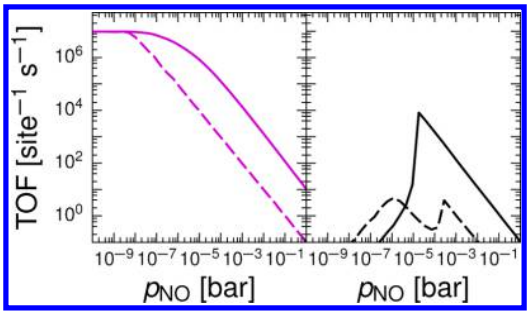

Figure 4. CO oxidation TOFs for the "high activity" (magenta, left panel) and "poisoned" (black, right panel) cases. Compared are the full simulation results as given in Figure 3 (solid lines) to results when the NO oxidation reactions are switched off in the 1p-kMC simulations (dashed lines). Without these reactions, the positive cooperativity is gone and the CO oxidation TOF in the "poisoned" case (black, right panel) remains low at all NO pressures.

systematically lowered by ∼2 orders of magnitude for all but the lowest NO partial pressures, the more striking finding is that, for the "poisoned" case, the CO oxidation TOF remains low for all NO pressures. The "poisoned" case thus remains essentially poisoned, irrespective of an additional presence of NO in the feed. Although we do observe a small enhancing effect due to NO, it is of a much smaller magnitude. In particular, for the intermediate NO pressures just above the threshold at $p_{NO} \approx 10^{-5}$ bar, this implies a quenching of the CO oxidation activity of more than 4 orders of magnitude (cf. Figure 4).

By further modifying the process list considered in the 1p-kMC simulations, we can trace this finding back to the removal of kinetic adsorption limitations by additional reaction and diffusion channels enabled through the NO oxidation part of the reaction network. Both channels bring locally O-poisoned configurations at the surface out of the deadlock situation, by either creating additional NO or CO adsorption possibilities through NO_2 desorption or by diffusional intermixing. Both cases offer increased possibilities to react off adsorbed O and thereby induce the transition from the O-poisoned coverage to a situation with coexisting NO + O already at lower p_{NO}. At these lower p_{NO}, a resulting intermediate NO coverage still leaves sites for CO coadsorption, which, in turn, enables efficient Langmuir−Hinshelwood CO oxidation reactions and the concomitant enhancement of the CO oxidation TOF.

As stated, the effect of the additional reaction channel is thereby simply the creation of free adsorption sites due to the desorption of formed NO_2. We can selectively assess this effect by allowing for the formation and decomposition of surface NO_2 in the 1p-kMC simulations, but disabling the possibility of NO_2 desorption (cf. the SI). More intriguing, however, is the diffusional channel. As illustrated in Figure 5, the formation and subsequent decomposition of a NO_2 reaction intermediate at the surface creates a new O diffusion possibility out of local configurations, where regular hopping diffusion would be suppressed by the repulsive lateral interactions. Because of the endothermicity of the NO oxidation reaction step, the decomposition of a once-formed NO_2 is a likely process, if a neighboring free site and the blocking rules allow for it. We can again selectively assess the effect of this new diffusion channel by restricting NO_2 decomposition only back into the original NO + O configuration out of which the NO_2 was formed in the 1p-kMC simulations. A corresponding suppression of the

DOI: 10.1021/acscatal.6b01344
ACS Catal. 2016, 6, 5191−5197

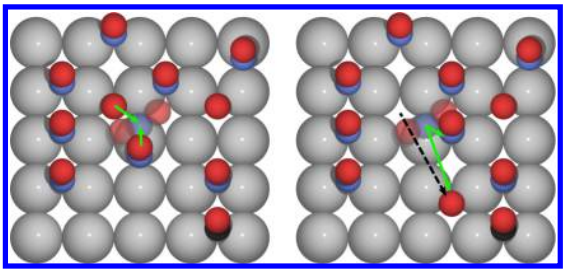

Figure 5. Top view illustrating the additional O diffusion mechanism enabled through the formation (left panel) and subsequent decomposition (right panel) of a NO_2 reaction intermediate. O, N, C, and Pd atoms are depicted as red, blue, black, and gray spheres, respectively.

diffusion mechanism results in TOFs that are only minimally modified from the results shown in Figure 4 when no NO oxidation reactions are allowed to occur at all. Allowing for the diffusion mechanism (i.e., an unrestricted formation and decomposition of NO_2 species) increases the maximum CO oxidation TOF reached already by more than 1 order of magnitude, compared to these no-NO-oxidation results. The remaining difference to the TOFs obtained with the true model with all processes enabled (cf. Figure 4) are then due to the additional reaction channel. While regular coadsorption effects as described in the last section can, to some extent, be extrapolated from separate studies of the individual oxidation reactions, this is neither the case for the additional reaction nor for the diffusion channel. Cooperative effects on the catalytic activity due to such mechanisms are correspondingly missed in traditional studies focusing on idealized feeds containing only one reducing agent.

4. CONCLUSIONS

Fundamental studies that concentrate on establishing microscopic insight into surface catalysis at single-crystal model catalysts largely focus on purified gas feeds containing a minimum number of components. In oxidation catalysis, prominent examples are the reactions of CO oxidation, NO oxidation, or water oxidation, each of which is selectively studied in gas phases containing oxygen plus one reductant (CO, NO, or H_2O, respectively). While this approach reduces the complexity of the problem, it dismisses possible cooperative effects that may arise in multicomponent gas feeds as is common in real applications. We investigated such effects using a 1p-kMC model that describes the simultaneous CO and NO oxidation at a Pd(100) model catalyst. Our results indeed show strong synergistic effects on both the surface composition and the catalytic activity that could not have been extrapolated from the separate study of both oxidation reactions. Very small amounts of NO in the feed gas are sufficient to reduce the surface oxygen coverage well below the level that would otherwise have induced oxide formation in corresponding oxygen-rich environments in CO oxidation catalysis. Simultaneously, this small amount of NO strongly enhances the CO oxidation activity in this oxygen-rich regime, despite competing for the same surface sites and adsorbed oxygen. One key factor behind such nonadditive effects is that already smallest amounts of an additional reaction intermediate (here, NO) may induce surface phase transitions in the adlayer formed by the other intermediates (here, O and CO). This effect is amplified in the presence of strongly repulsive lateral interactions, as is common at late transition-metal surfaces. This complexity cannot be easily captured in prevalent mean-field microkinetic modeling and may thus have been overlooked so far. It can only be grasped with most advanced site-resolved microkinetic analyses, which reveal intricacies in heterogeneous catalysis that continue to surprise us.

■ ASSOCIATED CONTENT

Supporting Information

This material is available free of charge via the Internet at http://pubs.acs.org/. The Supporting Information is available free of charge on the ACS Publications website at DOI: 10.1021/acscatal.6b01344.

NO_2 adsorption configuration search; lateral interaction calculations; analysis of the influence of the blocking-rules scheme; reactivity predicted by the 1p-kMC model with different altered process lists; discussion of the viability of using a mean-field approach (PDF)

■ AUTHOR INFORMATION

Corresponding Author

*E-mail: karsten.reuter@ch.tum.de.

Notes

The authors declare no competing financial interest.

■ ACKNOWLEDGMENTS

We gratefully acknowledge support from the German Research Council (DFG) and the TUM Faculty Graduate Center Chemistry, as well as generous computing time at the Leibniz Rechenzentrum (LRZ) of the Bavarian Academy of Sciences. S.M.'s research is carried out in the framework of MATHEON supported by the Einstein Foundation Berlin. J.M.L. acknowledges enlightening discussions with Max J. Hoffmann.

■ REFERENCES

(1) Reuter, K. In *Nanocatalysis*, 1st Edition; Heiz, U., Landman, U., Eds.; Springer: Berlin, 2006; p 343.
(2) Lundgren, E.; Mikkelsen, A.; Andersen, J.; Kresse, G.; Schmid, M.; Varga, P. *J. Phys.: Condens. Matter* **2006**, *18*, R481−R499.
(3) Over, H. *Chem. Rev.* **2012**, *112*, 3356−3426.
(4) Weaver, J. F. *Chem. Rev.* **2013**, *113*, 4164−4215.
(5) *In-situ Materials Characterization: Across Spatial and Temporal Scales*; Ziegler, A., Graafsma, H., Zhang, X. F., Frenken, J. W. M., Eds.; Springer Series in Materials Science, Vol. *193*; Springer: Berlin, 2014.
(6) Reuter, K. *Catal. Lett.* **2016**, *146*, 541−563.
(7) Gao, F.; Wang, Y.; Goodman, D. W. *J. Phys. Chem. C* **2010**, *114*, 6874−6874.
(8) van Rijn, R.; Balmes, O.; Felici, R.; Gustafson, J.; Wermeille, D.; Westerström, R.; Lundgren, E.; Frenken, J. W. M. *J. Phys. Chem. C* **2010**, *114*, 6875−6876.
(9) Rogal, J.; Reuter, K.; Scheffler, M. *Phys. Rev. Lett.* **2007**, *98*, 046101.
(10) Rogal, J.; Reuter, K.; Scheffler, M. *Phys. Rev. B: Condens. Matter Mater. Phys.* **2007**, *75*, 205433.
(11) Rogal, J.; Reuter, K.; Scheffler, M. *Phys. Rev. B: Condens. Matter Mater. Phys.* **2008**, *77*, 155410.
(12) Hendriksen, B. L. M.; Bobaru, S. C.; Frenken, J. W. M. *Catal. Today* **2005**, *105*, 234−243.
(13) Matera, S.; Blomberg, S.; Hoffmann, M. J.; Zetterberg, J.; Gustafson, J.; Lundgren, E.; Reuter, K. *ACS Catal.* **2015**, *5*, 4514−4518.
(14) Voltz, S. E.; Morgan, C. R.; Liederman, D.; Jacob, S. M. *Ind. Eng. Chem. Prod. Res. Dev.* **1973**, *12*, 294−301.

DOI: 10.1021/acscatal.6b01344
ACS Catal. 2016, 6, 5191−5197

(15) Crocoll, M.; Kureti, S.; Weisweiler, W. *J. Catal.* **2005**, *229*, 480−489.
(16) Irfan, M. F.; Goo, J. H.; Kim, S. D.; Hong, S. C. *Chemosphere* **2007**, *66*, 54−59.
(17) Katare, S. R.; Patterson, J. E.; Laing, P. M. *Ind. Eng. Chem. Res.* **2007**, *46*, 2445−2454.
(18) Koop, J.; Deutschmann, O. *Appl. Catal., B* **2009**, *91*, 47−58.
(19) Pandya, A.; Mmbaga, J.; Hayes, R. E.; Hauptmann, W.; Votsmeier, M. *Top. Catal.* **2009**, *52*, 1929−1933.
(20) Yamashita, H.; Yane, H.; Yamamoto, K. *J. Environ. Eng.* **2011**, *6*, 437−451.
(21) Boubnov, A.; Dahl, S.; Johnson, E.; Molina, A. P.; Simonsen, S. B.; Cano, F. M.; Helveg, S.; Lemus-Yegres, L. J.; Grunwaldt, J.-D. *Appl. Catal., B* **2012**, *126*, 315−325.
(22) Doronkin, D. E.; Kuriganova, A. B.; Leontyev, I. N.; Baier, S.; Lichtenberg, H.; Smirnova, N. V.; Grunwaldt, J.-D. *Catal. Lett.* **2016**, *146*, 452−463.
(23) Weiss, B. M.; Iglesia, E. *J. Catal.* **2010**, *272*, 74−81.
(24) Todorova, M.; Lundgren, E.; Blum, V.; Mikkelsen, A.; Gray, S.; Gustafson, J.; Borg, M.; Rogal, J.; Reuter, K.; Andersen, J. N.; Scheffler, M. *Surf. Sci.* **2003**, *541*, 101−112.
(25) Lundgren, E.; Gustafson, J.; Mikkelsen, A.; Andersen, J.; Stierle, A.; Dosch, H.; Todorova, M.; Rogal, J.; Reuter, K.; Scheffler, M. *Phys. Rev. Lett.* **2004**, *92*, 046101.
(26) Jelic, J.; Meyer, R. J. *Phys. Rev. B: Condens. Matter Mater. Phys.* **2009**, *79*, 125410.
(27) Jelic, J.; Reuter, K.; Meyer, R. *ChemCatChem* **2010**, *2*, 658−660.
(28) Hoffmann, M. J.; Reuter, K. *Top. Catal.* **2014**, *57*, 159−170.
(29) Matsumoto, S. *CATTECH* **2000**, *4*, 102−109.
(30) Koop, J.; Deutschmann, O. Modeling and simulation of NOx abatement with storage/reduction catalysts for lean burn and diesel engines. *SAE Tech. Pap. Ser.* **2007**, Paper No. 2007-01-1142 (DOI: 10.4271/2007-01-1142).
(31) Sabbe, M.; Reyniers, M.-F.; Reuter, K. *Catal. Sci. Technol.* **2012**, *2*, 2010−2024.
(32) Reuter, K. In *Modelling and Simulation of Heterogeneous Catalytic Reactions: From the Molecular Process to the Technical System*; Deutschmann, O., Ed.; Wiley−VCH: Weinheim, Germany, 2013.
(33) Temel, B.; Meskine, H.; Reuter, K.; Scheffler, M.; Metiu, H. *J. Chem. Phys.* **2007**, *126*, 204711.
(34) Reuter, K.; Scheffler, M. *Phys. Rev. B: Condens. Matter Mater. Phys.* **2006**, *73*, 045433.
(35) Hoffmann, M. J.; Scheffler, M.; Reuter, K. *ACS Catal.* **2015**, *5*, 1199−1209.
(36) Zhang, Y.; Blum, V.; Reuter, K. *Phys. Rev. B: Condens. Matter Mater. Phys.* **2007**, *75*, 235406.
(37) Liu, D.-J.; Evans, J. W. *J. Chem. Phys.* **2006**, *125*, 054709.
(38) Liu, D.-J.; Garcia, A.; Wang, J.; Ackerman, D. M.; Wang, C.-J.; Evans, J. W. *Chem. Rev.* **2015**, *115*, 5979−6050.
(39) Chase, M. W.; Curnutt, J. L.; Prophet, H.; McDonald, R. A.; Syverud, A. N. *J. Phys. Chem. Ref. Data* **1975**, *4*, 1−176.
(40) Reuter, K.; Scheffler, M. *Phys. Rev. B: Condens. Matter Mater. Phys.* **2001**, *65*, 035406.
(41) Clark, S. J.; Segall, M. D.; Pickard, C. J.; Hasnip, P. J.; Probert, M. I. J.; Refson, K.; Payne, M. C. *Z. Kristallogr.—Cryst. Mater.* **2005**, *220*, 567−570.
(42) Perdew, J. P.; Burke, K.; Ernzerhof, M. *Phys. Rev. Lett.* **1996**, *77*, 3865−3868.
(43) Henkelman, G.; Uberuaga, B. P.; Jónsson, H. *J. Chem. Phys.* **2000**, *113*, 9901−9904.
(44) Bahn, S.; Jacobsen, K. W. *Comput. Sci. Eng.* **2002**, *4*, 56−66.
(45) Hoffmann, M. J.; Matera, S.; Reuter, K. *Comput. Phys. Commun.* **2014**, *185*, 2138−2150.
(46) Delbecq, F.; Moraweck, B.; Vérité, L. *Surf. Sci.* **1998**, *396*, 156−175.
(47) Delbecq, F.; Sautet, P. *Surf. Sci.* **1999**, *442*, 338−348.
(48) Hammer, B. *J. Catal.* **2001**, *199*, 171−176.
(49) Loffreda, D.; Delbecq, F.; Simon, D.; Sautet, P. *J. Chem. Phys.* **2001**, *115*, 8101−8111.
(50) (a) Nyberg, C.; Uvdal, P. *Surf. Sci.* **1988**, *204*, 517−529; (b) Nyberg, C.; Uvdal, P. *Surf. Sci.* **1991**, *256*, 42−49.
(51) Rainer, D. R.; Vesecky, S. M.; Koranne, M.; Oh, W. S.; Goodman, D. W. *J. Catal.* **1997**, *167*, 234−241.
(52) Yeo, Y. Y.; Vattuone, L.; King, D. A. *J. Chem. Phys.* **1997**, *106*, 1990−1996.
(53) Daté, M.; Okuyama, H.; Takagi, N.; Nishijima, M.; Aruga, T. *Surf. Sci.* **1996**, *350*, 79−90.
(54) Jorgensen, S. W.; Canning, N. D. S.; Madix, R. J. *Surf. Sci.* **1987**, *179*, 322−350.
(55) Matera, S.; Reuter, K. *Catal. Lett.* **2009**, *133*, 156−159.
(56) Matera, S.; Reuter, K. *Phys. Rev. B: Condens. Matter Mater. Phys.* **2010**, *82*, 085446.
(57) Matera, S.; Maestri, M.; Cuoci, A.; Reuter, K. *ACS Catal.* **2014**, *4*, 4081−4092.

DOI: 10.1021/acscatal.6b01344
ACS Catal. 2016, 6, 5191−5197

Supporting information: Synergistic inhibition of oxide formation in oxidation catalysis: A first-principles kinetic Monte Carlo study of NO+CO oxidation at Pd(100)

Juan M. Lorenzi[a], Sebastian Matera[b] and Karsten Reuter[a*]

[a] *Chair for Theoretical Chemistry and Catalysis Research Center, Technische Universität München, Lichtenbergstr. 4, 85747 Garching (Germany)*
[b] *Fachbereich f. Mathematik u. Informatik, Freie Universität Berlin, Otto-von-Simson-Str. 19, D-14195 Berlin (Germany)*
* To whom correspondence should be addressed E-mail: karsten.reuter@ch.tum.de

1 Adsorption of NO_2 on Pd(100)

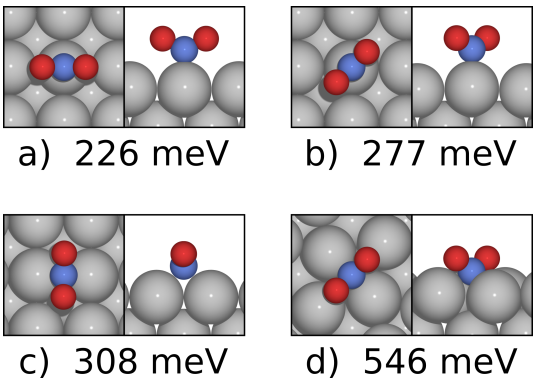

Figure S1: Metastable adsorption configurations found for NO_2 on Pd(100). Energies are relative to the most stable configuration shown in the main text.

Several adsorption geometries for the NO_2 molecule were analyzed within our density-functional theory (DFT) setup to determine the most stable configuration. For this, the molecule (in its vacuum-converged geometry) was placed on different high symmetry positions over a 4-layer thick, (2×2) Pd(100) slab. These configurations were used as initial conditions for geometry optimizations, in which the molecule and the upper two layers of the substrate were allowed to relax. The initial configurations included: (i) "upright" configurations with the N atom down over each of the high symmetry sites (top, bridge and hollow) and with the O atoms aligned either parallel, at a 45° angle or (only for the bridge site) perpendicular to the Pd-Pd direction; and (ii) "tilted" configurations, one for each of the "upright" ones, in which the molecule was rotated 45° around the N atom along an axis perpendicular to its plane, so that one of the O atoms was closer to the surface. After the geometry optimizations most of the initial configurations relaxed to the geometry presented in Fig. 1 of the main text, the one with the lowest energy observed. The four next most stable final geometries found are presented in figure S1 along with their relative energy with respect to the most stable configuration.

Table S1: Lateral interaction parameters per adsorbate for the selected lattice-gas Hamiltonian. Values in meV.

$V^{\mathrm{2NN,top}}_{\mathrm{NO-NO}}$	$V^{\mathrm{2NN,top}}_{\mathrm{CO-NO}}$	$V^{\mathrm{1NN}}_{\mathrm{O-O}}$	$V^{\mathrm{2NN,top}}_{\mathrm{CO-CO}}$
239	214	199	175
$V^{\mathrm{2NN,hol}}_{\mathrm{CO-CO}}$	$V^{\mathrm{2NN,hol}}_{\mathrm{CO-NO}}$	$V^{\mathrm{2NN}}_{\mathrm{O-NO}}$	$V^{\mathrm{2NN,hol}}_{\mathrm{NO-NO}}$
138	127	102	88
$V^{\mathrm{2NN}}_{\mathrm{CO-NO_2}}$	$V^{\mathrm{2NN}}_{\mathrm{O-CO}}$	$V^{\mathrm{2NN}}_{\mathrm{NO-NO_2}}$	$V^{\mathrm{2NN}}_{\mathrm{NO_2-NO_2}}$
86	85	64	59
$V^{\mathrm{2NN}}_{\mathrm{O-O}}$	$V^{\mathrm{2NN}}_{\mathrm{O-NO_2}}$	$V^{\mathrm{3NN}}_{\mathrm{NO-NO}}$	$V^{\mathrm{3NN}}_{\mathrm{CO-NO}}$
33	17	11	4

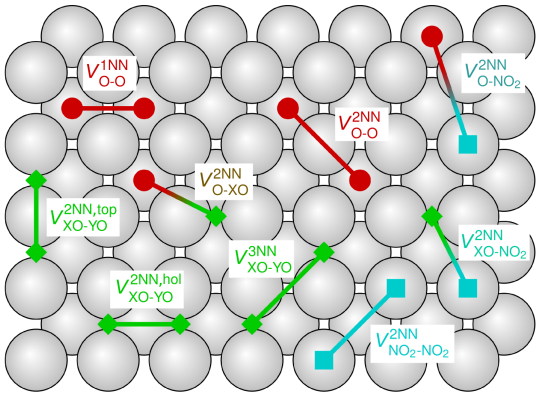

Figure S2: Representation of the interactions selected for the lattice gas Hamiltonian from table S1. XO and YO represent either CO or NO.

2 Lateral Interactions

To compute the strength of the lateral interactions and guide the definition of site-blocking rules of our 1p-kMC model, we calculated a database of DFT energies for different overlayer configurations. Adsorbates were placed on their corresponding adsorption site in supercells containing slabs with either (2×2) or (3×2) surface unit cells and 4 layer thickness. Preliminary calculations showed that configurations containing any pair of adsorbates at distances closer than the first nearest neighbor (1NN) distance between top and hollow sites ($\sim$1.97 Å) do not correspond to potential energy minima (i.e. adsorbates moved away from the original adsorption sites during geometry optimizations). Consequently, no configuration with coadsorption at such close distances was considered.

In all configurations, O, CO and NO adsorbates and the topmost two substrate layers were allowed to fully relax during the optimizations. Aiming to describe higher coverage conditions, NO_2 was constrained to maintain a C_{4v} symmetry above the top site. Under this constraint NO_2-NO_2 interactions at 1NN top-top distance turned out extremely large and tended to corrupt the inversion of the lattice gas Hamiltonian (LGH). We correspondingly concluded on a site-blocking rule for this short distance and did not consider corresponding configurations in the database. Configurations for which any of the adsorbates was displaced to a different adsorption site were also discarded and not considered in the analysis below. Figure S5 at the end of the document schematically shows the resulting 97 DFT calculated configurations that were used. Binding energies at the zero coverage limit were taken from calculations with a single adsorbate in (3×3) surface unit cells (0.11 ML coverage).

The DFT energies obtained for these configurations were used to fit a short-ranged LGH. Due to the relatively large number of adsorbates, we considered pairwise interactions only. Starting with a set of 23 interaction figures, and following the approach used by Zhang *et al.*,[S1] we found that the most accurate LGH (i.e. that which minimizes the leave-one-out cross validation (LOO-CV) score[S1]) corresponds to the one presented in table S1, in which the 16 interactions shown in Fig S2 were selected. However, even when only allowing a maximum of 12 interactions, the strongest interactions in table S1 are selected with values that differ by less than 20 meV from the corresponding values in table S1. Additionally, we have also performed the same analysis by excluding all configurations (and interactions) containing NO_2. Under these conditions we observe that again the 9 strongest NO_2-free interactions from table S1 are selected, and that the corresponding values differ again by less that 30 meV. We are thus

confident that the symmetrized treatment given to NO_2 does not have important effects on the interactions between the other species at the level of accuracy we aim at in this analysis. The highly repulsive interaction values obtained for the shortest-range distances in table S1 and the robustness with which they are obtained, fully justifies the site-blocking rules employed in the 1p-kMC model in the main text.

3 Influence of the blocking-rules scheme

The set of blocking rules used was defined such that all interactions stronger than 130 eV per adsorbate would be blocked. This corresponds to prohibiting (cf. table S1)

a. O-O coadsorption at 1NN hollow-hollow distances

b. CO-CO, CO-NO and NO-NO coadsorptions at 2NN bridge-bridge distances *across top sites*, and

c. CO-CO coadsorptions at 2NN bridge-bridge distances *across hollow sites*

in addition to blocking coadsorptions at distances equal or smaller than 1.97 Å (which do not even correspond to metastable configurations as discussed in the previous section). This was done to keep our extended set of blocking rules fully consistent with the one used by Hoffmann and Reuter.[S2]

The robustness of our results with respect to this choice has been systematically checked as follows: Fig. S3 compares the TOF for CO oxidation predicted with the blocking-rules scheme just described (solid lines, same data as in Fig. 3 of the main text), with the predictions from two alternative schemes, one "softer" (dashed lines) and one "harder" (dotted lines). The "softer" model corresponds to releasing the blocking of CO-CO coadsorption at 2NN bridge-bridge distance across hollow sites (effectively raising the blocking "cut-off energy" to 170 eV). It can be seen that the effects are completely negligible. On the other hand, the "harder" scheme extends blocking by prohibiting all CO-CO, CO-NO and NO-NO coadsorptions at 2NN bridge-bridge distances (i.e. both across hollow and top sites). Although somewhat larger than in the previous case, differences are still small. The most notable deviation is observed for the "poisoned" case, and accounts to a shift of the transition in the p_{NO} axis. The farther reaching interactions included into the site-blocking of this "harder" scheme have only smaller finite values. In reality, adsorption into corresponding configurations will not be entirely blocked. We therefore expect the effect predicted by the "harder" scheme to actually represent an upper bound, i.e. the true quantitative effect of neglecting the finite farther-reaching repulsive interactions in the main model will be less than what is predicted by the "harder" scheme. All in all, this analysis thus shows clearly that none of the qualitative effects put forward in this work are affected by the details of the employed blocking-rule scheme.

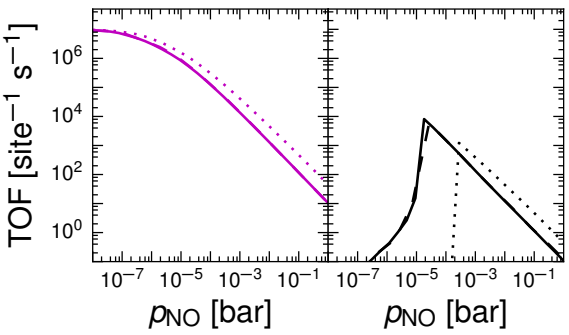

Figure S3: TOF as a function of NO partial pressure and at $T = 600\,K$ for the "high activity" (magenta, left panel) and "poisoned" (black, right panel), predicted using different blocking-rule schemes. Solid lines correspond to the results reported in the main text (cf. Fig. 3); dashed lines, to a softer lateral interaction model; and dotted lines, to harder one (details in text).

4 Results with modified process lists

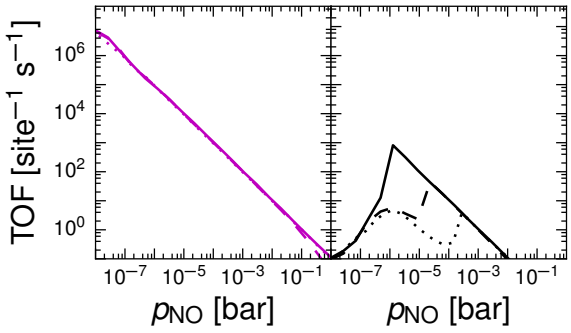

Figure S4: CO oxidation TOFs at $T = 600\,\mathrm{K}$ for the "high activity" (magenta, left panel) and "poisoned" (black, right panel) cases as in Fig. 3 of the main text. Compared are results from three altered 1p-kMC models: Dotted lines correspond to the model with NO oxidation completely turned off. Dashed lines correspond to a model in which NO_2 formation (but no desorption) is allowed, but dissociation is restricted (see text). Solid lines correspond to the model in which NO_2 formation and dissociation is unrestricted (but NO_2 desorption is turned off).

As discussed in the main text, we have analyzed different modifications to our 1p-kMC model to clearly elucidate the source of the reactivity enhancement. The modifications implemented are: (i) the NO oxidation elementary process was completely turned off; (ii) the surface NO oxidation process is on, but the NO_2 desorption process is turned off and the NO_2 dissociation process is restricted, such that this intermediate can only dissociate into the NO + O configuration that initially generated it; and (iii) only NO_2 desorption is turned off and NO_2 formation and dissociation is unrestricted. The difference between cases (ii) and (iii) allow to isolate the effects of the NO_2 mediated O mobility schematically shown in Fig 5 of the main text. The resulting CO oxidation TOF for each of these cases is presented in Fig S4, with results from cases (i), (ii) and (iii) shown with dotted, dashed and solid lines, respectively. As discussed, for the "poisoned" case the incremental addition of the different elementary reaction events shifts the position of the transition from O-poisoned to the NO+O reactive state to lower values of p_{NO}.

5 Kinetic Monte Carlo vs. mean-field microkinetics

Mean-field microkinetics is generally not able to properly model a system with strong lateral interactions. Following the approach by Temel *et al.*[S3] we compared the results of our 1p-kMC model to a mean-field description based on exactly the same elementary process list and exactly the same first-principles based rate constants. In complete analogy to the work by Temel *et al.*[S3] for CO oxidation at $RuO_2(110)$ we found the mean-field description to predict a much wider pressure range of appreciable catalytic activity at $T = 600\,\mathrm{K}$ already in the absence of NO. In fact, no O-poisoned regime is obtained in the entire pressure range shown in Fig. 2 of the main text. With this deficiency the mean-field model would correspondingly not be able to reliably capture the extended activity range observed in the 1p-kMC model at finite NO pressure.

References

(S1) Zhang, Y.; Blum, V.; Reuter, K. *Phys. Rev. B* **2007**, *75*, 235406.

(S2) Hoffmann, M. J.; Reuter, K. *Top. Catal.* **2014**, *57*, 159–170.

(S3) Temel, B.; Meskine, H.; Reuter, K.; Scheffler, M.; Metiu, H. *J. Chem. Phys.* **2007**, *126*, 204711.

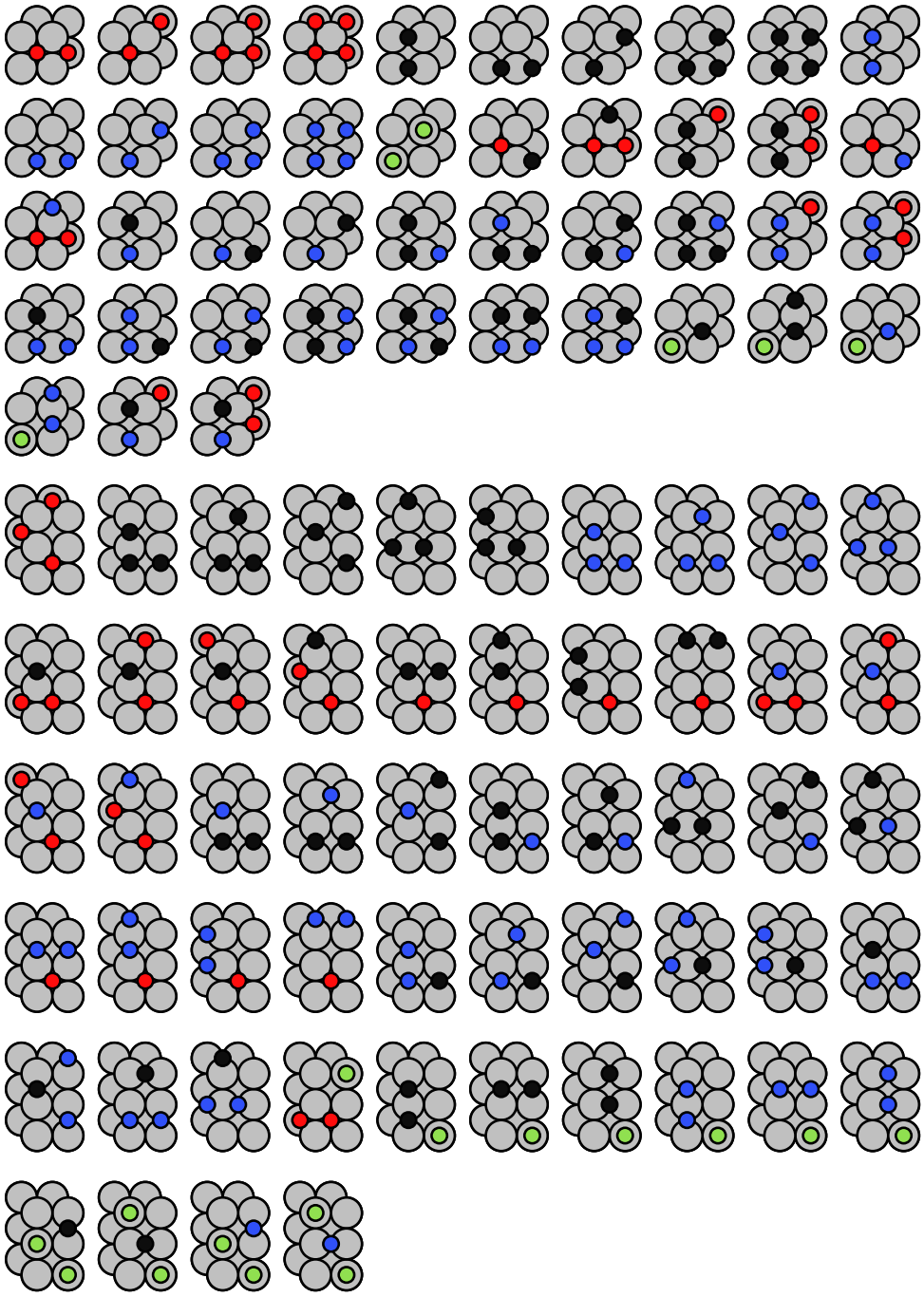

Figure S5: Configurations used for calculating the lateral interaction parameters. Gray circles represent Pd substrate atoms. Red, black, blue and green circles represent O, CO, NO, and NO_2 adsorbates, respectively.

A.2 Paper 2

Local-metrics error-based Shepard interpolation as surrogate for highly non-linear materials models in high dimensions.
Juan M. Lorenzi, Thomas Stecher, Karsten Reuter and Sebastian Matera
Accepted for publication in the Journal of Chemical Physics.

Local-metrics error-based Shepard interpolation as surrogate for highly non-linear materials models in high dimensions

Juan M. Lorenzi,[1, a)] Thomas Stecher,[1] Karsten Reuter,[1] and Sebastian Matera[2]
[1)] *Chair for Theoretical Chemistry and Catalysis Research Center, Technische Universität München, Lichtenbergstr. 4, 85747 Garching (Germany)*
[2)] *Fachbereich f. Mathematik u. Informatik, Freie Universität Berlin, Otto-von-Simson-Str. 19, D-14195 Berlin (Germany)*

(Dated: 16 October 2017)

Many problems in computational materials science and chemistry require the evaluation of expensive functions with locally rapid changes, such as the turn-over frequency of first principles kinetic Monte Carlo models for heterogeneous catalysis. Because of the high computational cost, it is often desirable to replace the original with a surrogate model, e.g. for use in coupled multiscale simulations. The construction of surrogates becomes particularly challenging in high-dimensions. Here, we present a novel version of the modified Shepard interpolation method which can overcome the *curse of dimensionality* for such functions to give faithful reconstructions even from very modest numbers of function evaluations. The introduction of local metrics allows us to take advantage of the fact that, on a local scale, rapid variation often occurs only across a small number of directions. Furthermore, we use local error estimates to weight different local approximations, which helps avoiding artificial oscillations. Finally, we test our approach on a number of challenging analytic functions as well as a realistic kinetic Monte Carlo model. Our method not only outperforms existing isotropic metric Shepard methods but also state-of-the-art Gaussian Process regression.

PACS numbers: 82.65.+r,82.20.-w,05.10.Gg,05.10.Ln,07.05.Kf,07.05.Mh,07.05.Tp
Keywords: kinetic Monte Carlo, machine learning, interpolation, surrogate models

I. INTRODUCTION

The interest in multiscale modeling approaches for materials science and chemistry has exploded in the last two decades. One important class of such approaches employs sequential (or hand-shaking) strategies, where a smaller scale model is employed as the closure of a larger scale model. In the simplest case, this just requires the adjustment of a finite set of parameters, e.g. the viscosity of an isothermal Newtonian fluid. In the general setting, the analytic form of the closure is not known and the small-scale model is required to determine functions of the large-scale variables. A prototypical example is *ab initio* molecular dynamics, where the functional dependence of the Potential Energy Surface (PES) is obtained from first principles electronic structure simulations. Employing a microscale simulation every time the function is evaluated is, of course, very time-consuming and then usually the bottleneck of such multiscale approaches. One way to accelerate this is to parametrize a surrogate model using the small-scale simulations and employ this in the large-scale simulations instead of the microscale simulator. A number of different general purpose surrogate models have been used in this way, including Neural Networks[1], Gaussian Processes[2–4], full[5] and sparse grid splines[6], and modified Shepard interpolation[7–9].

The present work grew out of our efforts to couple first-principles kinetic Monte Carlo (1p-kMC) to Computational Fluid Dynamics (CFD) simulations for reactive flows over a heterogeneous catalyst, using local modified Shepard interpolations[8,9] and extensions thereof[10,11]. Here, the surrogate model is used to interpolate the catalytic turnover frequency (TOF) obtained from the mesoscopic 1p-kMC simulations as a function of the temperature T and the partial pressures $\{p_i\}$ of the N_{spec} different gas phase species. The surrogate model then serves as a boundary condition in CFD. A corresponding use of surrogate models for coupling mean-field microkinetic models to CFD is widespread, including the use of splines[12,13] or *in situ* adaptive tabulation[14]. The latter has also been employed in the kMC+CFD context for the simulation of crystal growth and catalysis[15,16], albeit with a phenomenological kMC model.

Efficiently and reliably interpolating 1p-kMC based TOF maps is a challenging problem. Under the appropriate coordinate transformation (i.e. logarithmic pressures and TOF, as well as inverse temperature) the maps display an approximately linear behavior for large parts of the $(\{p_i\}, T)$-space. Usually, these linear regions correspond to steady-state kinetic "phases", characterized by a defined coverage regime on the catalyst.[17,18] In contrast, the behavior at the boundaries between such "phases" is highly non-linear and characterized by a rapid change of the TOF value and gradient within a narrow range of p_i and T values. This is challenging for most interpolation methods and normally it is necessary to sample such regions densely to get satisfactory results. This is aggravated further in higher dimensions (i.e. for problems with a larger number of gas-phase species N_{spec}), because the number of points required to densely fill space grows exponentially with the number of dimen-

[a)] juan.lorenzi@tum.de

sions (the so-called *curse of dimensionality*). For this reason, 1p-kMC+CFD studies have, up to now, been limited to problems involving only a small number of gas-phase species, such as CO oxidation,[10,11,18] where, in addition to the temperature, only the CO and oxygen partial pressures play a role. Modeling more complex pathways would, of course, be of great interest. For example, in competitive CO+NO oxidation[19], the dimensionality is already five (at least), because the TOFs also depend on the partial pressures of NO and NO_2.

In this article, we present an extension to the popular local modified Shepard interpolation[20] addressing the problem of approximating functions with sharp transitions in higher dimensions. Our approach constructs a local metric for each data point (node), which is then used to determine local polynomial approximations (the nodal functions), which are combined to estimate function values at arbitrary points (query points). In this way, we can exploit (local) low-dimensionality of the target functions: sharp variations typically occur only along a few directions, while the function is smoother along the others. Having metrics that are *local* is then crucial, because the direction of rapid change might vary across the domain. In the 1p-kMC context, sharp variations in rates are often associated with phase transitions in the surface coverages. These transitions have interfaces which are quasi-$(D-1)$-dimensional for D dimensional problems. Close to such regions, only the direction perpendicular to the transition region presents rapidly changing behavior, and thus the function is approximately one-dimensional there. Where two interfaces meet (i.e. around points where three phases coexist) the behavior will be approximately two-dimensional. The idea of a local metric is shared with Locally Weighted Projection Regression,[21] which differs, however, in the way the metric is determined and the nodal functions are blended. Most significantly, we do not base the blending on the distances between the query point and the nodes, but on estimates of the approximation quality of the nodal functions at the query points[10,22].

This combination of a local metric with error estimate based weighting largely suppresses artificial wiggles and especially overshoots close to sharp changes, while the resulting interpolant is once differentiable by construction. Our method produces accurate and qualitatively correct interpolations of a number of test functions with rapid, localized transitions, even in higher dimensions (up to at least 7) and from small data sets. All these properties are desirable in a multiscale context: overshoots and wiggles might introduce qualitatively wrong behavior, e.g. artificial hysteresis in 1p-kMC/CFD couplings; large-scale solvers often require continuous derivatives, e.g. many CFD codes incorporate the stiff chemistry using implicit ODE solvers[23]; finally, the small-scale models are often very costly and a large number of function evaluations is usually not affordable. While our present focus is on activity data, especially from 1p-kMC, our approach is very general and should also be of help in other fields, possibly with suitable adaptations.

This paper is structured as follows. In section II, we present the methodology of our interpolation, as well as the details of other versions of the Shepard interpolant that are relevant to this work. In section III, we use examples to demonstrate the performance of our interpolant. The examples include a collection of analytic test functions (cf. subsection III A) and a realistic 1p-kMC reactivity map (cf. subsection III B). In section IV, we offer conclusions on our findings and discuss future directions which might lead to an improvement of the devised methodology.

II. METHODS

Our approach belongs to the class of modified Shepard (MS) interpolation methods. They are *meshless*, scattered data interpolation methods, because they require neither the input data to lay on a predefined grid nor any kind of triangulation (meshing). The defining characteristic of the MS approach is the use of a collection of local approximations of the target function, centered on the data points. The interpolant itself is evaluated as a weighted sum of these approximations.

In section II A we introduce the common features of MS interpolation methods as well as one of the standard versions, which we will call distance-based MS (cf. section II A). In section II B, we discuss some of the limitations of distance-based MS and a way to overcome these by using an estimate of the error of the local approximations as the basis for the weighting. This constitutes what we call error-based MS, first introduced in ref.[10]. In section II C we consider problems arising from the use of isotropic weighting schemes when dealing with high-dimensional functions with localized regions of rapid change. We explain how local metrics can be constructed and combined with the error estimates to solve such issues, resulting in the error-based local metric MS (EBLMMS) method. Finally, in section II D, we discuss our choice of input data, i.e. the set of independent variables for which we evaluate the original function.

A. Modified Shepard Interpolation

Formally, our aim is to interpolate a *target function*

$$f : \mathbb{R}^D \to \mathbb{R} \tag{1}$$

within a certain D-dimensional domain $\Omega = [x_1^{\min}, x_1^{\max}] \times ... \times [x_D^{\min}, x_D^{\max}] \subset \mathbb{R}$. D is the number of parameters that define the value of the function (e.g. $D = N_{\text{spec}}+1$ in the above 1p-kMC/CFD coupling example). The interpolant is constructed using a set of points $X = \{\mathbf{x}_1, \mathbf{x}_2, ..., \mathbf{x}_N\} \subset \Omega$, known as *nodes*, and the corresponding function values $F = \{f_1, f_2, ..., f_N\} \subset \mathbb{R}$, with $f_i = f(\mathbf{x}_i)$.

The formula for the modified Shepard interpolant is[20]

$$g(\mathbf{x}) = \frac{\sum_{k=1}^{N} w_k(\mathbf{x}) Q_k(\mathbf{x})}{\sum_{k=1}^{N} w_k(\mathbf{x})} = \sum_{k=1}^{N} W_k(\mathbf{x}) Q_k(\mathbf{x}) \quad , \quad (2)$$

where the *nodal functions* Q_k are local approximations of f around the nodes $\mathbf{x}_k$, w_k are the *relative interpolation weights*, and

$$W_k(\mathbf{x}) = \frac{w_k(\mathbf{x})}{\sum_{i=1}^{N} w_k(\mathbf{x})} \quad (3)$$

are the *normalized interpolation weights*, or simply the *weights*.

Typically, the nodal functions are low-order polynomials, mostly first or second order. In this work, we will only consider the linear case and take

$$\begin{aligned} Q_k(\mathbf{x}) &= f_k \qquad\qquad + \mathbf{a}_k \cdot (\mathbf{x} - \mathbf{x}_k) \\ &= f_k \quad + \sum_{i=1}^{D} a_{k,i}(x_{k,i} - x_i) \quad . \end{aligned} \quad (4)$$

The coefficients $a_{k,i}$ are obtained by minimizing the weighted sum of squared errors

$$\sum_{\substack{i=1 \\ i \neq k}}^{N} \tilde{w}_k(\mathbf{x}_i) \left(Q_k(\mathbf{x}_i) - f_i\right)^2 \quad , \quad (5)$$

where we have introduced the *relative construction weights* $\tilde{w}_k(\mathbf{x}_i)$.

The flexibility in the selection of the weights w_k and $\tilde{w}_k$ allows for the definition of different classes of Shepard interpolants. In this work, however, we only consider relative interpolation weights which satisfy

$$w_k(\mathbf{x}) \geq 0 \quad (6a)$$

$$\lim_{\mathbf{x} \to \mathbf{x}_k} w_k(\mathbf{x}) = +\infty \quad (6b)$$

$$\lim_{|\mathbf{x} - \mathbf{x}_k| \to +\infty} w_k(\mathbf{x}) = 0. \quad (6c)$$

This guarantees that the normalized weights constitute a Shepard partition of unity, i.e.

$$W_i(\mathbf{x}) \geq 0 \quad (7a)$$

$$W_i(\mathbf{x}_k) = \delta_{ik} \quad (7b)$$

$$\sum_{i=1}^{N} W_i(\mathbf{x}) = 1 \qquad \forall \mathbf{x}. \quad (7c)$$

The property (7b) and the fact that $Q_k(\mathbf{x}_k) = f_k$ ensure that the interpolant goes through each of the datapoints exactly (i.e. $g(\mathbf{x_i}) = f_i \ \forall i$). By releasing one (or both) of these conditions, the method could easily be extended to also deal with noisy input data. However, this is outside the scope of this work.

A simple ansatz for the weights would be $w_k(\mathbf{x}) = \tilde{w}_k(\mathbf{x}) = |\mathbf{x} - \mathbf{x}_k|^{-2}$, i.e. inverse-square decay, which was used for the interpolation weights by Shepard in his original work[24]. In most cases, however, such long-range weights are undesirable and we want to construct the local approximations Q_k using only points close to the corresponding node $\mathbf{x}_k$. Accordingly, we can only expect such functions to be predictive near $\mathbf{x}_k$.

For this reason, alternative versions of Shepard interpolation use weights which either (a) decay (much) faster than inverse-square at longer distances[7,21] or (b) have finite support, i.e. the weights are only non-zero in a vicinity of the nodes[20,25,26]. In the latter case, which is the one we use in this work, each of the nodal functions Q_k is built using only a subset of the nodes $\sigma_k \subset X$. Such subsets are called *stars*. Correspondingly, the range of influence of each node $\mathbf{x}_k$ is limited to a region

$$\omega_k = \{\mathbf{x} \mid w_k(\mathbf{x}) > 0\} \subset \Omega \quad (8)$$

around it. Such regions are called *clouds*. The simplest choice is to make clouds and stars isotropic. This is most easily achieved by making $w_k(\mathbf{x})$ and $\tilde{w}_k(\mathbf{x})$ non-zero only inside D-Balls centered around $\mathbf{x}_k$.[25] In the seminal work of Renka,[20] relative interpolation weights are correspondingly defined according to

$$w_k(\mathbf{x}) = \frac{\left(1 - \frac{d_k(\mathbf{x})}{R_{w,k}}\right)_+^2}{\left(\frac{d_k(\mathbf{x})}{R_{w,k}}\right)^2} \quad (9)$$

and construction weights according to

$$\tilde{w}_k(\mathbf{x}) = \frac{\left(1 - \frac{d_k(\mathbf{x})}{R_{q,k}}\right)_+^2}{\left(\frac{d_k(\mathbf{x})}{R_{q,k}}\right)^2}, \quad (10)$$

where $d_k(\mathbf{x}) = ||\mathbf{x} - \mathbf{x}_k||_2$ is the Euclidean distance between query point $\mathbf{x}$ and node $\mathbf{x}_k$ and

$$(x)_+ = \begin{cases} x, \text{if } x \geq 0 \\ 0, \text{if } x < 0 \end{cases} \quad . \quad (11)$$

The radii $R_{w,k}$ are chosen such that a given number of nodes N_w fall inside each cloud σ_k. Similarly, the $R_{q,k}$ are chosen such that all stars σ_k contain a given number N_q of nodes. A representation of these elements is given in Fig. 2a.

Alternatively, clouds can be defined such that each query point is inside the clouds of exactly N_w nodes. In this formulation distance based weights can be defined according to

$$w_k(\mathbf{x}) = \frac{\left(1 - \frac{d_k(\mathbf{x})}{R_w(\mathbf{x})}\right)_+^2}{\left(\frac{d_k(\mathbf{x})}{R_w(\mathbf{x})}\right)^2} \quad , \quad (12)$$

where $R_w(\mathbf{x})$ depends on the query point $\mathbf{x}$ and is set to the distance to its N_wth neighbor. Such a

method is implemented in the numerical subroutine library ALGLIB.[26]

N_q and N_w are the two adjustable parameters of this method. The smallest reasonable value for N_q is the number of free parameters in the nodal functions (i.e. D for linear nodal functions), in order to be able to fit them to the N_q nodes. In practice, N_q is chosen considerably larger than D to avoid overfitting of the nodal functions. N_w represents the range of validity of nodal functions and controls how much clouds overlap. *A priori*, we would expect that N_q and N_w should not differ very much, as they ultimately represent the range in which we expect the target function to be reasonably approximated by linear functions.

In what follows, we will refer to methods using construction weights from eq. (10) and evaluation weights from either eq. (9) or eq. (12) as distance-based MS (DBMS) to differentiate them from the error-based methods which we define in the next section.

B. Error-Based Modified Shepard Interpolation (EBMS)

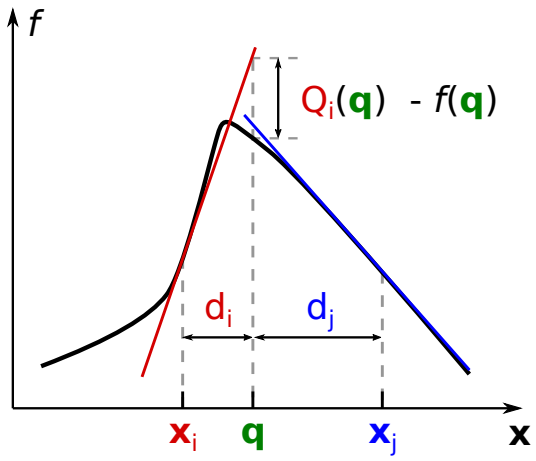

FIG. 1. The cause for overshoots with distance-based weights. The black curve represents the target function; colored straight lines represent the nodal functions Q_i and Q_j of nodes $\mathbf{x}_i$ and $\mathbf{x}_j$, respectively. The distance-based relative interpolation weight associated to Q_i at query point $\mathbf{q}$, i.e. $w_i(\mathbf{q})$, will be larger than that for $\mathbf{x}_j$, i.e. $w_j(\mathbf{q})$, even though the latter's nodal function predicts the target function value $f(\mathbf{q})$ considerably better.

Purely distance-based weights are a natural choice when we expect target function values at a given query point to be predicted better by nodal functions of closer nodes than by nodal functions of more distant nodes. This assumption might be violated by functions with concentrated regions of large gradient changes. An illustration of this is presented in Fig. 1, where nodes $\mathbf{x}_i$ and $\mathbf{x}_j$ are located on different sides of such a region. The query point $\mathbf{q}$ is on the same side as $\mathbf{x}_j$ but closer to $\mathbf{x}_i$ ($d_i < d_j$). The prediction of nodal function Q_i (red straight line in the figure) at point $\mathbf{q}$ is much worse than that of Q_j (blue straight line) but the distance-based weight of the former will be higher ($w_i(\mathbf{q}) > w_j(\mathbf{q})$). We therefore obtain a largely overpredicted function value, even though we have a better approximation available.

Alternatively, we propose to weight nodal functions according to how well they predict the target function, e.g. inversely proportional to their error

$$w_k(\mathbf{x}) \propto \frac{1}{|Q_k(\mathbf{x}) - f(\mathbf{x})|} \quad . \tag{13}$$

Using an expression like eq. (13) results in a larger weight for Q_j at query point $\mathbf{q}$ than for Q_i, because $|Q_i(\mathbf{q}) - f(\mathbf{q})| \gg |Q_j(\mathbf{q}) - f(\mathbf{q})|$. Of course, the target function value and, consequently, the nodal function error $|Q_k(\mathbf{x}) - f(\mathbf{x})|$ are unknown at arbitrary query points.

The key idea behind error-based modified Shepard interpolation (EBMS)[10] is to use computationally cheap *error estimates* instead

$$\epsilon_k(\mathbf{x}) \sim |Q_k(\mathbf{x}) - f(\mathbf{x})| \quad . \tag{14}$$

An analytic expression for such estimates can be obtained from a formula giving upper bounds of the nodal function's error[22], which can be parametrized using the *known errors* of the nodal functions on nearby nodes.

We can formally derive the EBMS error estimates as follows: Let $\partial_i f$, with $i = 1, ..., D$, be the (unknown) partial derivatives of the target function f. From the theory of Taylor expansions we have

$$\begin{aligned} f(\mathbf{x}) &= T_k(\mathbf{x}) + Z_k(\mathbf{x}) \\ &= f_k + \sum_{i=1}^{D} \partial_i f(\mathbf{x}_k)(x_i - x_{k,i}) + Z_k(\mathbf{x}) \quad , \end{aligned} \tag{15}$$

where T_k is the first-order Taylor expansion of f around $\mathbf{x}_k$ and Z_k is the residual. It can be shown that, for continuously differentiable target functions, there exists a scalar $b_{k,2} \geq 0$ such that[22]

$$|Z_k(\mathbf{x})| \leq b_{k,2} \left(d_k(\mathbf{x})\right)^2 \qquad \forall \mathbf{x} \in \omega_k \quad , \tag{16}$$

where $d_k(\mathbf{x}) = ||\mathbf{x} - \mathbf{x}_k||^2$, as before. With this in mind, we obtain a bound for the error $|Q_k(\mathbf{x}) - f(\mathbf{x})|$ within the cloud ω_k

$$\begin{aligned} &|Q_k(\mathbf{x}) - f(\mathbf{x})| = |Q_k(\mathbf{x}) - T_k(\mathbf{x}) - Z_k(\mathbf{x})| \\ &\leq \sum_{i=1}^{D} |\partial_i f(\mathbf{x}_k) - a_{k,i}||x_i - x_{k,i}| - |Z_k(\mathbf{x})| \quad , \end{aligned} \tag{17}$$

where we have applied the definition of the nodal functions, eq. (4), and the triangle inequality. Combining the fact that $\sum_{i=1}^{D} |x_i - x_{k,i}| \leq D d_k(\mathbf{x})$ with eq. (16), and taking

$$b_{k,1} = D \max_{1 \leq i \leq N} (\{|\partial_i f(\mathbf{x}_k) - a_{k,i}|\})$$

we obtain a formula for a bound on the errors of nodal functions

$$|Q_k(\mathbf{x}) - f(\mathbf{x})| \leq b_{k,1} d_k(\mathbf{x}) + b_{k,2} \left(d_k(\mathbf{x})\right)^2 , \qquad (18)$$

which we can use as an analytic expression for our error estimates

$$\epsilon_k(d_k(\mathbf{x})) = b_{k,1} d_k(\mathbf{x}) + b_{k,2} (d_k(\mathbf{x}))^2 \quad . \qquad (19)$$

We need the error estimates ϵ_k to approximate the prediction error of Q_k. To achieve this, the coefficients $b_{k,1}$ and $b_{k,2}$ are fitted by minimizing the sum of squared differences between the error estimates and the known errors in the cloud

$$\sum_{\mathbf{x_i} \in \omega_k} \left(\epsilon_k(d_k(\mathbf{x}_i)) - |Q_k(\mathbf{x}_i) - f_i|\right)^2 \quad . \qquad (20)$$

In order to be consistent with the derivation of ϵ_k, this minimization is performed under the constraints

$$0 \leq b_{k,1}, b_{k,2} \qquad \text{and} \qquad (21a)$$
$$|Q_k(\mathbf{x}_i) - f_i| \leq \epsilon_k(d_k(\mathbf{x}_i)) \quad \text{for all } \mathbf{x}_i \in \omega_k \quad . \qquad (21b)$$

Having obtained an expression for the error estimates ϵ_k, we can now formally define the EBMS interpolant: the nodal functions Q_k are built exactly as in DBMS (cf. eqs. (4), (5) and (10)), but the interpolation weights are given by

$$w_k(\mathbf{x}) = \frac{\lambda(R_w, r_w; d_k(\mathbf{x}))}{\epsilon_k(d_k(\mathbf{x}))} \quad , \qquad (22)$$

where λ is a localization function

$$\lambda(R, r; d) = \qquad (23)$$
$$\begin{cases} 1, \text{if } d < R - r \\ -2\left(\frac{R-d}{r}\right)^2 + 3\left(\frac{R-d}{r}\right)^3, \text{if } R - r \leq d < R \\ 0, \text{if } R \leq d \quad . \end{cases}$$

λ guarantees that the w_k have finite support and that the resulting interpolant is once differentiable. The width of the transition, i.e. the region where $0 < \lambda < 1$, can be made small by choosing $r_w << R_w$, which ensures that the weights are purely error based (except for the localization). It has already been shown that error-based weights very effectively alleviate overshoots in DBMS for low dimensional cases[10]. In section III A, we show that this also holds for higher dimensional functions.

Much like in the previous section, the radius R_w of equation (22) can be chosen to depend either on the node (like $R_{k,w}$ in eq. (9)) or on the query point (like $R_k(\mathbf{x})$ in eq. (12)), which changes the shape of the clouds. The EBMS implementation we use in section III is based on ALGLIB's DBMS implementation,[26] and thus uses the query point based interpolation weights.[10]

C. Local Metric Based Modified Shepard

In both DBMS and EBMS the relative construction weights $\tilde{w}_k(x)$ and the interpolation weights $w_k(\mathbf{x})$ depend only on the distance $||\mathbf{x} - \mathbf{x}_k||_2$. This isotropy corresponds to the implicit assumption that the nodal functions approximate the function equally well in all directions. However, this may not reflect the true behavior of the target function. An example of such an anisotropic function is depicted in Fig. 2. The (linear) nodal function corresponding to node $\mathbf{x}_k$ approximates the function very well at query point $\mathbf{q}_1$, but we expect a large error at query point $\mathbf{q}_2$ (at the same distance from the node as $\mathbf{q}_1$), because the function behaves highly non-linearly in the direction $\mathbf{x}_k - \mathbf{q}_2$ (as indicated by the isolines).

To get an accurate interpolation of such a function using isotropic weights, we would need to densely sample the domains of rapid change. This becomes intractably expensive in higher dimensions, even if we were able to detect these domains. An alternative is to introduce anisotropic stars and clouds. Intuitively, stars and clouds that are narrow in the directions of rapid variation and wide in the other directions are needed, as illustrated in Fig. 2. Instead of the (hyper-)spherical cloud for isotropic weights in Fig. 2a, we thus introduce a cloud which is contracted in the $\mathbf{x}_k - \mathbf{q}_2$ direction, as shown in Fig. 2b. This reduces the deviation of the target function from the linear nodal function within the cloud, even if the cloud still has the same volume.

A straightforward way to achieve anisotropic clouds is to introduce a set of $D \times D$ matrices $M_k = (m_{k,ij})$, each associated to a node. We can then introduce a set of local distance measures

$$d_k(\mathbf{x}) := ||M_k(\mathbf{x} - \mathbf{x}_k)||_2 \qquad (24)$$

and use this local metric to naturally extend the formulae from the isotropic interpolant case. Since M_k is only used to define distances, it suffices to consider *symmetric*, *positive definite* matrices. Consequently, each of them is determined by $D(D+1)/2$ coefficients.

In this formalism, the interpolation weights are given by

$$w_k(\mathbf{x}) = \frac{\lambda(1, r_0, d_k(\mathbf{x}))}{\epsilon_k(d_k(\mathbf{x}))} \quad , \qquad (25)$$

where the local metric, eq. (24), is used instead of the Euclidean distance. The clouds resulting from these error weights are D-dimensional *ellipsoids*. Notice that the M_k already contain the information giving the size of the ellipsoids. Consequently, there is no explicit radius appearing in eq. (25). The parameter r_0 defines the thickness of the shell in which $0 < \lambda < 1$. To make this parameter scale adequately with the dimension D of the problem, we define it as

$$r_0 = 1 - \sqrt[D]{1 - \rho_0} \quad . \qquad (26)$$

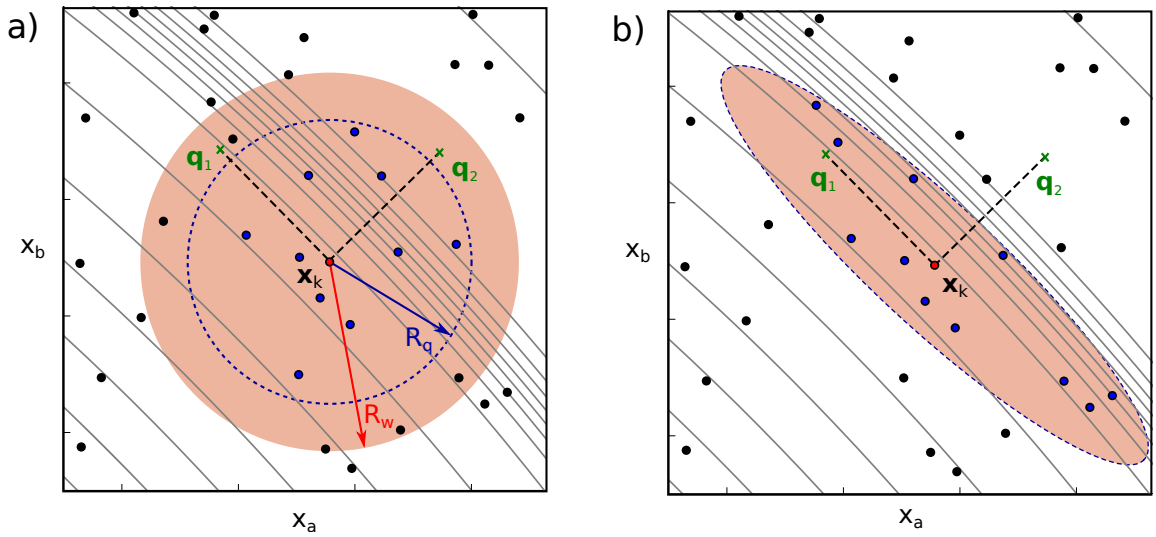

FIG. 2. Schematic representation of the different geometric elements associated with the interpolation methods described in this work. Small circles represent the nodes and gray lines represent contour levels of the target function, which accumulate in regions of rapid change. The shaded region corresponds to the cloud ω_k, i.e. the support of the interpolation weight w_k. The region delimited by the blue dashed line represents the support of construction weight $\tilde{w}_k$ and defines the star σ_k. Nodes belonging to the star are colored blue. Query points $\mathbf{q}_1$, $\mathbf{q}_2$ are separated from $\mathbf{x}_k$ by the same distance. In the isotropic case (left panel) both regions are hyper-spheres with radius R_w and R_q, respectively. The weight associated with nodal function Q_k is the same at query points $\mathbf{q}_1$ and $\mathbf{q}_2$, i.e. $w_k(\mathbf{q}_1) = w_k(\mathbf{q}_2)$. In the anisotropic case (right panel), the supports of w_k and $\tilde{w}_k$ are coinciding hyper-ellipsoids, such that the weight associated with Q_k is positive at query point $\mathbf{q}_1$ but zero at point $\mathbf{q}_2$, i.e. $w_k(\mathbf{q}_1) > w_k(\mathbf{q}_2) = 0$.

This ensures that the fraction of the cloud's volume taken by the shell is ρ_0 (the proof is given in the supplementary material, SM). In this work we use $\rho_0 = 0.1$.

In this local metric based MS (LMMS) the nodal functions Q_k are still constructed by minimizing eq. (5), but now using anisotropic construction weights. We can generalize the isotropic construction weights from eq. (10) to

$$\tilde{w}_k(\mathbf{x}) = \frac{(1 - \tilde{d}_k(\mathbf{x}))_+^2}{\left(\tilde{d}_k(\mathbf{x})\right)^2} \quad , \tag{27}$$

where we have introduced the local distance measure $\tilde{d}_k(\mathbf{x}) = ||\tilde{M}_k(\mathbf{x} - \mathbf{x}_k)||_2$ and the $\tilde{M}_k$ construction matrices. The supports of the $\tilde{w}_k$, also D-dimensional ellipsoids, define the anisotropic stars.

Intuitively, we expect the ellipsoids defining stars and clouds to be aligned and geometrically similar, i.e. that they can be mapped to each other through isotropic scaling, since their orientation and shape should only depend on the local gradients of the target function. Therefore, we expect $M_k = \gamma \tilde{M}_k$ for some scalar γ. For simplicity, we will only consider $\gamma = 1$ in this work, thus restricting our study to stars and clouds of equal size and shape. Although a preliminary analysis has shown the effects of γ to be small, we postpone a detailed analysis to a future study. For the sake of simplicity of exposition, in what follows, we will often use the term *clouds* instead of *clouds and stars*, even where strict conceptual analogy with the isotropic methods would favor the term *stars*.

Constructing an error estimate for use with the anisotropic version of the interpolant is straightforward. To rationalize this, it is sufficient to notice that distances from eq. (24) are simply the Euclidean distance in the transformed coordinates $\mathbf{x}'$ given by

$$\mathbf{x} \to \mathbf{x}' = M_k \mathbf{x} \quad . \tag{28}$$

Thanks to this, the formal derivation of the error estimates from section II B (cf. eqs. (15) to (19)) is valid also in the transformed coordinates. This means the error estimates ϵ_k in eq. (25) are still given by eq. (19), but using the local distance $d_k(\mathbf{x})$ from eq. (24). Correspondingly, the coefficients $b_{k,1}$ and $b_{k,2}$ are obtained by minimizing expression (20) under the constraints of eq. (21) using the local distance $d_k(\mathbf{x})$.

The only element missing is then a procedure to obtain the matrices M_k. As discussed at the beginning of this section, we want local matrices that minimize the prediction error of the nodal functions. We can quantify this with a (distance) weighted sum of errors given by

$$E(M_k) = \sum_{\substack{i=1 \\ i \neq k}}^{N} \tilde{w}_k(M_k, \mathbf{x}_i) \left(Q_k(M_k, \mathbf{x}_i) - f_i\right)^2 \quad , \tag{29}$$

where we have highlighted the dependence of the nodal

functions Q_k and the distance-based construction weights $\tilde{w}_k$ (cf. eq. (25)) on M_k.

Directly minimizing eq. (29) would often not provide useful results, since clouds will tend to shrink until the number of nodes they contain is $\leq D$, trivially resulting in $E = 0$. This would lead to overfitting of the nodal functions and/or to gaps in the cloud coverage of the domain. Instead, we would like to control the number of points that fall within a cloud, as we could in the isotropic versions of the method. We would thus want to perform the minimization, constraining the search space to M_k-matrices that produce clouds with a given number of nodes in them. However, introducing a discontinuous constraint like node counts into a numerical minimization scheme is technically difficult. To alleviate this, we have decided to impose softer constraints.

We can define two estimates of the number of points in a cloud: One given by

$$\eta_-(M_k) = \sum_{i=1}^{N} \lambda(1, r_-; d_k(\mathbf{x}_i))) \quad , \tag{30}$$

which is always equal or smaller than the actual number of nodes in the cloud $\eta_0(M_k)$; and another given by

$$\eta_+(M_k) = \sum_{i=1}^{N} \lambda(1 + r_+, r_+; d_k(\mathbf{x}_i))) \quad , \tag{31}$$

which is always $\eta_+(M_k) \geq \eta_0(M_k)$. Proof of the inequality relations for η_+ and η_- are given in the SM. The width parameters are given by

$$r_- = 1 - \sqrt[D]{1 - \rho_{\text{soft}}} \tag{32a}$$

$$r_+ = \sqrt[D]{1 + \rho_{\text{soft}}} - 1 \quad . \tag{32b}$$

In the limit $\rho_{\text{soft}} \to 0$, both width parameters tend to zero and the bounds η_- and η_+ both converge to the actual number of nodes in the cloud. However, for very low values of ρ_{soft} the λ function shows very steep gradients, which would disqualify the estimates from eqs. (30) and (31) for use in numerical optimization routines. It is necessary, therefore, to work with a finite ρ_{soft} and we have employed $\rho_{\text{soft}} = 0.2$ throughout this study.

We use eqs. (30) and (31) to define the following optimization constraints

$$\eta_-(M_k) \geq N_t \tag{33a}$$

$$\eta_+(M_k) \leq 2N_t \quad , \tag{33b}$$

which ensures that each cloud contains more than N_t but less than $2N_t$ nodes. Here, N_t is a free parameter of the interpolation method, analogous to N_q and N_w in DBMS and EBMS. In this formulation, the points in the cloud determine not only the D coefficients of the nodal functions, but also the $D(D+1)/2$ coefficients of the local matrices. For this reason, it is necessary to have $N_t \geq D(D+1)/2$.

The final necessary element, avoiding another potential pitfall, is a limit on the skewness of the matrices. For node distributions, in which they are approximately aligned, clouds will tend to extend in one direction and shrink indefinitely in the others, leading to overfitted, spurious nodal functions and gaps in the cloud coverage. We can quantify the skewness of an ellipsoid as the ratio between the length of its longest and its shortest principal semi-axes, which is equal to the ratio between the absolute values of the largest and the smallest eigenvalues of the corresponding matrix. This is the *condition number*[27] of the matrix, and can be approximated by

$$\kappa(M_k) = ||M_k||_1 ||M_k^{-1}||_1 \quad , \tag{34}$$

where $||\cdot||_1$ represents the 1-norm for $D \times D$ matrices. We penalize M_k with large κ by introducing a multiplicative factor to our cost function of the from

$$K(M_k) = 1 + \left(\frac{\kappa(M_k) - \kappa_0}{\kappa_0} \right)_+^p \quad , \tag{35}$$

where κ_0 is the value at which this penalization term starts to take effect, and $p \geq 2$. In this work we take $\kappa_0 = 100$ and $p = 4$.

In summary, local matrix coefficients are obtained by minimizing the cost function

$$C(M_k) = E(M_k) K(M_k) \tag{36}$$

subject to the constraints of eq. (33).

For the rest of this work, we will refer to the interpolation method described in this section as error-based LMMS interpolation, EBLMMS for short. We have implemented the EBLMMS method as a python[28] package, with computationally critical parts implemented as C-extensions with the help of the SWIG[29] interface generator. Linear algebra operations on bigger matrices (mainly the matrix of node coordinates), as well as the least squares optimization of the nodal function coefficients, cf. eq. (5), are done using the BLAS[30] and LAPACK[31] linear algebra libraries. Both local matrix and error estimate parameter optimizations were implemented with the help of the NLopt non-linear optimization library.[32]

The initial guess for the local matrices is taken as $M_k^0 = I_D / R_0$ where I_D is the $(D \times D)$ identity matrix and

$$R_0 = \sqrt[D]{\frac{(R_k^{NN}(N_t))^D + (R_k^{NN}(2N_t))^D}{2}} \quad , \tag{37}$$

with $R_k^{NN}(n)$ representing the distance from $\mathbf{x}_k$ to its n^{th} nearest neighbor. The algorithm used to fit the matrices is Constrained Optimization by Linear Approximations (COBYLA)[33], which is a derivative-free optimization algorithm able to handle non-linear constraints. COBYLA works by solving consecutive linear approximations of the target optimization problem. The approximations are constructed using the points in a simplex (similar to the

one used in the well-known Nelder-Mead method), which is reduced in size during the optimization.

We have explored three different stopping criteria for the optimization: (a) the value of the cost function, eq. (36), falls below some threshold value $C_{\min}$, (b) the size of the simplex (i.e. the maximum distance between vertices) is smaller than some value m_0 (which represents convergence of the change of the matrix coefficients $m_{k,ij}$), or (c) the number of cost function evaluations exceeds N_{eval}. As expected, the choice of stopping criterion affects both the quality of the interpolant and the time to reach convergence. For criterion (a), larger values of $C_{\min}$ (obviously) reduce the CPU time for determining M_k, but can affect the quality of the interpolant when the number of nodes is large (and thus the value of the cost function is small). In this work, we use $C_{\min} = 10^{-8}$ for all calculations presented in section III. We find that reducing the value of this parameter further provides only negligible gains in interpolant quality. For criterion (b), we find that it is most robust to employ a scale dependent on the local environment of the node, and thus select $m_0 = 0.05(R_k^{NN}(2N_t) - R_k^{NN}(N_t))$. Finally, criterion (c) is simply the backup for when the optimization takes too long and we employ $N_{\text{eval}} = 1000$ in this work.

In summary, we observe that the stopping criteria as well as the initial value of the M_k matrix can have a strong impact on both the quality and construction time of the interpolant. We believe this is a direction in which considerable improvements could be made to the method. However, as we will see in section III A, the method as presented can already provide better results than other state-of-the-art methods for the class of functions which are of interest in this work.

The fitting of the error estimate parameters $b_{k,1}$ and $b_{k,2}$ is achieved using the derivatives-based Method of Moving Asymptotes (MMA)[34] optimization. The initial guess for the parameters is a conservative guess

$$b_{0,1} = 10\frac{\Delta F}{\Delta X}$$
$$b_{0,2} = 10\frac{\Delta F}{(\Delta X)^2} \quad ,$$

where ΔF and ΔX are the range of variation of the function values and the (maximum) range of variation of the coordinate values, respectively. We stop the optimization, when both $b_{k,1}$ and $b_{k,2}$ change by less than 10^{-5} between two consecutive iteration steps.

For clarity, we finally present a summary of the algorithm for EBLMMS construction as pseudocode in Algorithm 1.

Algorithm 1 Construction of the EBLMMS interpolant

procedure BUILD
  Set κ_0, N_t
  Load nodes $X = (\mathbf{x}_1, ..., \mathbf{x}_N)$
  Load function values $F = (f_i, ..., f_N)$
  for `k=1 to N` **do**
    $DX \leftarrow (\mathbf{x}_1 - \mathbf{x}_k, ..., \mathbf{x}_N - \mathbf{x}_k)$
    $DF \leftarrow (f_1 - f_k, ..., f_N - f_k)$
    Get $R_k^{NN}(N_t)$, $R_k^{NN}(2N_t)$
    $M_k^0 \leftarrow I_D/R_0$ (cf. eq. (37))
    $\mathbf{a}_k$, $M_k \leftarrow$ Minimize C(...) (cf. eq. (36)) under constraints (33) using COBYLA
    $\{b_{k,1}, b_{k,2}\} \leftarrow$ Minimize eq. (20) under constraints (21) using MMA
function C(M_k, DX, DF, κ_0) ▷ eq. (36)
  $DX_{\text{scaled}} \leftarrow M_k DX$
  Get Q_k by minimizing eq. (5)
  Evaluate E (cf. eq. (29))
  Evaluate K (cf. eq. (35))
  return $E \cdot K$

D. Interpolant Construction and Quality Evaluation

In section III we construct interpolants for different target functions. In order to do this, we first need to select the location of the nodes. As this work targets applications in higher dimensions, using nodes on regular grids is not a viable option, because the number of total nodes for a given grid resolution grows exponentially with the number of dimensions, i.e. $N = n^D$ where n is the number of nodes in each coordinate. This is the so-called *curse of dimensionality*. The use of sequences of pseudo-random vectors is also not ideal for our problem. Such sequences typically show regions with a locally high or low density of points (compared to the overall density). For our purposes, regions where nodes accumulate are undesirable as these nodes could become redundant (especially in smooth regions of the test function). Correspondingly, regions locally devoid of nodes could leave parts of the domain outside of the cloud coverage.

For these reasons, we use *low-discrepancy* sequences (also known as *quasi-random* sequences or Quasi-Monte-Carlo points), which are deterministic vector sequences covering a given domain more evenly than pseudo-random vector sequences. This property is often exploited to perform high-dimensional numerical integration, where it allows accurate estimates to be obtained from relatively few function evaluations. We expect this to be beneficial for the determination of the nodal functions as well, since fitting the expansion coefficients of a polynomial approximation is closely related to integration. Specifically, we employ Sobol sequences[35,36], which are very frequently used and widely implemented. For each of the cases presented in section II, we construct the database for the interpolant by evaluating the target function on the first N vectors of the Sobol sequence of the corresponding dimension $\{\mathbf{x}_i^{\text{sobol}}\}_{i=1}^N$, for a number of different values of N.

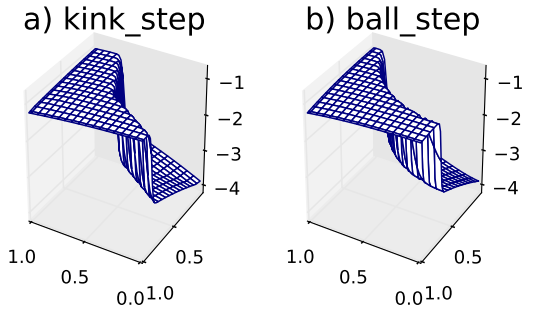

FIG. 3. Representation of the 2D version of the analytic functions used to test the interpolation method.

III. RESULTS

In this section, we analyze the performance of the newly developed interpolant qualitatively and quantitatively. This is done in comparison to isotropic versions of the MS method as well as against the state-of-the-art Gaussian process regression method (GPR), which has recently gained popularity in computational physics and materials science[2–4]. To obtain a quantitative measure of the interpolant's quality, we estimate the L1 integral of the error of the interpolation as

$$\Phi = \frac{1}{\Delta F} \frac{\sum_{i=1}^{N_{\text{test}}} |g(\mathbf{y}_i) - f(\mathbf{y}_i)|}{N_{\text{test}}} \quad , \tag{38}$$

where g is the interpolant, f the target function, and ΔF is a measure of the variation of the function values given by

$$\Delta F = \max_{\Omega}(f) - \min_{\Omega}(f) \quad . \tag{39}$$

In all cases, we will be using the N_{test} vectors of the Sobol sequence *immediately following* the points used as nodes, i.e. $\{\mathbf{y}_i\}_{i=1}^{N_{\text{test}}} = \{\mathbf{x}_i^{\text{sobol}}\}_{i=N+1}^{N+N_{\text{test}}}$. Taking $N_{\text{test}} = 2 \times 10^5$ was sufficient to converge Φ values for all tests.

In section III A, we first use a collection of analytic functions designed specifically to emulate the challenging features this method intends to tackle and to show how the method performs for problems of different dimensionality. In section III B, we then test the method by interpolating results from a realistic 1p-kMC model of heterogeneous catalysis.

A. Analytic Test Functions

We define two function classes, which can be used to construct related functions of arbitrary dimension. In this work we test dimensions from $D = 2$ to $D = 7$. A representation of the 2D test functions is given in Fig. 3. All functions from both classes have small gradients across most of the domain, but show a sharp (but differentiable), step-like transition concentrated around a $(D-1)$-dimensional hypersurface. What differentiates the two function classes is the shape of this surface, which also determines the *intrinsic dimensionality* of the functions. The transition of `kink_step` is on the union of two $(D-1)$-dimensional half-hyperplanes which meet on a common $(D-2)$-dimensional hyperplane. Therefore, this function is intrinsically two-dimensional for all D values. `ball_step` functions have the transition on the surface of a D-ball and are thus fully D-dimensional. However, they are approximately one-dimensional at length scales smaller than the radius of the ball. As we will see, our locally adaptive method is capable of exploiting this fact to improve the quality of the interpolant. The detailed definition of the test functions is given in the SM.

1. Analysis of Anisotropic Clouds

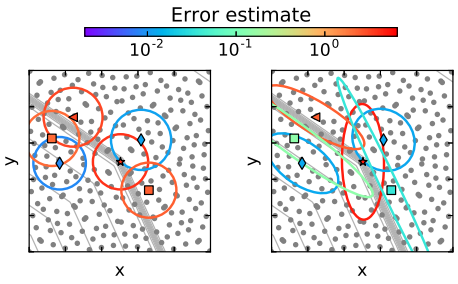

FIG. 4. Representation of clouds from selected nodes. Gray lines are contour lines of the 2D `kink_step` target function (cf. Fig. 3), gray dots mark the position of the nodes. The total number of nodes is 256. The left panel corresponds to EBMS with $N_q = N_w = 20$, the right panel corresponds to EBLMMS with $N_t = 20$. The clouds are represented by ellipses, colored according to the value of the error estimate $\epsilon_k(\mathbf{x})$. The symbols marking selected nodes (star, squares, diamonds, triangle) are used to assist the discussion in the text.

To demonstrate the working principle of the method in a concrete example, we analyze the shape of the clouds resulting from the EBLMMS interpolation of the 2D version of `kink_step` (cf. figure 3.a) using 256 nodes. Figure 4 shows a comparison between the isotropic clouds ($N_q = N_w = 20$, left) and the anisotropic clouds from EBLMMS ($N_t = 20$, right) for selected nodes, marked by colored symbols. The clouds are represented by ellipses and are colored by the estimated error of the corresponding nodal functions at their boundaries. The target function is represented by gray equidistant contour lines. In the isotropic case, all clouds close to the sharp transition show a high error. In the local metric case, the clouds generally align to the expected directions and also become narrower as they get closer to the region of strong gradient changes. Moreover, for any given node, the error at the cloud boundaries is typically smaller in the latter case. An exception is the node marked with a

star in the plot, located very close to the point in which the transition region bends. Since there is no satisfactory orientation for the cloud, the shape of the corresponding ellipsoid is spurious. This is where the error weighting scheme comes into play. The error associated with the mentioned point is very high compared to those of neighboring nodes, thus ensuring that the effect of this ill-defined cloud is minimized. Another exception is the point marked by a triangle. The resulting cloud aligns in the expected direction, but still contains several nodes that lie across the transition region. As a consequence, the quality of the corresponding nodal function is low and, correspondingly, the associated weight is low in the flat regions, where there are multiple nodal functions which better predict the function values. The nodes marked with squares are examples of these. For these nodes the local matrix optimization has shrank the ellipses to let them lie fully within a single smooth subdomain. In the isotropic case (left panel), the corresponding clouds extend across the transition region and, consequently, their nodal functions are not accurate within the respective clouds and the error estimates are large. Nodes marked with diamonds are located well within a region of smooth behavior, so the isotropic method is expected to work well. Here, the error estimates for both cases are small and the EBLMMS clouds also have a roughly circular shape.

2. Quantitative Analysis

As a quantitative test of the quality of our interpolant, we interpolate each of the test functions from Fig. 3 in the domain $\Omega = [0,1]^D \subset \mathbb{R}^D$ for dimensions $D = 2, 3, ..., 7$, and evaluate the L1 error norm from eq. (38) in each case. The EBLMMS method, as described above, includes several free parameters. While we leave the systematic assessment of the effect of each parameter to a future study, we concentrate on the N_t parameter here, which has a clear geometric interpretation and is analogous to the N_q parameter in traditional MS. We construct interpolants using $N_t = n_t D$, with $n_t = 4, 10, 20, 50, 150$, to cover a wide range of reasonable values of this parameter. For each function class, dimension D and n_t value, we build interpolants for different numbers of nodes using the first N elements of the Sobol sequence (cf. section II D). We take N as the powers of 2 between 64 and 32768 and evaluate Φ for each interpolant using eq. (38). In Fig. 5 we plot the best (smallest) Φ value obtained from all calculations (for a given test function class, dimension D and number of nodes N).

To quantify the specific effect of introducing anisotropic clouds, we also calculate the L1 error resulting from the EBMS interpolation (cf. section II B). EBMS interpolants are constructed using N_q values equal to the N_t values used for EBLMMS. Moreover, $N_w = N_q/2$, $N_w = N_q$ and $N_w = 2N_q$ are tested. The best

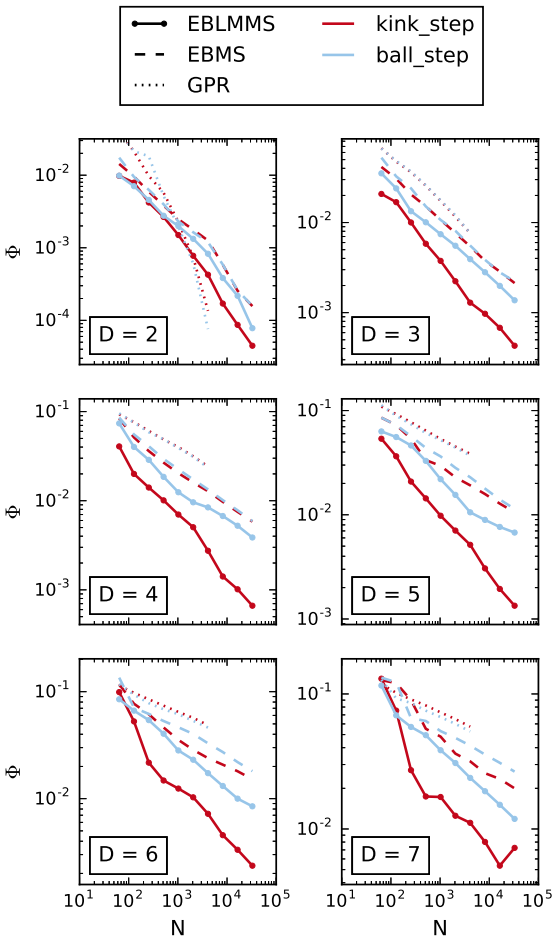

FIG. 5. Scaling of the Φ error with increasing number of nodes for the `kink_step` (dark, red lines) and the `ball_step` (light, blue lines) functions in different dimensions. The EBLMMS method (solid lines) is compared to EBMS (dashed lines) and GPR (dotted lines) methods.

Φ values for each (N_q, N_w) and each dimension are included in Fig. 5 as dashed lines. Naturally, the error for the anisotropic case is always smaller. As expected, it can also be seen that the relative improvement due to using EBLMMS is larger for higher dimensions. This is due to the fact that the rate of improvement of Φ with N (scaling) decreases more slowly for EBLMMS than for EBMS. It is also important to note that the benefit of using local metrics is much more pronounced for the intrinsically low-dimensional `kink_step` test functions than for the fully D-dimensional `ball_step` test functions.

To compare also to a non-MS method, we assess the performance of Gaussian processes regression.[37,38] Since the popular squared exponential kernel yields very low quality results for the target functions in this work, we employ the more flexible neural network kernel, which has been shown to be able to cope with discontinuities.[37]

In particular we use the diagonally anisotropic version of this kernel, which is the most general version available in the GPy library[39]. The working equations of the methods and further details are provided in the SM. Due to computer memory constraints, we only present GPR results up to node counts of $N = 4096$.

The GPR results are included in Fig. 5 as dotted lines. We observe that the errors for GPR are larger than those for EBLMMS in all cases except for $D = 2$ at larger node counts. In this low-dimensional case, node counts $N \gtrsim 1000$ correspond to very high node densities, which usually is not practical. Moreover, the error is already very low when GP becomes more accurate. Even for $D = 3$, the Shepard interpolations outperform GPR and the improvement continues to increase with dimensionality.

To complement the results presented in this section, we perform analogous calculations for two additional function classes, including one with rapid change of the gradient but not the function value. Since the conclusions drawn from the analysis of these functions are very similar to the ones just presented, we only present these results in the SM.

3. Graphical Analysis

It is important to point out that the small differences in the values of Φ in Fig. 5 do not always fully capture the qualitative improvement provided by the EBLMMS approach. To show this, we compare different interpolations of the 5D `ball_step`-function graphically. The wireframe plots in Fig. 6 show a number of interpolants evaluated in a 2D cut of the full 5D domain, which passes through the center and is parallel to coordinate directions 2 and 4 (cf. SM; we observe qualitatively very similar behavior for the nine other possible pairs of axes). All interpolants shown in Fig. 6 were constructed using the same 1024 nodes. As well as for EBLMMS, EBMS and GPR, which were used in the previous section, we also present results for the traditional, distance-based isotropic DBMS (cf. section II A) and for what we call DBLMMS (distance-based local metric MS), in which we use the local matrices M_k from EBLMMS to define the clouds, but evaluate the interpolant using distance-based interpolation weights (i.e. analogous to eq. (9), but using the local anisotropic distances instead of Euclidean distances). In the figure, we highlight overshoots by changing the wireframe-color when the value of the interpolant is above the (true) maximum of the target function. The overshoot value is reported as a percentage of the step-height (which here is 3). Regions of the wireframe in which the interpolant is equal to or lower than the maximum remain colored in dark blue (i.e. according to the lower end of the colorbar).

We start by discussing the differences between methods from the MS family, as they illustrate many of the effects discussed in the methods section. The isotropic, distance-based DBMS interpolant suffers from

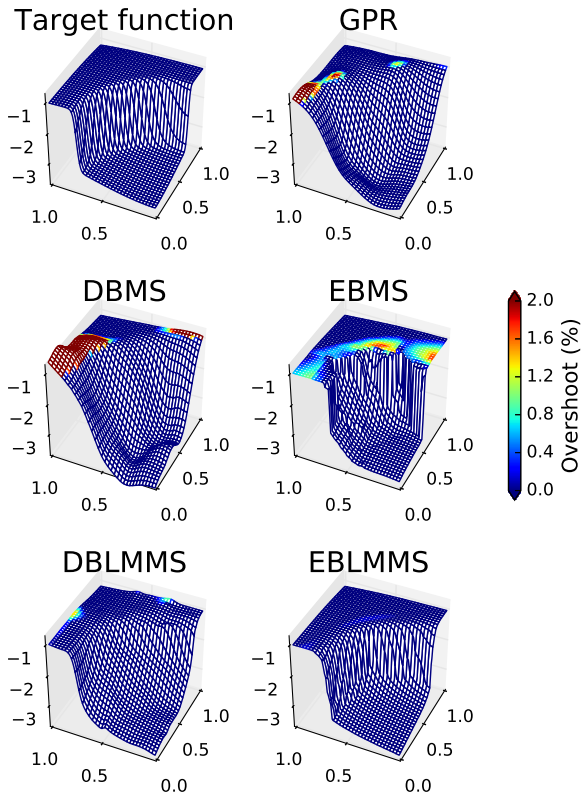

FIG. 6. Comparison of different approximations of the 5D `ball_step` test function, using a database of size $N = 1024$. Highlighted regions are colored according to how much the interpolant has exceeded the maximum value of the target function (as a percentage of the step height, i.e. 3).

overshoots, which are rather large in this example. The shape of the step is barely reproduced and the function heavily smoothed out. In the isotropic EBMS interpolant, such overshoots are considerably reduced and the interpolant matches the target function very well far from the highly non-linear region. However, this method is still unable to reproduce the shape of the transition region (the 5-ball), and some spurious features appear.

Looking at the bottom two panels, we can see that anisotropic clouds improve the interpolation quality significantly. However, the shape of the DBLMMS interpolant still shows several flaws. In particular, small oscillations appear, even in regions relatively far from the highly non-linear transition. In addition, the transition region is smoothed out considerably and its shape is not particularly well reproduced. The EBLMMS interpolant, finally, gives a much better qualitative match than any of the other cases. Even with such a small number of nodes, the shape of the highly non-linear transition re-

gion is traced very precisely. Moreover, there are no overshoots or oscillations detectable. The main source of the observed integral error Φ is a smoothing of the sharp transition, which, to some extent, is probably unavoidable using such a small dataset.

For completeness, we also show a comparison with GPR. All the spurious features observed for DBMS are present, albeit somewhat less pronounced, namely overshoots, artificial oscillations, smoothing of the step and an inability to properly capture the step's shape. As a final note, we point out that the good quality observed for EBLMMS is not strongly dependent on the exact choice of N_t. In the SM we provide wireframe plots comparing different values of this parameter to illustrate this.

B. Realistic 1p-kMC based data

Having demonstrated the capabilities of the EBLMMS method for a variety of analytic function classes and in multiple dimensions, we next tackle a realistic example, interpolating the reactivity map arising from a 1p-kMC model of heterogeneous catalysis. Specifically, we use a reduced version of the well-established and frequently studied model of CO oxidation at $RuO_2(110)$ by Reuter and Scheffler[40]. The original model is based on an extensive set of Density Functional Theory (DFT) calculations and has been shown to accurately capture experimental results.[17] It considers two adsorption site types, bridge (br) and coordinately unsaturated (cus), and two surface species, CO and O. The elementary steps modeled include molecular CO adsorption and desorption, dissociative adsorption/associative desorption of O_2, irreversible CO+O reaction and diffusional hops.

The reduced version of the model employed here was introduced by Gelß *et al.*[41] and is obtained by excluding all processes involving br sites. It has been shown that chemical kinetics is mainly controlled by the cus sites[42–44] and that the reduced model reproduces the results of the full model quantitatively for many reaction conditions[41]. Being computationally cheap, the reduced model can be evaluated for a large number of different input parameter values, which makes it a valuable test problem for our interpolation method.

The reduced model contains 7 elementary reaction steps. Single-site processes include unimolecular adsorption and desorption of CO; two-site processes, defined on pairs of nearest neighbors, include dissociative adsorption and associative desorption of O_2, CO_2 desorption as an immediate result of reaction of a pair of adsorbed CO and O, as well as diffusional hops of both species. The whole reaction mechanism is summarized in Table I.

In the context of 1p-kMC/CFD coupling, the TOF for this model is a function of 3 parameters, namely the partial pressures of CO and oxygen, p_{CO} and p_{O_2}, and the temperature T. As we intend to demonstrate the capabilities of the EBLMMS method in higher dimensional problems, in this work we will study the TOF as a function of the individual rate constants instead, i.e. we consider the 7D function

$$\begin{aligned} f : \mathbb{R}^D &\to \mathbb{R} \\ (k_{\mathrm{CO}}^{\mathrm{ads}}, k_{\mathrm{O}_2}^{\mathrm{ads}}, k_{\mathrm{CO}}^{\mathrm{des}}, k_{\mathrm{O}_2}^{\mathrm{des}}, k^{\mathrm{reac}}, k_{\mathrm{CO}}^{\mathrm{diff}}, k_{\mathrm{CO}}^{\mathrm{diff}}) &\to \mathrm{TOF} \quad . \end{aligned} \tag{40}$$

On the one hand, understanding the parametric dependence of the TOF on the rate constants is useful to perform local or global sensitivity analyses[42,43,45], which are crucial to quantify the effects of uncertainty in the determination of rate constants (due to, e.g., DFT errors). On the other hand, and more importantly for our purposes, the characteristics of this 7D function in rate constant-space are very similar to 1p-kMC TOF maps in $(\{p_\alpha\}, T)$-space. This is highlighted in models such as the one used here, in which the rate constants for non-activated adsorption are directly proportional to the corresponding partial pressures

$$k_\alpha^{\mathrm{ads}} = \frac{A_{\mathrm{uc}}}{n_\alpha} \frac{p_\alpha}{\sqrt{2\pi m_\alpha k_{\mathrm{B}} T}} \qquad \alpha = \mathrm{CO},\, \mathrm{O}_2 \quad , \tag{41}$$

where m_α are the molecular masses, A_{uc} is the surface area of the $RuO_2(110)$ unit cell, k_{B} is the Boltzmann constant and n_α is a factor arising from the multiplicity of the adsorption processes included in the model. The specific values are $A_{\mathrm{uc}} = 20.06 \mathring{A}^2$, $n_{\mathrm{CO}} = 2$ and $n_{\mathrm{O}_2} = 4$. Variation in temperature would correspond to concerted changes of the rate constants for the activated processes, which are also included in the domain of the 7D TOF function. For example, the rate constant for CO oxidation is given by

$$k^{\mathrm{reac}} = \frac{k_{\mathrm{B}} T}{h} \exp\left(-\frac{\Delta E^{\mathrm{reac}}}{k_{\mathrm{B}} T} \right) \quad , \tag{42}$$

where h is the Planck constant and ΔE^{reac} is the activation barrier for the CO oxidation elementary process. Moreover, the 7D TOF function of eq. (40) also includes variations in the parameters of the model beyond those accessible by simple changes in p_{CO}, p_{O_2} and T. For these reasons, this function is a useful proxy for a reactivity map arising from a 1p-kMC containing more species.

The advantages of using such a proxy are twofold. On the one hand, the computational cost to run this 1p-kMC model is reasonably low. This allows us to perform the 200000+ kMC calculations used as systematic test data. Just for the contour plots presented in the next section we needed 10000 results for reference, which with more complex multi-species models could cost vast amounts of computational time. On the other hand, the RuO_2 CO oxidation model has been characterized in detail both in $(p_{\mathrm{CO}}, p_{\mathrm{O}_2}, T)$-space[40,46–49] and in rate constant space[42–44] and its behavior is well understood. This makes it ideal for testing new theoretical developments such as the one presented here. In particular, the conditions under which the model presents rapid changes in reactivity are well known. Therefore, we can focus our study there, where interpolation becomes most challenging.

TABLE I. List of elementary reaction events included in the reduced model for CO oxidation at RuO_2. The default value for each rate constant, as well its range of variation, are indicated. The default values correspond to reaction conditions $T = 600K$, $p_{CO} = p_{O_2} = 1$bar.

Name	Expression	Default rate constant [1/s]	Range [1/s]
CO adsorption	$* \rightarrow CO*$	$k_{CO}^{ads} = 2.0 \times 10^8$	2.0×10^6 - 2.0×10^{10}
O_2 adsorption	$2* \rightarrow 2O*$	$k_{O_2}^{ads} = 9.7 \times 10^7$	9.7×10^5 - 9.7×10^9
CO desorption	$CO* \rightarrow *$	$k_{CO}^{des} = 9.2 \times 10^6$	9.2×10^4 - 9.2×10^8
O_2 desorption	$2O \rightarrow 2*$	$k_{O_2}^{des} = 2.8 \times 10^1$	2.8×10^{-1} - 2.8×10^3
CO oxidation	$O + CO \rightarrow 2*$	$k^{reac} = 1.7 \times 10^5$	1.7×10^3 - 1.7×10^7
CO diffusion	$CO + * \rightarrow * + CO$	$k_{CO}^{diff} = 5.0 \times 10^{-1}$	5.0×10^{-3} - 5.0×10^1
O_2 diffusion	$O + * \rightarrow * + O$	$k_{O_2}^{diff} = 6.6 \times 10^{-2}$	6.6×10^{-4} - 6.6×10^0

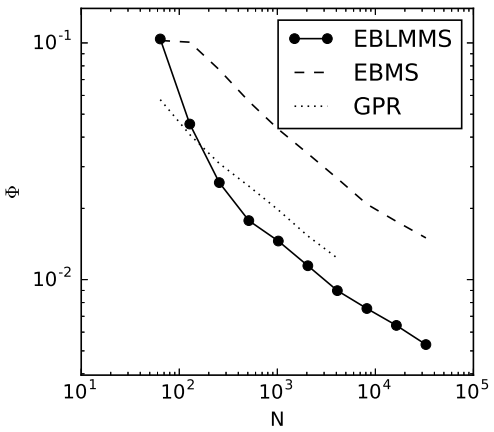

FIG. 7. Scaling of the Φ error with increasing number of nodes for the 1p-kMC model. The EBLMMS method (solid lines) is compared to EBMS (dashed lines) and GPR (dotted lines) methods.

Taking this into account, we consider the rate constants corresponding to $T = 600K$, $p_{CO} = p_{O_2} = 1$bar as the default (central) values. Such values lay close to the anticipated (second order) phase transition[44]. We define the limits of the interpolation domain such as to encompass a change in each of the rate constants of four orders of magnitude in total (i.e. two orders of magnitude higher and lower than the default cf. Table I). Considering the Arrhenius-dependence of the rate constants for activated processes on energy barriers, e.g. as in eq. (42), this accounts for changes in activation barriers ΔE of up to ~ 0.25 eV. For the non-activated adsorption processes, cf. eq. (41), this corresponds to a span of variation of 4 orders of magnitude in the partial pressures. To perform the interpolation, the domain is mapped onto a logarithmic scale and into the $[0,1]^7$ unit hypercube.

The 1p-kMC predicted CO oxidation TOF is calculated for the first 3×10^5 vectors of the 7D Sobol sequence to build the database that will later be split into nodes and test points (cf. section II D). The 1p-kMC model is implemented with the help of the `kmos` kinetic Monte Carlo simulation package[50] using a simulation cell containing 400 individual cus sites. A total of 3×10^8 kMC steps are used for relaxation and another 5×10^8 steps for steady-state sampling. To build the interpolant, the TOF values are also log-scaled. As the upper limit of the TOF scale, we take $\text{TOF}_{\max} = 3 \times 10^6 s^{-1}$, which is (slightly) larger than the maximum TOF in the database. For low TOF values, kMC sampling is challenging and simulations can sometimes result in rates equal to zero, which cannot be log-scaled. However, very low TOF conditions are of little interest in catalysis and we therefore sidestep this problem by capping the rates from below at a value of $\text{TOF}_{\min} = 10^{-4} s^{-1}$. The interpolation is then performed using the transformed TOF values, in which the $[\text{TOF}_{\min}, \text{TOF}_{\max}]$ interval is logarithmically mapped to the $[0,1]$ interval. While we observe that the relaxation times used are sufficient to reach kinetic steady state, we also find that a small amount of statistical noise remains in the data, as can be seen in the line plots of Fig. 8. To quantify this error, we recalculate 10^4 1p-kMC data points with different random number seeds and find an average absolute error value due to noise of $\sim 3\times10^{-3}$ (in the transformed TOF coordinates). However, for some points the kMC sampling error can be as large as $\sim 3 \times 10^{-1}$.

1. Quantitative Analysis and Method Comparison

Similar to section III A, the EBLMMS interpolant is built for $N_t = 28, 70, 140, 350, 700, 1050$ and the number of nodes N equal to the powers of 2 from 64 to 32768. The value of the error measure Φ, eq. (38), is evaluated for the transformed TOF values. A summary of the results is presented in Fig. 7, where we again plot the smallest value of Φ (varying N_t) obtained for each N (exactly as in Fig. 5). Even for sample sizes as small as $N \approx 2\times10^3$, we can achieve global errors of $\Phi \approx 10^{-2}$. Considering the highly non-linear behavior of the TOF (cf. Figs. 8 and 9) and the fact that such low values of N would correspond to a regular grid with only ~ 3 points in each coordinate direction, we think this is a remarkably good approximation.

In Fig. 7 we also present results from the EBMS (cf.

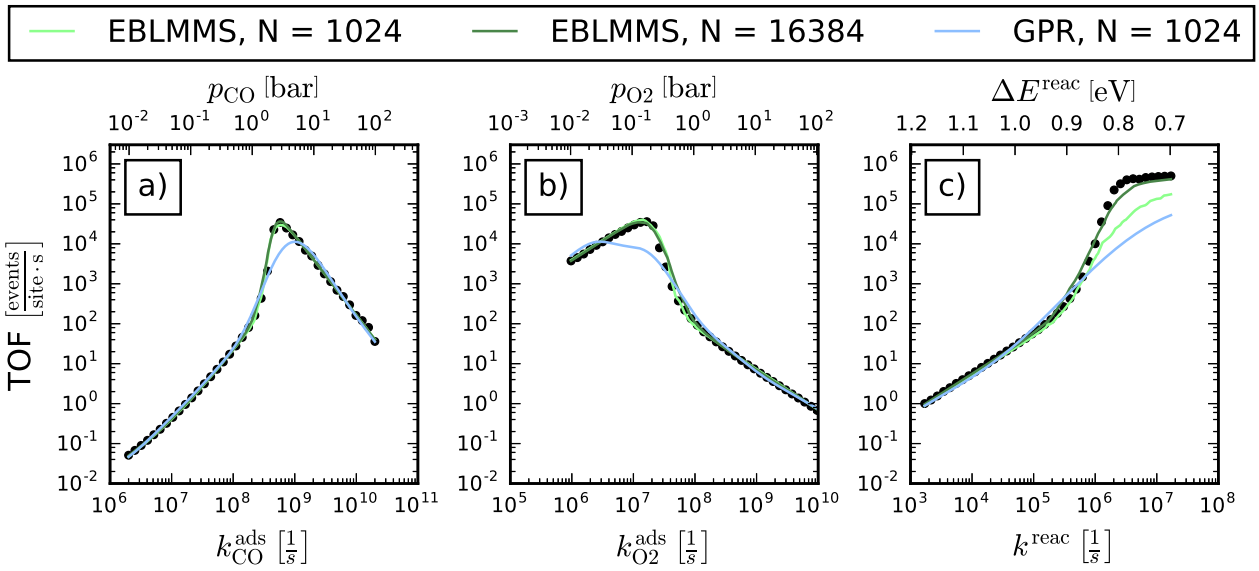

FIG. 8. 1D cuts of different 7D interpolants compared to 1p-kMC data not included in their input (dots). For each case, all but one of the rate constants where fixed at their default values (cf. tab. I). Lines correspond to EBLMMS built with 1024 (light green) and 16384 (dark green) nodes and GPR built using 1024 nodes (light blue lines). Axes indicating partial pressures associated to the adsorption rate constants (cf. eq (41)) and the activation barrier associated to the CO oxidation rate constant (cf. 42) are also included.

section II B) and GPR (cf. SM) methods for comparison. For EBMS, N_q values equal to the N_t values above were used, as well as $N_w = N_q/2$, $N_w = N_q$, $N_w = 2N_q$. As for the case of the analytic test functions, comparing EBLMMS and EBMS shows that incorporating the local metrics produces a noticeable improvement in the quality measure. Interestingly, the error values for GPR and EBLMMS are very similar, with EBLMMS's being slightly lower except for very low node counts. However, a careful investigation reveals that important qualitative differences are not sufficiently reflected by this error measure. In the next section, we demonstrate that GPR is not able to capture features with rapid function value and gradient changes as well as EBLMMS. Since such regions are localized in a small volume fraction of the domain, this difference is not properly captured by an integral error measure such as Φ. In section III B 3, we show that these difference can have large impacts in results of coupled 1p-kMC/CFD simulations.

2. Graphical Analysis

To provide a clearer understanding of the quality and scaling of the interpolant, we present 2D line plots of the CO oxidation TOF as a function of selected rate constants in Fig. 8. Both EBLMMS and GPR are compared to a set of additional 1p-kMC data points (not included in the interpolants' input database). The curves show the values the 7D interpolants take along 1D cuts of the domain in which all but one of the parameters are kept constant. We have decided to focus on the directions of the adsorption rate constants, which can be directly associated to changes in the partial pressures p_{CO} and p_{O_2}, cf. eq. (41), and of the CO oxidation rate constant k^{reac}, which can be associated to potential errors in the activation barrier for oxidation, cf. eq. (42). These associated dependencies have been indicated by extra axes in the plots. In all three directions, the TOF presents a rapid, step-like change in value and gradient, which presents a challenge for the interpolation methods.

From the plots it can already be seen that EBLMMS presents the correct qualitative behavior even at a very low node count of $N = 1024$. Although there are quantitative errors for high k^{reac} values, we see that EBLMMS is able to reproduce the step-like nature of the transition. For the k^{ads}_{CO} (p_{CO}) and $k^{ads}_{O_2}$ (p_{CO}) cases, there is even very good quantitative agreement. In contrast, GPR is qualitatively poorer in all cases at such (desirably) low node count. It is never able to reproduce the shape of the curves, and misses to match the high TOF peak in all cases. For the k^{reac} case, it does not even hint the step-like shape. In 1p-kMC/CFD such interpolant deficiencies are crucial: The highest TOF values at the ridge need to be reproduced quantitatively, as this corresponds precisely to the region of highest activity targeted in catalysis research. Steep TOF increases over small pressure regions are also critical topological features that govern potential reactor instabilities or gas-phase coupled activity oscillations. If such features are washed out as by the

GPR interpolant in Fig. 8, the very targets of coupled microkinetic - fluid dynamical multiscale simulations can not be met by construction.

Further increasing the number of nodes systematically improves the quality of the EBLMMS interpolant. In Fig. 8, this is illustrated for $N = 16384$ nodes, in which very good quantitative agreement is found for all the cases shown. In the SM we have included a plot similar to Fig. 8 presenting examples for other choices of number of nodes N. There it can be seen that the quality of GPR remains low even up to 4096 nodes (the highest value analyzed).

Another impression of the behavior of the interpolation method can be gained by looking at the contour plots presented in Fig. 9. The plots show TOF contour plots across cuts of the 7D domain in which all rate constants except for $k_{\mathrm{CO}}^{\mathrm{ads}}$ and k^{reac} are now kept fixed at their default values. The panels on the left (same data top and bottom) show 1p-kMC data explicitly calculated on a (100×100) grid. The central panels show the TOF values predicted by the 7D EBLMMS interpolant built using $N = 1024$ (top) and $N = 8192$ (bottom) nodes. The panels on the right show the corresponding absolute value of the error, calculated in the transformed (logarithmic) TOF scale. The plots demonstrate that even for $N = 1024$ the qualitative features of the target function are remarkably well reproduced. For $N = 8192$, the 1p-kMC and EBLMMS results are almost indistinguishable by eye. In addition, it can be observed that the errors are concentrated in the regions of rapid gradient change and very small in the rest of the domain. The conditions of Fig. 8c are marked in the contour plots by a dotted line. We can rationalize the difficulty of reproducing TOF values for high k^{reac} by noting that these conditions fall into the TOF peak observed in the contours (i.e. located in the top-center region). This peak is relatively localized and thus very difficult to predict using only a small number of nodes. In the SM, an analogous contour plot with GPR predictions using 1024 nodes is presented. It shows that the qualitative behavior is poorer than the corresponding EBLMMS interpolant.

3. A Stagnation Flow Example

To further underscore our general remarks on the required accuracy of TOF interpolants in coupled 1p-kMC/CFD simulations, we consider an isothermal and stationary stagnation flow[51], where a mixture of CO, O_2 and Argon streams from a sieve-like inlet against a disk-shaped catalyst. This is a suitable reactor model for flat-faced single-crystal model catalysts as in the reduced $RuO_2(110)$ 1p-kMC CO oxidation model, which we will continue to use for this demonstration. As illustrated in Fig. 10, the geometry of the axisymmetric reactor problem is fully determined by the vertical height L of the inlet. For the calculations we employ $L = 3\,\mathrm{cm}$ and an inlet velocity of $10\,\mathrm{cm/s}$. The oxygen partial pressures at the inlet is chosen as $p_{\mathrm{O_2}}^{\mathrm{inlet}} = 1\,\mathrm{bar}$, the CO partial pressure $p_{\mathrm{CO}}^{\mathrm{inlet}}$ varies between one and four bar, and 50% of the mixture is always Argon, i.e $p_{\mathrm{Ar}}^{\mathrm{inlet}} = p_{\mathrm{O_2}}^{\mathrm{inlet}} + p_{\mathrm{CO}}^{\mathrm{inlet}}$. We obtain numerical solutions to the resulting one-dimensional boundary value problem using our previously employed perturbative approach (see supporting information in Ref.[11]) and a stagnation flow solver[8,9].

The interpolated TOF enters the stagnation flow equations as a non-linear boundary condition. As a reference, we use a dense regular 2D grid of 100×100 1p-kMC data points in the pressure range $(p_{\mathrm{CO}}, p_{\mathrm{O_2}}) \in [10^{-2}, 10^{2}]^2$, which we interpolate piecewise linearly. Against this reference, we assess the performance of the high-dimensional GPR and EBLMMS surrogate models with a low number of interpolation nodes $N = 1024$ (cf. Fig. 8), i.e. we employ the full 7D interpolations and eq. (41) to obtain the partial pressures. This way, we can asses the impact of interpolation errors in multidimensional TOF maps onto CFD simulations results. Such multidimensional TOF maps naturally arise from 1p-kMC models with many reactive species, but also the here considered TOF map of the individual rates might be beneficial in practice, e.g. when fitting reaction parameters to experimental reactor data.

Figure 10 shows the CO_2 partial pressure directly above the catalyst $p_{\mathrm{CO_2}}^{\mathrm{catal}}$, which would be the central experimental observable, e.g. when employing Planar Laser Induced Fluorescence measurements[11,52], and which is related to the catalytic activity. For our reference calculations (black dots), we find a low, monotonically increasing activity ($p_{\mathrm{CO_2}}^{\mathrm{catal}}$) for $p_{\mathrm{CO}}^{\mathrm{inlet}}$ below the stoichiometric ratio. For high $p_{\mathrm{CO}}^{\mathrm{inlet}}$, the activity is higher and monotonically decreasing. These two regimes are connected by a relatively narrow regime for $p_{\mathrm{CO}}^{\mathrm{inlet}}$ slightly above the stoichiometric ratio, in which we find multiple stationary solutions that could give rise to gas-phase coupled oscillatory behavior of the catalytic activity. The EBLMMS-based model reproduces the behavior of the reference calculation with only minor quantitative differences. In contrast, the GPR-based model deviates largely from the reference calculation for most of the CO pressure range. Particularly at the phase transition it provides a qualitatively wrong picture. Multiple solutions appear where they should not be, while the true regime with multiple solutions is missed. This is a direct consequence of its inability to properly trace the steep TOF variations predicted by the 1p-kMC model.

IV. SUMMARY AND OUTLOOK

We have presented an interpolation technique able to faithfully approximate high-dimensional functions with locally rapid changes, such as those arising from first-principles kinetic Monte Carlo models for heterogeneous catalysis. Exploiting the fact that such functions often show locally low-dimensional behavior, small global er-

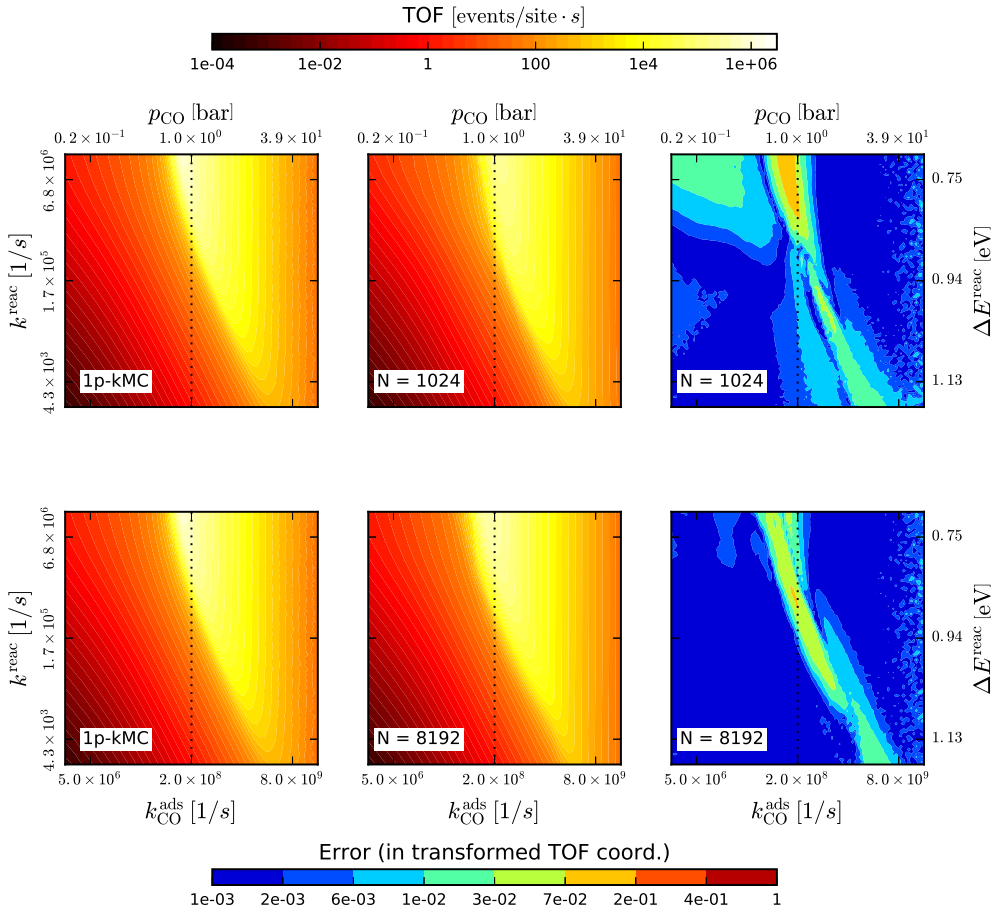

FIG. 9. Contours of CO oxidation TOF explicitly calculated with the 1p-kMC model (left, plot repeats top and bottom), compared with interpolations generated by EBLMMS using 1024 nodes (center, top) and 8192 nodes (center, bottom). The panels on the right present the error, measured in the transformed TOF coordinates. The domain is cut through its center (where all rate constants have their default value) and parallel to the axes corresponding to the CO adsorption and CO oxidation rate constants. The dotted lines mark the conditions plotted in Fig. 8.c. Additional axes have been added to show the correspondence between changes in k^{ads}_{CO} and p_{CO} (k^{reac} and ΔE^{reac}).

rors can be achieved with this error-based local metric modified Shepard (EBLMMS) method even with modest numbers of function evaluations. Furthermore, the method successfully suppresses undesired behavior, such as oversmoothing and artificial wiggles.

Compared with existing methods from the Shepard family as well as with state-of-the-art Gaussian process regression, our approach proved to be superior for tested target functions ranging from analytic test cases up to numerical 1p-kMC data. In higher dimensions in particular, our combination of a locally changing metric and error estimate based blending proved to be advantageous. The superior accuracy was also shown to be very important when building surrogates for use in 1p-kMC/CFD coupling.

Another strength of the approach is its basis in geometrical considerations and a conceptually simple mathematical description. Most input parameters either have an intuitive geometrical meaning or can be interpreted as an error, either in the error function or in the coefficients of the local metric. Nevertheless, methodologically there is still room for improvement. Most importantly, this concerns the determination of the ellipsoids which define the clouds. A better initial guess of the local metric as well as the exploitation of more efficient and robust optimization algorithms are desirable. Furthermore, data structures can be developed which exploit the finite support of the interpolation weights and make evaluation times scale sub-linearly with the number of nodes. Finally, the cheaply available error estimates could be used for parameter set optimization. Instead of having to split the calculated data into construction and tests sets, the parameters could be obtained by minimizing the error estimates at points in which the true function value is unknown.

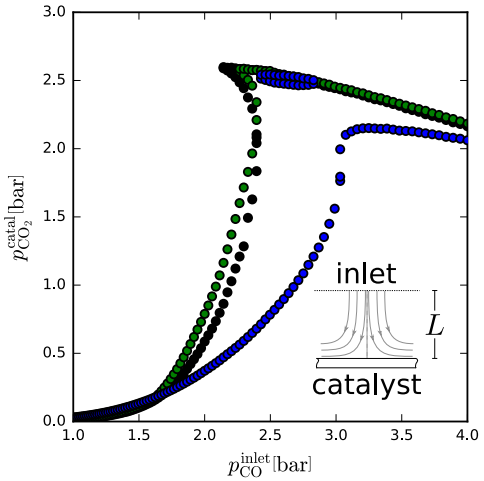

FIG. 10. Steady-state CO_2 partial pressure immediately over the catalyst as a function the CO partial pressure of the inlet of the stagnation flow reactor schematically depicted in the inset. Detailed conditions of the simulation are summarized in the text. We compare the results obtained using as catalyst boundary condition a reference solution (black) with those using the EBLMMS- (green) and GPR- (blue) based interpolants discussed in Fig. 8. Both surrogates are built using a total of 1024 nodes.

SUPPLEMENTARY MATERIAL

See supplementary material for: (a) the justification of eqs. (26), (30) and (31), (b) the exact definition of the analytic test functions, (c) a description of the GPR method used, (d) error scaling plots for two additional test function classes, (e) a graphical comparison of EBLMMS interpolants with different N_t values, (f) a plot similar to Fig. 8 for interpolants built with different numbers nodes and (g) a graphical comparison between EBLMMS and GPR for the 1p-kMC model.

ACKNOWLEDGMENTS

We gratefully acknowledge support from the German Research Council (DFG) and the TUM Faculty Graduate Center Chemistry, as well as generous computing time at the Leibniz Rechenzentrum (LRZ) of the Bavarian Academy of Sciences. S.M.'s research is carried out in the framework of MATHEON supported by the Einstein Foundation Berlin. J.M.L. warmly thanks A. Martinez and F. Busnengo for their hospitality during his stay at Instituto de Física Rosario, Argentina, where parts of this work were carried out.

[1] J. Behler, J. Phys.: Condens. Matter **26**, 183001 (2014).
[2] A. P. Bartók, M. C. Payne, R. Kondor, and G. Csányi, Phys. Rev. Lett. **104**, 136403 (2010).
[3] T. Stecher, N. Bernstein, and G. Csányi, J. Chem. Theory. Comput. **10**, 4079 (2014).
[4] L. Mones, N. Bernstein, and G. Csányi, J. Chem. Theory Comput. **12**, 5100 (2016).
[5] H. F. Busnengo, A. Salin, and W. Dong, J. Chem. Phys. **112**, 7641 (2000).
[6] D. Strobusch and C. Scheurer, J. Chem. Phys. **140**, 074111 (2014).
[7] M. A. Collins, Theor. Chem. Acc. **108**, 313 (2002).
[8] S. Matera and K. Reuter, Catal. Lett. **133**, 156 (2009).
[9] S. Matera and K. Reuter, Phys. Rev. B **82**, 085446 (2010).
[10] S. Matera, M. Maestri, A. Cuoci, and K. Reuter, ACS Catal. **4**, 4081 (2014).
[11] S. Matera, S. Blomberg, M. J. Hoffmann, J. Zetterberg, J. Gustafson, E. Lundgren, and K. Reuter, ACS Catal. **5**, 4514 (2015).
[12] M. Votsmeier, Chem. Eng. Sci. **64**, 1384 (2009).
[13] M. Votsmeier, A. Scheuer, A. Drochner, H. Vogel, and J. Gieshoff, Catal. Today **151**, 271 (2010).
[14] S. Pope, Combust. Theory Modell. **1**, 41 (1997).
[15] A. Varshney and A. Armaou, Chem. Eng. Sci. **60**, 6780 (2005).
[16] A. Varshney and A. Armaou, Comput. Chem. Eng. **32**, 2136 (2008).
[17] K. Reuter, D. Frenkel, and M. Scheffler, Phys. Rev. Lett. **93**, 116105 (2004).
[18] K. Reuter, Catal. Lett. **146**, 541 (2016).
[19] J. M. Lorenzi, S. Matera, and K. Reuter, ACS Catal. **6**, 5191 (2016).
[20] R. J. Renka, ACM Trans. Math. Softw. **14**, 139 (1988).
[21] S. Vijayakumar, A. D'souza, and S. Schaal, Neural Comput. **17**, 2602 (2005).
[22] C. Zuppa, Appl. Numer. Math. **49**, 245 (2004).
[23] M. Maestri and A. Cuoci, Chem. Eng. Sci. **96**, 106 (2013).
[24] D. Shepard, in *Proceedings of the 1968 23rd ACM National Conference*, ACM '68 (ACM, New York, NY, USA, 1968) pp. 517–524.
[25] R. Franke and G. Nielson, Int. J. Numer. Meth. Eng. **15**, 1691 (1980).
[26] S. Bochkanov, "ALGLIB," www.alglib.net.
[27] James W. Demmel, *Applied Numerical Linear Algebra* (SIAM, Philadelphia, PA, USA, 1997).
[28] Python Software Foundation, "Python 2.7," http://www.python.org/.
[29] "SWIG: Simplified wrapper and interface generator," http://www.swig.org.
[30] L. S. Blackford, J. Demmel, J. Dongarra, I. Duff, S. Hammarling, G. Henry, M. Heroux, L. Kaufman, A. Lumsdaine, A. Petitet, R. Pozo, K. Remington, and R. C. Whaley, ACM Trans. Math. Softw. **28**, 135 (2002).
[31] E. Anderson, Z. Bai, C. Bischof, S. Blackford, J. Demmel, J. Dongarra, J. Du Croz, A. Greenbaum, S. Hammarling, A. McKenney, and D. Sorensen, *LAPACK Users' Guide*, 3rd ed. (SIAM, Philadelphia, PA, 1999).
[32] S. G. Johnson, "The NLopt nonlinear-optimization package," http://ab-initio.mit.edu/nlopt.
[33] M. J. D. Powell, in *Advances in Optimization and Numerical Analysis*, edited by S. Gomez and J.-P. Hennart (Kluwer Academic, Dordrecht, 1994) pp. 51–67; M. Powell, Acta Numer. , 287 (1998).
[34] K. Svanberg, SIAM J. Optimiz. **12**, 555 (2002).
[35] I. Sobol, USSR Comput. Math. Math. Phys. **7**, 86 (1967).
[36] P. L'Ecuyer and C. Lemieux, in *Modeling Uncertainty: An Examination of Stochastic Theory, Methods, and Applications*, edited by M. Dror, P. L'Ecuyer, and F. Szidarovszky (Springer, Boston, MA, 2005) pp. 419–474.
[37] C. E. Rasmussen and C. K. I. Williams, *Gaussian Processes for Machine Learning (Adaptive Computation and Machine Learning series)* (MIT Press, 2005).
[38] D. J. C. Mackay, *Information Theory, Inference and Learning Algorithms*, 1st ed. (Cambridge University Press, 2003).

[39]GPy, "GPy: A gaussian process framework in python," `http://github.com/SheffieldML/GPy` (since 2012).
[40]K. Reuter and M. Scheffler, Phys. Rev. B **73**, 045433 (2006).
[41]P. Gelß, S. Matera, and C. Schütte, J. Comput. Phys. **314**, 489 (2016).
[42]H. Meskine, S. Matera, M. Scheffler, K. Reuter, and H. Metiu, Surf. Sci. **603**, 1724 (2009).
[43]S. Döpking and S. Matera, Chem. Phys. Lett. **674**, 28 (2017).
[44]M. J. Hoffmann, F. Engelmann, and S. Matera, J. Chem. Phys. **146**, 044118 (2017).
[45]J. E. Sutton, W. Guo, M. A. Katsoulakis, and D. G. Vlachos, Nat. Chem. **8**, 331 (2016).
[46]B. Temel, H. Meskine, K. Reuter, M. Scheffler, and H. Metiu, J. Chem. Phys. **126**, 204711 (2007).
[47]S. Matera, H. Meskine, and K. Reuter, J. Chem. Phys. **134**, 064713 (2011).
[48]D.-J. Liu and J. W. Evans, J. Chem. Phys. **142**, 134703 (2015).
[49]G. J. Herschlag, S. Mitran, and G. Lin, J. Chem. Phys. **142**, 234703 (2015).
[50]M. J. Hoffmann, S. Matera, and K. Reuter, Comput. Phys. Commun. **185**, 2138 (2014).
[51]R. Kee, M. Coltrin, and P. Glarborg, *Chemically Reacting Flow, Theory and Practice* (Wiley, Hoboken, NJ, 2003).
[52]J. Zetterberg, S. Blomberg, J. Gustafson, Z. W. Sun, Z. S. Li, E. Lundgren, and M. Aldén, Rev. Sci. Instrum. **83**, 053104 (2012).

Supplementary Material for: Local-metrics error-based Shepard interpolation as surrogate for highly non-linear materials models in high dimensions

Juan M. Lorenzi,[1, a)] Thomas Stecher,[1] Karsten Reuter,[1] and Sebastian Matera[2]
[1)] *Chair for Theoretical Chemistry and Catalysis Research Center, Technische Universität München, Lichtenbergstr. 4, 85747 Garching (Germany)*
[2)] *Fachbereich f. Mathematik u. Informatik, Freie Universität Berlin, Otto-von-Simson-Str. 19, D-14195 Berlin (Germany)*

(Dated: 27 September 2017)

I. LOCALIZATION FUNCTION AND CLOUD NODE COUNT ESTIMATES

Here we demonstrate the properties

$$\eta_-(M_k) \leq \eta_0(M_k) \tag{S-1a}$$
$$\eta_+(M_k) \geq \eta_0(M_k) \tag{S-1b}$$

of the soft constraint functions defined in eqs. (30) and (31) in the main text. Given a symmetric, positive definite matrix M_k, a vector $\mathbf{x}_k \in \mathbb{R}^D$ and a real number $R > 0$, we define the associated ellipsoid according to

$$E(M_k, \mathbf{x}_k, R) = \{\mathbf{x} \in \mathbb{R}^D \mid ||M(\mathbf{x} - \mathbf{x}_0)||_2 < R\} \quad . \tag{S-2}$$

Such ellipsoids define the support of localization function $\lambda(R, r, d_k(\mathbf{x}))$ (cf. eq. (23)), when the distance $d_k(\mathbf{x})$ is given by eq. (24). In addition, $\lambda(R, r, d_k(\mathbf{x}))$ is strictly equal to 1 when $\mathbf{x}$ belongs to the smaller ellipsoid $E(M_k, \mathbf{x}_k, R - r)$, and $0 \leq \lambda(R, r, d_k(\mathbf{x})) < 1$ when $\mathbf{x}$ is within the ellipsoidal shell between $E(M_k, \mathbf{x}_k, R-r)$ and $E(M_k, \mathbf{x}_k, R)$. In the limit $r = 0$, $\lambda(R, 0; d_k(\mathbf{x}))$ is the indicator function for $E(M_k, \mathbf{x}_k, R)$, i.e.

$$\lambda(R, 0; d_k(\mathbf{x})) = \begin{cases} 1, \text{if } \mathbf{x} \in E(M_k, \mathbf{x}_k, R) \\ 0, \text{if } \mathbf{x} \notin E(M_k, \mathbf{x}_k, R) \end{cases} \quad .$$

As this function is strictly equal to 1 in the whole $E(M_k, \mathbf{x}_k, R)$, we can see that

$$\lambda(R, 0; d_k(\mathbf{x})) \geq \lambda(R, r; d_k(\mathbf{x})) \quad \forall 0 \leq r < R \quad . \tag{S-3}$$

Similarly, localization function $\lambda(R+r, r, d_k(\mathbf{x}))$ has finite support in ellipsoid $E(M_k, \mathbf{x}_k, R+r)$, and is strictly equal to 1 on $E(M_k, \mathbf{x}_k, R)$. This results in

$$\lambda(R, 0; d_k(\mathbf{x})) \leq \lambda(R + r, r; d_k(\mathbf{x})) \quad \forall 0 \leq r \quad . \tag{S-4}$$

From eq. (25) in the main text, we can see that the clouds for the EBLMMS interpolant are given by $\omega_k = E(M_k, \mathbf{x}_k, 1)$. Correspondingly, the functions $\lambda(1, 0; d_k(\mathbf{x}))$ are indicator functions for clouds ω_k. With this in mind, the total number of nodes in the cloud can be calculated as the summation

$$\eta_0(M_k) = \sum_{i=1}^{N} \lambda(1, 0; d_k(\mathbf{x}_i)) \quad . \tag{S-5}$$

Using this and relation (S-3) we can see that

$$\begin{aligned} \eta_0(M_k) &= \sum_{i=1}^{N} \lambda(1, 0, d_k(\mathbf{x}_i)) \\ &\geq \sum_{i=1}^{N} \lambda(1, r_-, d_k(\mathbf{x}_i)) = \eta_-(M_k) \end{aligned} \tag{S-6}$$

and similarly, using relation (S-4),

$$\begin{aligned} \eta_0(M_k) &= \sum_{i=1}^{N} \lambda(1, 0, d_k(\mathbf{x}_i)) \\ &\leq \sum_{i=1}^{N} \lambda(1 + r_+, r_+, d_k(\mathbf{x}_i)) = \eta_+(M_k). \end{aligned} \tag{S-7}$$

This demonstrates relations (S-1).

Next, we justify eqs. (26) and (32) (main text) for the scaling of the r_0, r_- and r_- parameters with dimension D (cf. section II C from the main text). Using basic concepts of multidimensional calculus, it is easy to prove that the volume of the ellipsoids is given by

$$V\left(E(M, \mathbf{x}_0, R)\right) = \frac{V\left(B_D(R)\right)}{\det M} \quad , \tag{S-8}$$

where $\det M$ is the determinant of M and $V\left(B_D(R)\right)$ is the volume of a D-ball of radius R defined as

$$B_D(R) = \{\mathbf{x} \in \mathbb{R}^D \mid ||\mathbf{x}||_2 < R\} \quad . \tag{S-9}$$

Using this, we see that the ratio between the volume of an ellipsoidal shell between $E(M_k, \mathbf{x}_k, 1)$ (i.e. the cloud ω_k) and $E(M_k, \mathbf{x}_k, 1 - r)$ (i.e. the region in which $\lambda(1, r; d_k(\mathbf{x})) = 1$ strictly) and the volume of $E(M_k, \mathbf{x}_k, 1)$ itself is

$$\begin{aligned} \frac{V\left(E(M, \mathbf{x}_0, 1)\right) - V\left(E(M, \mathbf{x}_0, 1-r)\right)}{V\left(E(M, \mathbf{x}_0, 1)\right)} = \\ \frac{V\left(B_D(1)\right) - V\left(B_D(1-r)\right)}{V\left(B_D(1)\right)} = \\ 1 - (1-r)^D \quad , \end{aligned} \tag{S-10}$$

[a)] juan.lorenzi@tum.de

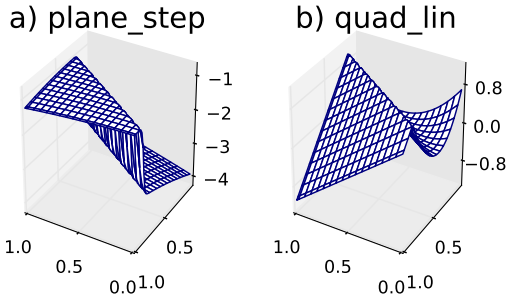

FIG. S-1: Representation of the 2D version of the two additional analytic function classes.

where we have used the fact that $B_D(R) = B_D(1)R^D$. Replacing the expression for r_0 (r_-) from eq. (26) (eq. (32a)), it is easy to see that the resulting volume ratio is equal to ρ_0 (ρ_{soft}) (i.e. independent of D).

Similarly, if we consider an ellipsoidal shell immediately outside (surrounding) the cloud $E(M_k, \mathbf{x}_k, 1)$, we get

$$\begin{aligned}\frac{V\left(E(M,\mathbf{x}_0,1+r_+)\right) - V\left(E(M,\mathbf{x}_0,1)\right)}{V\left(E(M,\mathbf{x}_0,1)\right)} = \\ \frac{V\left(B_D(1+r_+)\right) - V\left(B_D(1)\right)}{V\left(B_D(1)\right)} = \\ (1+r_+)^D - 1 \quad .\end{aligned} \tag{S-11}$$

Replacing r_+ from eq. (32b) in the main text, the volume ratio equals ρ_{soft}.

II. EXACT DEFINITION OF TEST FUNCTIONS

Here we present the formulae for the test functions used in section III A of the main text as well as for two additional test function classes only discussed in this SI. Wireframe plots of the 2D versions of the extra functions classes are presented in Fig. S-1. Functions of the `plane_step` family present small gradients in most of the domain, except for a sharp (but differentiable) step-like transition located around a $(D-1)$-hyperplane. Therefore, these functions are intrinsically one-dimensional. Functions of the `quad_lin` class are also intrinsically one-dimensional. They are quadratic on one side of an hyperplane, and linear in the other. Contrary to the other function classes used in this work, `quad_lin` functions present rapid changes in the gradient, but not on the function value.

All the parameters that enter the definition of the test functions are summarized in Table S-I. For functions with $D < 7$, the coefficients of vector parameters $\mathbf{x}_0$, $\mathbf{n}_0$ and $\mathbf{n}_1$ were just taken as the first D coefficients of the vectors in the table.

All step-like functions are defined based on the 1D step function

$$\begin{aligned}\mathrm{s}(x,t) = \\ -2\mathrm{sig}(x,t) + (1-\mathrm{sig}(x,t))\,(x-4) \\ +\cos(x)\end{aligned} \tag{S-12}$$

where

$$\mathrm{sig}(x,t) = \frac{1}{1+e^{-x/t}} \tag{S-13}$$

is the sigmoid function, and t defines the width of the transition.

Using this we define the `plane_step` functions as

$$f_{\texttt{plane\_step}}(\mathbf{x}) = \mathrm{s}\left(\frac{\mathbf{n}_0\cdot(\mathbf{x}-\mathbf{x}_0)}{|\mathbf{n}_0|}, t\right) \quad , \tag{S-14}$$

where $\mathbf{n}_0$ is the direction normal to hyperplane where the step-like transition occurs and $\mathbf{x}_0$ is a point of such hyperplane.

Functions of the `kink_step` family are given by

$$f_{\texttt{kink\_step}}(\mathbf{x}) = \begin{cases} \mathrm{s}\left(\max(p_0,p_1),t\right) & \text{if } p_0,p_1<0 \\ & \text{or } p_0,p_1\geq 1 \\ \mathrm{s}(p_0,t) & \text{if } p_1<0, p_0\geq 1 \\ \mathrm{s}(p_1,t) & \text{if } p_0<0, p_1\geq 1 \end{cases} \tag{S-15}$$

with $p_0 = \mathbf{n}_0\cdot(\mathbf{x}-\mathbf{x}_0)/|\mathbf{n}_0|$ and $p_1 = \mathbf{n}_1\cdot(\mathbf{x}-\mathbf{x}_0)/|\mathbf{n}_1|$. Here $\mathbf{n}_0$ and $\mathbf{n}_1$ are the directions normal to the half-hyperplanes defining the kink; and $\mathbf{x}_0$ is a point on the hypersurface where they meet.

Functions of the `ball_step` family are given by

$$f_{\texttt{ball\_step}}(\mathbf{x}) = \mathrm{s}\left(\left|\mathbf{x}-\mathbf{x}_0+R\frac{\mathbf{n}_0}{|\mathbf{n}_0|}\right| - R, t\right) \quad , \tag{S-16}$$

where R is the ball's radius, $\mathbf{x}_0$ is a point on the edge of the ball and, $\mathbf{n}_0$ defines the direction normal to a hyperplane tangent to the ball that passes through $\mathbf{x}_0$.

Finally, functions of the `quad_lin` family are defined with the help of the 1D function

$$\mathrm{u}(x,t) = \begin{cases} y_0+\alpha x+\beta x^2 \text{ if } x\leq -t \\ a_0+a_1x+a_2x^2+a_3x^3 \text{ if } -t\leq x<t \\ y_0+\gamma x \text{ if } t<x \end{cases} \tag{S-17}$$

where

$$\begin{aligned} a_0 &= y_0 + \frac{(\gamma-\alpha)t}{4} \\ a_1 &= \frac{\alpha+\gamma}{2} - \frac{\beta t}{4} \\ a_2 &= \frac{\gamma-\alpha}{4t} + \frac{\beta}{2} \\ a_3 &= -\frac{\beta}{4t} \end{aligned}$$

to make the transition smooth within a distance t. With this, we define

$$f_{\texttt{quad\_lin}}(\mathbf{x}) = \mathrm{u}\left(\frac{\mathbf{n}_0 \cdot (\mathbf{x}-\mathbf{x}_0)}{|\mathbf{n}_0|}, t\right) \quad , \tag{S-18}$$

where $\mathbf{n}_0$ and $\mathbf{x}_0$ define normal direction to and a point belonging to the plane in which the rapid gradient change takes place.

TABLE S-I: Values of the parameters defining the analytic test functions.

Scalar parameters							
$t = 0.01$				$R = 1.00$			
$y_0 = 1.00$		$\alpha = 6.00$		$\beta = 8.00$		$\gamma =$ -3.00	
Vector parameters							
$\mathbf{x}_0$	0.5	0.5	0.5	0.5	0.5	0.5	0.5
$\mathbf{n}_0$	0.551	0.795	0.219	0.714	0.683	0.516	0.556
$\mathbf{n}_1$	0.609	0.276	0.297	0.305	0.322	0.211	0.635

III. GAUSSIAN PROCESS REGRESSION

While we refer to textbooks[1,2] for an in-depth introduction of Gaussian Process Regression (GPR), we would like to give a brief outline in order to clarify this point of reference. GPR is a Bayesian method: it assumes a prior probability distribution on the function values we wish to predict and combines this with the observed, possibly noisy data. The prior distribution of function values is assumed to be a Gaussian process, which describes a distribution over functions and can loosely be thought of as an infinite-dimensional multivariate Gaussian distribution. Just as a multivariate Gaussian distribution is defined by a mean vector and covariance matrix, a Gaussian process is defined by a mean function $m(\mathbf{x})$ (often taken to be 0) and a covariance function (or kernel) $k(\mathbf{x}_i, \mathbf{x}_j)$. Conditioning this prior on the observations yields another (posterior) Gaussian process with the following predictive mean and covariance functions:[1]

$$g(\mathbf{x}) = \bar{f}(\mathbf{x}) = \mathbf{k}^T(\mathbf{x}, X)(K(X) + \sigma_y \mathbf{I})^{-1}\mathbf{F} \tag{S-19}$$

$$\mathrm{cov}(f(\mathbf{x}_1), f(\mathbf{x}_2)) = k(\mathbf{x}_1, \mathbf{x}_2) - \mathbf{k}^T(\mathbf{x}_1, X)\cdot \cdot (K(X) + \sigma_y \mathbf{I})^{-1}\mathbf{k}(\mathbf{x}_2, X), \tag{S-20}$$

where $\mathbf{F}$ are the observed function values at the nodes X. $\mathbf{k}(\mathbf{x}, X)$ is the vector composed of covariance function values $k(\mathbf{x}, \mathbf{x}_i)$, the matrix $K(X)$ collects the values of the covariance function between nodes, σ_y represents the noise associated with the input data and $\mathbf{I}$ is the identity matrix. Equations S-19 and S-20 are the key working equations of GPR, with the former interpreted as the central prediction and the latter indicating its uncertainty. Note, in particular, that in general GPR assumes the input data to be noisy, with the level of noise not only affecting the posterior covariance, but also the prediction (mean function). In essence, this allows GPR to interpolate between noisy data points, thus avoiding overfitting.

A. Covariance Functions and Hyperparameters

The choice of covariance function is key to a meaningful application of GPR. It determines, for example, how smooth the Gaussian process reconstruction will be. Many commonly used covariance functions, including the popular squared exponential covariance function,

$$k(\mathbf{x}_1, \mathbf{x}_2) = \sigma_f^2 \exp\left(-\frac{|\mathbf{x}_1 - \mathbf{x}_2|^2}{2l^2}\right), \tag{S-21}$$

are so-called stationary functions, meaning they only depend on the difference $\mathbf{x}_1 - \mathbf{x}_2$. Clearly, for the target applications of this paper, such a choice would be inappropriate and we have indeed verified that it leads to poor results. Instead we used the so-called 'neural network' kernel (sometimes also referred to as 'arc sine' or 'multilayer perceptron' (MLP) kernel). It can be constructed as the limit of a neural network with one hidden layer and an infinite number of hidden units,[1] thus representing a particularly general model. In its most general form this kernel is given by[1]

$$k_{NN}(\mathbf{x}_1, \mathbf{x}_2) = \sigma_f^2 \frac{2}{\pi} \sin^{-1}\left(\frac{2\tilde{\mathbf{x}}_1^\top \Sigma \tilde{\mathbf{x}}_2}{\sqrt{((1 + 2\tilde{\mathbf{x}}_1^\top \Sigma \tilde{\mathbf{x}}_1)(1 + 2\tilde{\mathbf{x}}_2^\top \Sigma \tilde{\mathbf{x}}_2))}}\right), \tag{S-22}$$

where $\tilde{\mathbf{x}}$ is obtained by augmenting the input vector $\mathbf{x}$ by a leading entry of 1. Since we wanted to compare our method to a readily available, off-the-shelf method, we used the kernel in the slightly less general form implemented in the freely-available GPy-package[3], which constrains Σ to be diagonal. Its entries, together with σ_f and the level of noise are referred to as "hyper-parameters" in the machine learning literature. They can be learned from the data by optimizing the so-called marginal likelihood or evidence of the model (the normalization factor of Bayes' theorem), which provides a way to quantify how well a model fits the data. It can also be used to compare altogether different covariance functions, and, again, we observe that the neural network kernel is much better suited to our class of problems than a simple stationary covariance function.

IV. ADDITIONAL ERROR SCALING PLOTS

In Fig. S-2 we present plots of how the Φ error from eq. 38 scales with the number of nodes for the `plane_step` and `quad_lin` function classes. The procedure to calculate these results is exactly the same as the one described in section III A 2 of the main text. The different methods

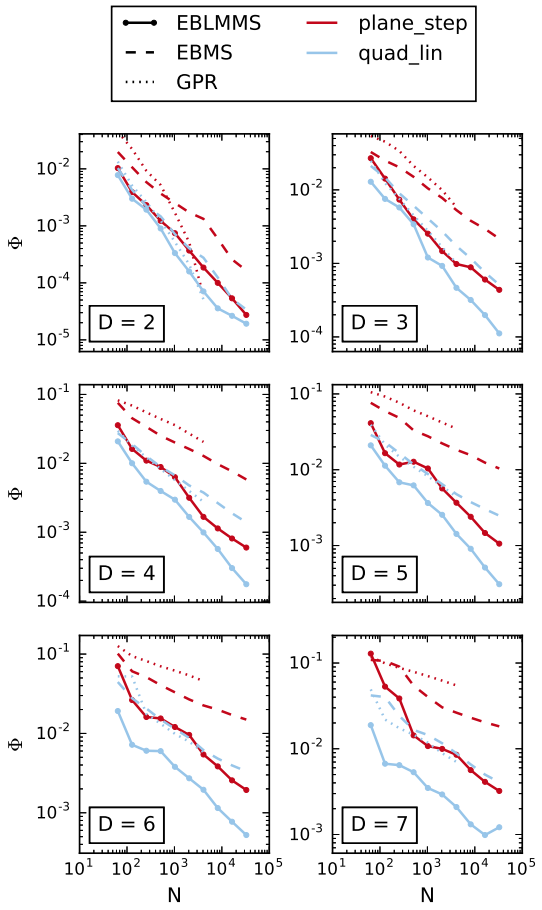

FIG. S-2: Scaling of the Φ error with increasing number of nodes for the `plane_step` (dark, red lines) and the `quad_lin` (light, blue lines) functions in different dimensions. The EBLMMS method (solid lines) is compared to EBMS (dashed lines) and GPR (dotted lines) methods.

compare to each other similarly with these functions as with the functions discussed in the main text. While this is to be expected for `plan_step` function, results for `quad_lin` demonstrate the benefits of employing the EBLMMS approach are not limited to step-like functions.

V. WIREFRAMES PLOTS FOR `ball_step` FOR DIFFERENT N_t VALUES

Here we present a qualitative comparison of the EBLMMS interpolation for different values of N_t. This is presented in Fig. S-3, where different interpolants of the 5D `ball_step` are presented. The cut of the domain used is the same as in Fig. 6 in the main text. While for very large N_t values the interpolant becomes smoothed out, for $N_t \leq 100$ it is able to very reasonably trace the

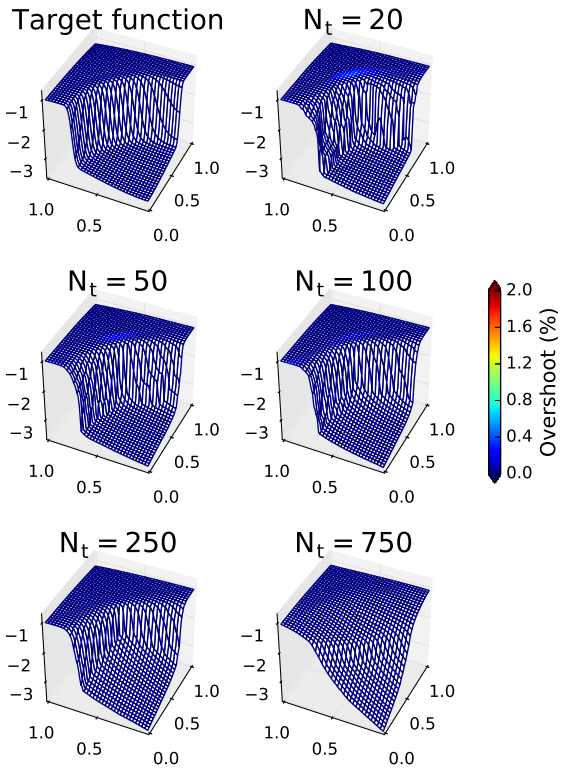

FIG. S-3: Wireframe plots for the 5D version of the `ball_step` test function, for different values of N_t. The number of nodes is $N = 1024$.

shape of the transition region step. Only for the smallest N_t value shown, some spurious features (similar to those observed for EBMS) appear. This shows that there is a wide range of values of N_t that result in an interpolant of reasonable quality.

VI. ADDITIONAL PLOTS FOR THE 1P-KMC EXAMPLE

In figure S-4 we present additional line plots of cuts of the 7D EBLMMS and GPR interpolants. There, we see that, even for 4096 nodes, GPR still presents poor qualitative behavior, even showing artificial oscillations in the $k^{\text{ads}}_{\text{O}_2}$ case. In contrast, EBLMMS already reaches good quantitative behavior, with small errors even in the challenging k^{reac} case. An EBLMMS interpolant built with 32768 nodes (the largest node count used in this work) is presented for reference, showing excellent quantitative agreement.

In Fig. S-5, we present contours comparing cuts of a 7D EBLMMS interpolants (center panel) with a 7D GPR

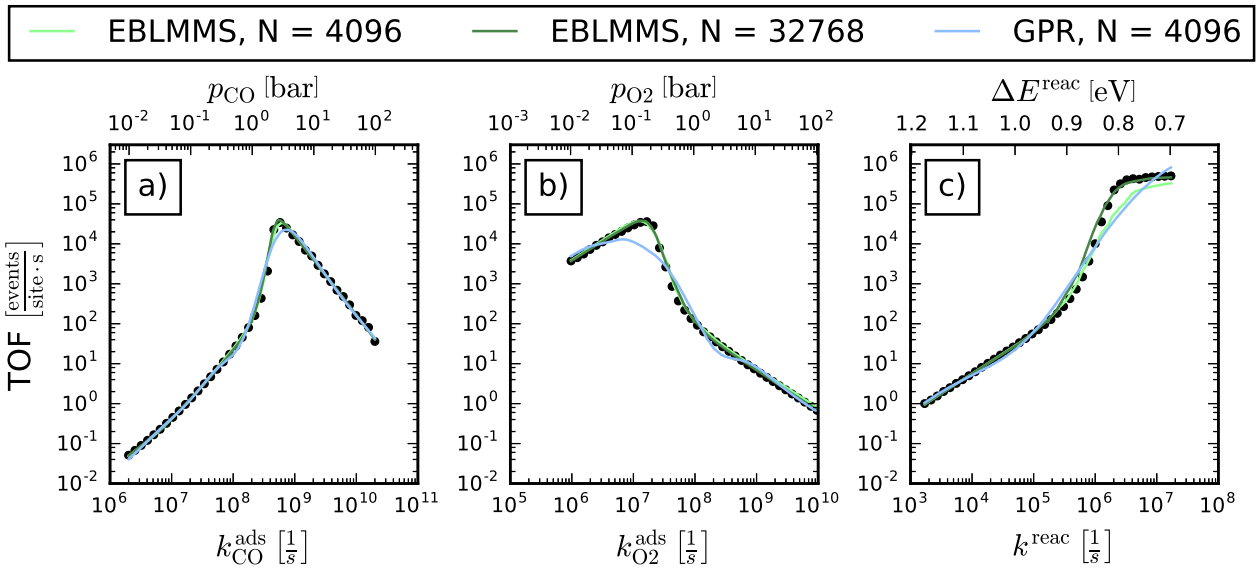

FIG. S-4: 1D cuts of different 7D interpolants compared to explicit 1p-kMC data not included in their input (dots). For each case, all but one of the rate constants where fixed at their default values (cf. tab. I). Lines correspond to EBLMMS built with 4096 (light green) and 32768 (dark green) nodes and GPR built using 1024 nodes (light blue lines). Axes indicating partial pressures associated to the adsorption rate constants (cf. eq (41)) and the activation barrier associated to the CO oxidation rate constant (cf. 42) are also included.

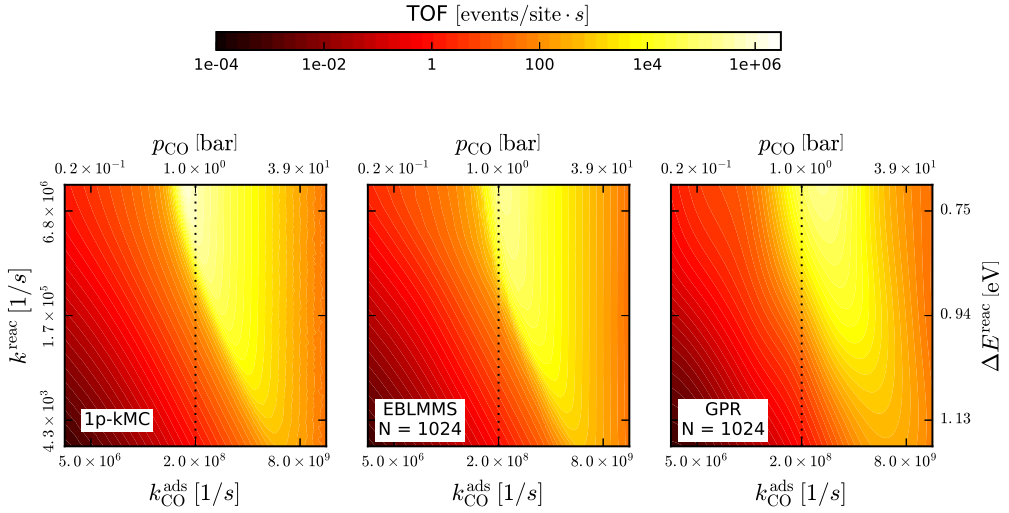

FIG. S-5: Contours of CO oxidation explicitly calculated with the 1p-kMC model (left), compared to the the interpolation generated by the EBLMMS (center) and to GPR results (right). For both approximation methods the number of nodes is $N = 1024$. The cut of the domain is done across the center of the domain (where all rate constants have their default value) and is parallel to the axes corresponding to the CO adsorption and CO oxidation rate constants. The dotted lines marks the conditions plotted in Fig. 8c in the main text.

model (right panel), both built using 1024 nodes. We also include explicitly calculated 1p-kMC data (left panel) for reference. As discussed in the main text, EBLMMS reproduces the function except for the height of the very localized maximum activity peak. In contrast, GPR produces a too smooth approximation, missing important features of the underlying function such as the sharp increase in reactivity when increasing CO adsorption. Nevertheless, this qualitative failure is rather localized. In seven dimensions, the subdomain where this happens

is therefore rather small and this qualitative failure has therefore only a minor impact on the integral L1 error norm.

[1]C. E. Rasmussen and C. K. I. Williams, *Gaussian Processes for Machine Learning (Adaptive Computation and Machine Learning series)* (MIT Press, 2005).

[2]D. J. C. Mackay, *Information Theory, Inference and Learning Algorithms*, 1st ed. (Cambridge University Press, 2003).

[3]GPy, "GPy: A gaussian process framework in python," `http://github.com/SheffieldML/GPy` (since 2012).